THE STRUCTURE OF EXOTIC NUCLEI ^{10}N AND ^{9}C USING THE ACTIVE TARGET APPROACH

A Dissertation

by

JOSHUA LEE HOOKER

Submitted to the Office of Graduate and Professional Studies of
Texas A&M University
in partial fulfillment of the requirements for the degree of

DOCTOR OF PHILOSOPHY

Chair of Committee,	Grigory V. Rogachev
Committee Members,	Charles M. Folden III
	Jeremy W. Holt
	Dan G. Melconian
Head of Department,	Grigory V. Rogachev

May 2019

Major Subject: Physics

ABSTRACT

The large imbalance between protons and neutrons and negative binding energy make these nuclei very challenging for experimental studies. Modern theoretical tools have been developed, such as *ab initio* Greens Function Monte Carlo or the large basis no-core shell model that start from bare nucleon-nucleon interactions or interactions based on the Effective Field Theory and provide exact or truncated solutions to the quantum many body problem. These theoretical approaches can handle up to A=12 nuclei and the study of ^{9}C and ^{10}N would provide stringent tests of the theoretical predictions.

^{10}Li plays an important role in the Borromean system ^{11}Li which is a two neutron halo system with two valence neutrons extending far beyond the ^{9}Li core. To model ^{11}Li, we most know about the ^{9}Li+n interaction that can be established from the known states in ^{10}Li. There are uncertainties in the spin-parity assignments and excitation energies of low-lying states in ^{10}Li and even less is known about its mirror nucleus, ^{10}N. We report on the first observation of the ground and first excited states in ^{10}N via ^{9}C+p resonance scattering. Both states were determined to be $\ell = 0$. We can now reliably place the location of the $2s_{1/2}$ shell in ^{10}N at 2.3 ± 0.2 MeV above the proton decay threshold. Using mirror symmetry and correcting for Thomas-Ehrman shift we argue that the ground state of ^{10}Li is an $\ell = 0$ state that should be very close to the neutron threshold.

The structure of ^{9}C was studied using ^{8}B+p resonance scattering with the newly commissioned Texas Active Target (TexAT) detector system. Recent theoretical developments allow for robust predictions of level structure of light nuclei, including continuum effects, starting from nucleon-nucleon and three-nucleon interactions [1, 2, 3]. High-quality experimental data are necessary to benchmark these predictions. Experimental data on ^{9}C is limited - only two excited states in ^{9}C have been observed. The goal of this work was two-fold. First, the ^{8}B+p resonance scattering was used as the first commissioning experiment for the active target detector system TexAT. This reaction was chosen because the experimental data on

^{8}B+p elastic scattering excitation function at low energy are available. The second goal was to search for positive parity states in ^{9}C (none are known). For that, we extended the ^{8}B+p elastic scattering excitation function to higher excitation energy, improved statistics and quality of the existing low energy data, measured angular distributions, and also searched for the ^{8}B(p,2p) reaction channel.

DEDICATION

To my mother and the memory of my father.

ACKNOWLEDGMENTS

I would first like to thank my adviser, Dr. Grigory Rogachev, who has always been available for any questions I have had and guidance over the last five years. It has been a privilege to work with such a remarkable scientist and I could not have imagined having a better mentor. I am indebted to Dr. Yevgen Koshchiy for without his tireless work on the various setups, this thesis would not exist. I am thankful for the helpful discussions with Dr. Vladilen Goldberg. I would also like to thank Dr. Charles Folden III, Dr. Jeremy Holt and Dr. Dan Melconian for serving on my committee.

I could not have done this without the help and support from my friends Heshani Jayatissa and Sriteja Upadhyayula. It has been a blast to work with you two on all of our various experiments and to keep me sane. I would also like to acknowledge other members of my group that have helped me tremendously including Dr. Ethan Uberseder and Dr. Sunghoon (Tony) Ahn.

Finally, I want to express my gratitude toward the staff members at the Cyclotron Institute at Texas A&M University for keeping the beam going for my experiments.

CONTRIBUTORS AND FUNDING SOURCES

Contributors

This work was supported by a dissertation committee consisting of Professors Rogachev, Holt and Melconian of the Department of Physics and Astronomy and Professor Folden III of the Department of Chemistry.

All work conducted for the dissertation was completed by the student independently.

Funding Sources

Graduate study was supported by teaching and research assistantships from Texas A&M University.

TABLE OF CONTENTS

Page

ABSTRACT ii

DEDICATION iv

ACKNOWLEDGMENTS v

CONTRIBUTORS AND FUNDING SOURCES vi

TABLE OF CONTENTS vii

LIST OF FIGURES ix

LIST OF TABLES xv

1. INTRODUCTION 1

    1.1 Nuclear Reactions 2
    1.2 R-Matrix Theory 6
    1.3 Nuclear Shell Model 10
    1.4 *Ab Initio* Nuclear Models 14
        1.4.1 No-Core Shell Model 14
        1.4.2 Quantum Monte Carlo Calculations 15
    1.5 Experimental Techniques 16
    1.6 Summary 20

2. STRUCTURE OF ^{10}N 21

    2.1 The Halo Nucleus ^{11}Li 21
    2.2 Structure of ^{10}Li 23
        2.2.1 Theoretical Calculations 23
        2.2.2 Previous Experimental Results 24
    2.3 ^{10}Li's Mirror Nucleus: ^{10}N 29
    2.4 Experimental Setup 33
        2.4.1 The Momentum Achromat Recoil Spectrometer (MARS) 33
        2.4.2 Experimental Setup and Procedures 35
    2.5 Experimental Procedures 39
        2.5.1 Calibration of the Detectors 40
        2.5.2 Particle Identification of the Beam 43
        2.5.3 Selecting Proton Scattering Events 45

2.5.4 Reconstructing Punch-through Events 48
2.5.5 Measured Excitation Function and R-matrix Analysis 50
2.5.6 Location of the 2s-shell in ^{10}Li 56
2.6 Conclusion 58

3. STRUCTURE OF ^{9}C 59

3.1 Introduction 59
3.2 Previous Studies of ^{9}C 59
3.3 Theoretical Calculations 65
3.4 Experimental Setup 65
3.4.1 The Texas Active Target Detector 67
3.4.1.1 General Electronics for TPCs 71
3.5 Data Analysis 72
3.5.1 Baseline Corrections and Obtaining the Energy and Timing 72
3.5.2 Chain and Strip Matching 73
3.5.3 Track Reconstruction - Hough Transform 74
3.5.4 Alpha Source Test in Gas 76
3.6 Experimental Procedures 81
3.6.1 Beam Particle Identification 81
3.6.2 Tuning of the beam 83
3.6.3 Low and High Gain Areas in the Micromegas Detector 84
3.6.4 Selecting Proton Events 84
3.6.5 Removing Inelastic Scattering Events 85
3.6.6 Vertex Reconstruction in the Central Region 88
3.6.7 Vertex Reconstruction in the Side Regions 89
3.6.8 Measured Excitation Function and R-matrix Analysis 91
3.7 Conclusion 93

4. CONCLUSION 98

4.1 Future Outlook 98

REFERENCES 100

LIST OF FIGURES

FIGURE Page

1.1 Kinematics of the binary nuclear reaction $A(a,b)B$ for the laboratory and center-of-mass coordinate systems [1]. Reprinted with permission from [1]. ... 4

1.2 The shell model and magic numbers for the Woods-Saxon potential on the left and the Woods-Saxon potential with the spin-orbit term [2]. Reprinted with permission from [2]. ... 12

1.3 Excitation energies of ^{6}Li obtained up to $14\hbar\Omega$ basis space compared to experimental values [3]. Reprinted with permission from [3]. ... 15

1.4 GFMC propagation in imaginary time for four $J^\pi = 5/2^-$ states in ^{7}Li [4]. Reprinted with permission from [4]. ... 17

1.5 GFMC calculations for the ground state and excited states of light nuclei. The calculations are shown with and without the three-body force IL7 [4]. Reprinted with permission from [4]. ... 18

2.1 Low mass region of the Serge chart highlighting the two neutron halo systems [5]. Reprinted with permission from [5]. ... 22

2.2 RMS radii of the Li isotopes plotted with the normal $R \sim A^{1/3}$ that is found in stable nuclei. ... 22

2.3 Calculations of the excitation energies of ^{10}Li using the NCSM with the CD-Bonn 2000 NN potential.[6]. Reprinted with permission from [6]. ... 24

2.4 Differential cross section as a function of relative energy between the ^{9}Li and neutron. The thin solid curve represents the virtual s-wave state, the dashed curve is the p-wave state and the dotted curve is the d-wave state [7]. Reprinted with permission from [7]. ... 26

2.5 Spectrum of ^{10}Li using the d(^{9}Li,p) reaction. A virtual s-wave state was needed to reproduce the data with a p-wave state at $E = 0.38$ MeV [8]. Reprinted with permission from [8]. ... 27

2.6 Spectrum of ^{10}Li via d(^{9}Li, p) at 100 MeV between c.m. angles $\theta_{\text{c.m.}} = [5.5°, 16.5°]$. The solid black line is the sum of the partial wave contributions from theoretical calculations matching the experimental data [9]. Reprinted with permission from [9]. 28

2.7 Spectrum of ^{10}Li using the p(^{11}Li, d) reaction. A p-wave state at $E = 0.62$ MeV was needed to reproduce the measured data [10]. Reprinted with permission from [10]. 29

2.8 (Top) Spectrum from the (^{14}N, ^{14}B) reactions on the ^{10}B, ^{11}B and ^{16}O target. (Bottom) Spectrum after subtracting the counts from the target contaminants [11]. Reprinted with permission from [11]. 31

2.9 (Top) Subtracted background fitting with the sum of three (dotted) and four (dashed) body fragmentation background. (Bottom) Fit of the peak with a Breit-Wigner resonance [11]. Reprinted with permission from [11]. 32

2.10 Overview of the MARS facility. 33

2.11 Result of the ^{9}C production on MARS showing the main contaminant of ^{3}He and some ^{4}He [12]. Reprinted with permission from [12]. 35

2.12 Sketch of the scattering chamber. The BC-404 scintillator is placed in front of the scattering chamber and is observed by two PMTs. A Havar window of 4 μm thickness separates the gas volume and the beam line. A windowless ionization chamber is installed at the entrance of the scattering chamber. An array of proportional wire cells and a set of silicon detectors are located downstream in the chamber. 37

2.13 Diagram of the MSQ25-1000 silicon detectors. 40

2.14 Readout scheme of the experimental setup. 41

2.15 Signals measured in a proportional counter cell using equidistantly spaced pulsar signals. The equidistant pulsar signals bunch together at higher channels due to the logarithmic pre-amplifier. 42

2.16 Ionization chamber energy vs the scintillator energy. We can clearly defined the ^{3}He, ^{4}He backgrounds and cut on the ^{9}C beam. 44

2.17 Cut made on the timing from the PMTs vs the energy in keV measured in the Si detectors. Punch-through proton events occur in the bottom left of the cut. 46

2.18 Specific energy loss deposited on the proportional counter cells (dE) plotted against the energy measured in the Si detectors. 47

2.19 The three regions of the dE vs E is shown. The green region is the non-punch-through region where the protons are fully stopped in the Si detector. The blue region are the punch-through events and the red region is the 'mixed' region. 48

2.20 The incident proton energy (pre-silicon energy) plotted against the measured proton energy at an incident angle of 0.2 rad. 49

2.21 Schematic of the three different angular regions for obtaining the excitation function. The 'Forward Angle' region consist of events in the zero degree detector, the 'First Ring' region are the next four quadrants outside of the zero degree detector and the 'Second Ring' are the four most outside Si quadrants. 52

2.22 Spectrum of protons from the ^{9}C+p resonance scattering for the first ring [13]. Reprinted with permission from [13]. 53

2.23 Spectrum of protons from the ^{9}C+p resonance scattering at three different angular regions. The red dash-dotted line in (b) is the Rutherford scattering cross section, the blue dashed line is the best fit with $J^{\pi} = 2^{-}$ as the ground state and a $J^{\pi} = 1^{-}$ state as the 1st excited state. The green solid line is the best fit with a $J^{\pi} = 1^{-}$ ground state and a $J^{\pi} = 2^{-}$ 1st excited state. The dotted magenta curve is the R-matrix calculation assuming that there are no resonances in the ^{9}C+p system, and that the cross section is defined by the repulsing hard sphere phase shift. The black dash-dotted curve is the fit with a $J^{\pi} = 2^{-}$ g.s., a $J^{\pi} = 1^{-}$ 1st excited and a $J^{\pi} = 1^{+}$ state at 3.3 MeV [13]. Reprinted with permission from [13]. 55

2.24 Excitation function of the First Ring. R-matrix calculations were performed for a single $J^{\pi} = 2^{-}$ state (solid red curve) and a $J^{\pi} = 1^{+}$ ground state with a $J^{\pi} = 1^{-}$ first excited state (green dashed line) [13]. Reprinted with permission from [13]. 57

3.1 Energy spectrum from ^{12}C(^{3}He, ^{6}He)^{9}C. ^{9}C ground state is at channel number 490 [14]. Reprinted with permission from [14]. 60

3.2 Spectra from the ^{12}C(^{3}He, ^{6}He)^{9}C reaction. Top and bottom panels are two different field settings. FS is the field setting of the splitpole spectrometer and Q is the total charge of the beam. Top panel is the ground state and the bottom panel shows the first excited state of ^{9}C at 2.2 ± 0.1 MeV [15]. Reprinted with permission from [15]. 61

3.3 Measured raw excitation function of ^{9}C [16]. Peak A corresponds to events not from elastic scattering while B are events from elastic scattering. Reprinted with permission from [16]. 62

3.4 Excitation function of ^{9}C subtracting backgrounds. R-matrix calculations are shown and the best fit to the data is the known $J^\pi = 1/2^-$ state plus a $J^\pi = 5/2^-$ state at 3.6 MeV [16]. Reprinted with permission from [16]. 63

3.5 Excitation function of ^{9}C with R-matrix fits including $J^\pi = 1/2^-$, $J^\pi = 5/2^-$ and $J^\pi = 3/2^-$ resonances [16]. Reprinted with permission from [16]. 64

3.6 Invariant-mass spectrum of ^{9}C. Blue dashed and green dotted line are R-matrix calculations for a $J^\pi = 1/2^-$ and $J^\pi = 5/2^-$ respectively [17]. Reprinted with permission from [17]. 65

3.7 Shell model prediction for p-shell states in ^{9}C. Level energies are in MeV [18]. Reprinted with permission from [18]. 66

3.8 Designed TexAT Assembly with one side removed. The top part is the Micromegas where the red portion depicts the central pads and the green are the side regions. The Si detectors (yellow) are each backed by a CsI (turquoise) detector. The beam travels from right to left along the central pads [19]. Reprinted with permission from [19]. 67

3.9 Schematic of the Micromegas detector and the sizes are not-to-scale. 68

3.10 TexAT Micromegas Design. The Micromegas consists of three regions: the left, the central and the right [19]. Reprinted with permission from [19]. 69

3.11 Picture of the Micromegas readout plane showing the detection pads. Shows the rows of the central pads consisting of six columns. The strips in the side planes are the solid readout pads that are perpendicular to the beam axis while the chains are the square readout pads in the side regions that go along the beam axis. 69

3.12 Schematic of the Forward Si Array. The center of the chamber along the beam axis is (0, 0) in this diagram. All measured distances are in mm. 70

3.13 (Left) Example waveforms of the four FPN channels. (Right) Raw Waveforms without any FPN or background subtraction. 73

3.14 Waveforms corrected with FPN and background subtraction. 74

3.15 An example of matched chains and strips for a single event that can then be used to reconstruct a track. 75

3.16 Diagram of the d, θ parameters in two dimensions. 76

3.17 (Top) A straight line (blue points) with scattering noise (orange). (Bottom) The Hough space of the top points. Outlined in the red is the minimal standard deviation of d corresponding to the straight line of blue points. 77

3.18 An accumulation of the alpha source tracks in the XY-plan in the forward and side walls. 0 mm on the y-axis corresponds to the beginning of the Micromegas plate. All of the tracks converge to ~ -60 mm where the source was located. . 78

3.19 The XZ projection of the forward Si wall. 79

3.20 (Top) XZ projection of the Si wall choosing the lower left and upper right quadrants of each Si detector. (Bottom) XZ projection of the Si wall choosing the upper left and lower right quadrants of each Si detector. 80

3.21 (Top) The energy of the ionization chamber. The ^{8}B peak is located between channels 1300-1900. (Bottom) The time of the maximum of the ionization chamber. The beam particles corresponding to the Si hit fall between 5400 ns to 6500 ns. 82

3.22 The cumulative counts in the central region of the Micromegas during the beam tuning. The pressure was adjusted to stop the beam about 1/8th from the end of the Micromegas. 83

3.23 The energy deposited in each of the central region pads. The Bragg peak occurs around row number 90. 84

3.24 The specific energy loss per unit pad in the central region plotted against the total energy measured in the Si and CsI detector. The energy loss is measured in the last 1/8th in the central pads. Protons are clearly defined and a gap in spectrum between 9 and 10 MeV occur do to a threshold effect in the CsI. . 86

3.25 The specific energy loss per unit pad of the strips in the side region plotted against the total energy measured in the Si and CsI detector. Protons are the only particle than can be identified in the spectrum. 86

3.26 The energy recorded in the CsI detector in channel number plotted against the measured energy (in keV) in the Si detector. Only proton events punch-through the Si detector to deposit energy in the CsI. 87

3.27 Inelastic events where a proton is measured in one side of the Micromegas plate and a proton in the central region. 88

3.28 Inelastic events where protons are measured in both sides of the Micromegas plate. 88

3.29 Specific energy loss of the beam and heavy scattered recoil vs. row number in Micromegas along the beam axis. Black lines are the raw energy values while the red curve is the running average. (Left) The vertex location is around row 20 while the maximum specific energy loss is around row 50. (Right) The vertex location is around row 30 while the maximum specific energy loss is around row 60. 90

3.30 Vertex position vs. total energy measured in the Si and CsI detectors for the central forward detectors. The gap between energies 9 and 10 MeV occur due to a threshold effect for the CsI detectors. 90

3.31 Vertex position vs total energy measured in the Si and CsI detectors for the outside forward detectors. The gap between energies 12 and 13 MeV occur due to a threshold effect for the CsI detectors. 91

3.32 Cross section vs. excitation energy for the center forward detectors (top) and outside forward detectors (bottom) for ^{8}B + p resonance elastic scattering. 94

3.33 R-matrix calculations and experimental data for both regions. The black solid line are the three states from [16]: the $J^{\pi} = 1/2^{-}$, $J^{\pi} = 5/2^{-}$ and $J^{\pi} = 3/2^{-}$ states. The blue dash-dotted curve include the $J^{\pi} = 1/2^{-}$, $J^{\pi} = 5/2^{-}$ and $J^{\pi} = 7/2^{-}$. The green dashed curve includes the $J^{\pi} = 1/2^{-}$, $J^{\pi} = 5/2^{-}$ and $J^{\pi} = 5/2^{+}$ while the red dotted curve is the same configuration but with an added $J^{\pi} = 7/2^{-}$ state. 95

3.34 R-matrix calculations and experimental data for both regions. All three calculations include the $J^{\pi} = 1/2^{-}$, $J^{\pi} = 5/2^{-}$ and $J^{\pi} = 7/2^{-}$ states. The blue solid curve is the $J^{\pi} = 1/2^{+}$ state, the green dashed curve is the $J^{\pi} = 3/2^{+}$ state while the red dotted line the $J^{\pi} = 5/2^{+}$ state. 96

LIST OF TABLES

TABLE Page

2.1 R-Matrix parameters for the best fit of the ground state and first excited state in ^{10}N. For both configurations, the spin-parity assignment, the c.m. energy, the total width of the state, and the dimensionless reduced width are shown. 56

1. INTRODUCTION

Nuclei are made up of neutrons and protons, referred to as nucleons, and are held together by the strong interaction. To learn more about the strong interaction, we can ask ourselves what combinations of neutrons and protons can bind together to create nuclei and what are the properties of those nuclei. The stability of nuclei is determined by the balance of the attractive nuclear (strong) force and the repulsive Coulomb interaction. In light nuclei (less than $\sim$40 nucleons) the role of Coulomb repulsion is relatively small and nuclides that are most stable tend to have equal numbers of protons and neutrons. Light nuclei that have significant excess of either protons or neutrons are referred to as exotic nuclei. This is not only due to the fact that these nuclei have short half-lifes (the amount of time it takes for half of its nuclei to decay), but also because they often have unusual structure and exhibit features not found in stable nuclei. Exotic decay modes, increased root-mean-square radii, halo phenomena, and evolution of nuclear shell structure with increasing imbalance between protons and neutrons are all examples of these unusual and often unexpected features that have already been observed in exotic nuclei. High-quality experimental data on these nuclei provide a better understanding of properties of nuclear interactions and guide development of contemporary nuclear structure models.

With ion beams of only stable isotopes, the experimental study of exotic nuclei has been limited to complex multi-nucleon transfer reactions until recently. These reactions often have low cross sections and are difficult for theoretical analysis. With the development of radioactive ion beams (RIBs) three decades ago, the study of these exotic nuclei can be done using simpler reactions such as elastic and inelastic scattering and transfer reactions. These reactions are well understood and have a much more favorable cross section than multi-nucleon transfer reactions. However, experiments with RIBs have challenges. One of the problems is that the intensities of RIBs are orders of magnitude lower than intensities of stable beams. In addition, many RIBs are created using the in-flight approach. RIBs

created in this way generally have energy and angular resolution significantly worse than stable beams. Development of new experimental techniques is necessary to take advantage of the scientific opportunities offered by RIBs.

The focus of this thesis is to study the structure of two proton-rich nuclei: ^{10}N and ^{9}C. The structure of these two nuclei provide excellent tests for nuclear models and both of these light nuclei are accessible ab-initio calculations. The structure of ^{10}N can provide insight into the structure of its mirror nucleus, ^{10}Li, that plays an important role in the two-neutron halo ^{11}Li. The main goal in studying structure of ^{9}C was to search for new states (in particular positive parity states to locate the 2s shell) in this exotic carbon isotope, as well as to commission the new Texas Active Target detector with this experiment. Both of these nuclei were studied using resonance scattering with protons in active target time projection chambers. By measuring the excitation functions for ^{9}C+p and ^{8}B+p resonance scattering and applying the R-matrix formalism for theoretical analysis, the level structure of these nuclei can be established.

1.1 Nuclear Reactions

Nuclear structure can be studied through various experimental techniques using nuclear reactions involving a beam on a target nuclei. These reactions can add or remove nucleons from either the beam or target nuclei or a compound nucleus can be formed where the target and beam ions merge into one and then subsequently decay. In this study we use the latter process, the formation of compound nucleus, to populate states in ^{10}N and ^{9}C using resonance elastic scattering of ^{9}C and ^{8}B incident RIB on a proton target and briefly forming ^{10}N and ^{9}C, respectively.

A binary nuclear reaction involve a projectile a incident on a target A producing two products, b and B. This reaction can be expressed in two different notations

$$a + A \rightarrow b + B \tag{1.1}$$

or more compactly

$$A(a,b)B \tag{1.2}$$

We can classify different types of reactions based on their entrance and exit channels. A channel is a set of specific nuclei in specific states. Nuclear reaction is called elastic scattering if the entrance and exit channels are identical, or inelastic scattering if one (or both) of the participating nuclei emerge in an excited state. Another type of reactions are transfer reactions which involve the transfer of one or more nucleons between the projectile and the target.

The total energy must be conserved in any reaction process, and in non-relativistic case of binary nuclear reaction this is given by the following expression:

$$E_A + m_A c^2 + E_a + m_a c^2 = E_b + m_b c^2 + E_B + m_B c^2 \tag{1.3}$$

where $E_i = \frac{1}{2} m_i v_i^2$ is the non-relativistic kinetic energy and $m_i c^2$ is the mass at rest of particle i. Non-relativistic kinematics can be used in these calculations because the kinetic energies for each particle will be much less than their mass. By labeling the sum of kinetic energies of the particles in the entrance and exit channels as E_α and E_β respectively, we can rewrite equation 1.3 as

$$E_\alpha + Q = E_\beta \tag{1.4}$$

where Q is the Q-value of the reaction and is determined by the difference of rest masses of the entrance and exit channels:

$$Q = \left(m_A + m_a - m_b - m_B\right) c^2 \tag{1.5}$$

When $Q > 0$, the reaction is called exothermic and energy is released as additional kinetic energy of the exit channel products while when $Q < 0$, the reaction is endothermic and energy needs to be supplied to create the products [2].

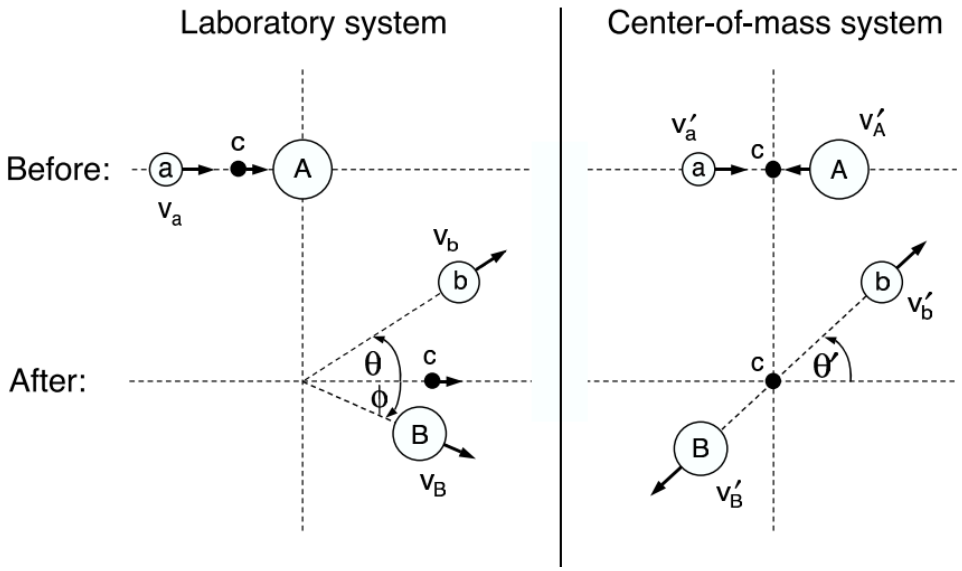

Figure 1.1: Kinematics of the binary nuclear reaction $A(a,b)B$ for the laboratory and center-of-mass coordinate systems [1]. Reprinted with permission from [1].

Is it useful to change the reference frame from the laboratory frame to the center-of-mass frame (c.m.). Figure 1.1 shows the laboratory and c.m. frames for a binary nuclear reaction. The c.m. velocity is a Galilean transformation between the laboratory and c.m. frames and defined as

$$v_{\text{c.m.}} = \frac{m_a v_a + m_A v_A}{m_a + m_A} = \frac{m_a}{m_a + m_A} v_a \tag{1.6}$$

where a is the projectile (or beam) and A is the target nucleus which is at rest in the laboratory frame (v_A=0). The c.m. energy can then be written as

$$E_{\text{c.m.}} = \frac{m_A}{m_a + m_A} E_a \tag{1.7}$$

Elastic scattering is the simplest process and the one used in this study. In elastic scattering, the amount of energy released (Q-value) is zero and the total kinetic energy of the system is conserved. Elastic scattering provides a relatively simple way to study nuclei and their properties. One method to study nuclei using elastic scattering involves measuring the cross section as a function of energy - excitation function. A cross section is a

measurement of the probability of a nuclear reaction to occur. Cross sections are measured in barns where 1 barn (b) = 10^{-24} cm^2 [2]. Differential cross section $d\sigma/d\Omega$ gives a dependence of a cross section on scattering angle and is defined as the probability per unit solid angle $d\Omega$ that an incident particle is scattered at. Experimentally, the differential cross section in the laboratory frame of reference can be determined as

$$\frac{d\sigma}{d\Omega}_{\text{lab}} = \frac{N}{N_{\text{inc}} T_{\text{t}} \Delta\Omega} \tag{1.8}$$

where N is the number of scattered particles measured at a given solid angle $\Delta\Omega$, N_{inc} is the number of incident nuclei, and T_{t} is the number of target nuclei per cm^2. In the case of elastic scattering in inverse kinematics (heavy beam on light target) that was used for all measurements described in this thesis, the c.m. cross section can be calculated from the laboratory frame cross section by

$$\frac{d\sigma}{d\Omega}_{\text{c.m.}} = \frac{1}{4\cos\theta} \frac{d\sigma}{d\Omega}_{\text{lab}} \tag{1.9}$$

where θ is the laboratory scattering angle of the light particle. This conversion factor can be derived from energy and momentum conservation.

Using scattering theory, the differential elastic scattering cross section can be written as

$$\left(\frac{d\sigma}{d\Omega}\right)_{\text{elastic}} = \frac{1}{4k^2} \left| \sum_{\ell=0}^{\text{inf}} (2\ell+1)(1 - e^{2i\delta_\ell}) P_\ell(\cos\theta) \right|^2 \tag{1.10}$$

$$= \frac{1}{k^2} \left| \sum_{\ell=0}^{\text{inf}} (2\ell+1) \sin\delta_\ell P_\ell(\cos\theta) \right|^2 \tag{1.11}$$

where $P_\ell(\cos\theta)$ are the Legendre polynomials and δ_ℓ is the partial wave phase shift [1]. For elastic scattering of charged particles Coulomb interaction plays an important role. The cross section for just the Coulomb potential (known as the Rutherford cross section) for an

infinite sized target is given by

$$\frac{d\sigma}{d\Omega_{\text{c.m.}}} = \left(\frac{Z_1 Z_2 \alpha \hbar c}{4E}\right)^2 \frac{1}{\sin^4(\frac{\theta}{2})} \tag{1.12}$$

where Z_1 and Z_2 are the charges of the two incident particles, E is the energy of projectile and α is the fine structure constant.

Sharp peaks can be observed in the excitation function at certain energies. These peaks correspond to unbound excited states (resonances) in a compound nucleus. Resonance width, Γ, is related to its lifetime, τ

$$\Gamma \sim \frac{\hbar}{\tau} \tag{1.13}$$

where $\hbar = 6.58 \times 10^{-16}$ eV·s is the reduced Planck constant. Thus, the wider the resonance, the shorter its half-life. The total elastic scattering cross section of neutral spin zero particles for a single isolated resonance with a resonance energy of E_r and width Γ is given by

$$\sigma_{\text{elastic}} = \frac{4\pi}{k^2}(2\ell + 1)\frac{\Gamma^2/4}{(E - E_r)^2 + \Gamma^2/4} \tag{1.14}$$

This is called the Breit-Wigner formula [1].

1.2 R-Matrix Theory

R-Matrix theory was introduced by Wigner and Eisenbud in 1947 and described by Lane and Thomas in 1958 [20, 21]. R-matrix theory can be split into two classifications: the calculable R-matrix and the phenomenological R-matrix. The calculable R-matrix provides a way of solving the Schrödinger equation for positive and negative energies. The phenomenological R-matrix method uses a parametrization to reproduce cross section data without solving the Schroödinger equation. This method has been successfully applied to analyze huge body of experimental data and is not limited to just elastic scattering but can also be used in inelastic scattering and transfer reactions that proceed through a formation of compound nucleus. In this study, we use the phenomenological R-matrix theory.

Lets consider the case of a single channel and solve the radial Schrödinger equation for partial wave l

$$(H_l - E)u_l = 0 \tag{1.15}$$

where u_l is the radial component of the wave function and the radial Hamilton H_l is defined as

$$H_l = T_l + V(r) \tag{1.16}$$

The operator T_l for a reduced mass μ is given by

$$T_l = -\frac{\hbar^2}{2\mu}\left(\frac{d^2}{dr^2} - \frac{l(l+1)}{r^2}\right) \tag{1.17}$$

and $V(r)$ is the central potential. We divide the space in R-matrix theory into two regions, an external region where we assume only the Coulomb force and an internal region. The two regions are matched at the channel radius, a, and require that the wave functions are continuous, $u_l^{\text{int}}(a) = u_l^{\text{ext}}(a)$ and $u_l^{\text{int}'}(a) = u_l^{\text{ext}'}(a)$. The channel radius has to be chosen large enough so that the nuclear force can be neglected beyond it, and the total potential $V(r)$ in the entire external region can be well approximated by the Coulomb potential. In the external region, the wave function can be expressed in terms of F_l and G_l which are the regular and irregular Coulomb functions and δ_l is the phase shift, as

$$u_l^{\text{ext}}(r) = \cos\delta_l F_l(kr) + \sin\delta_l G_l(kr) \tag{1.18}$$

or,

$$u_l^{\text{ext}}(r) = I_l(r) - U_l O_l(r) \tag{1.19}$$

where I_l and O_l are the incoming and outgoing waves respectively and U_l is the collision or scattering matrix. We can express U_l in terms of the phase shift δ_l

$$U_l = e^{2i\delta_l} \tag{1.20}$$

The phase shift for the lth partial wave and channel radius a can be written as

$$\tan\delta_l = -\frac{F_l(ka) - kaR_l(E)F_l'(ka)}{G_l(ka) - kaR_l(E)G_l'(ka)} \tag{1.21}$$

where $R_l(E)$ is the R-matrix. We can relate the scattering matrix U_l with the R-matrix by

$$U_l = \frac{I_l(ka) - kaR_l(E)I_l'(ka)}{O_l(ka) - kaR_l(E)O_l'(ka)} \tag{1.22}$$

or

$$U_l = e^{2i\phi_l}\frac{1 - L_l^* R_l(E)}{1 - L_l R_l(E)} \tag{1.23}$$

where ϕ_l is the hard-sphere phase shift

$$\phi_l = -\arctan[F_l(ka)/G_l(ka)] \tag{1.24}$$

and L_l is the logarithmic derivative of the outgoing flux O_l at the channel radius,

$$L_l = ka\frac{O_l'(ka)}{O_l(ka)} \tag{1.25}$$

L_l^* is defined as the conjugate of L_l.

In case of only one open channel (elastic scattering) the R-matrix (or R-function for one channel) for N states is defined as

$$R(E) = \sum_{n=1}^{N}\frac{\gamma_n^2}{E_n - E} \tag{1.26}$$

where E_n are the energy eigenvalues and γ_n are the formal reduced widths. When other channels are present, the R-function becomes the R-matrix given by

$$R_{cc'}(E) = \sum_{n=1}^{N}\frac{\gamma_{nc}\gamma_{nc'}}{E_n - E} \tag{1.27}$$

for channels c and c'. These can be used to calculate the observed resonance energies E_R and widths Γ_R. The formal reduced width can be related to the observed reduced width γ_R by

$$\gamma_r^2 = \frac{\gamma_R^2}{1 - \gamma_R^2 S_l'(E_R)} \tag{1.28}$$

Then we can relate the observed reduced width to the observed width Γ_R

$$\Gamma_R = 2P_l(E_R)\gamma_R^2 \tag{1.29}$$

The observed resonance energy E_R can be calculated from the formal resonance energy by

$$E_R = E_r - \gamma_r^2 S_l(E_r) \tag{1.30}$$

In Equations 1.28, 1.29 and 1.30, P_l is the penetration factor, S_l is the shift factor and S_l' is the energy derivative of the shift function. The penetration factor and shift factor are defined in terms of the regular and irregular Coulomb function and their derivatives:

$$P_l(E) = \frac{ka}{F_l^2(ka) + G_l^2(ka)} \tag{1.31}$$

$$S_l(E) = ka\frac{F_l(ka)F_l'(ka) + G_l(ka)G_l'(ka)}{F_l^2(ka) + G_l^2(ka)} \tag{1.32}$$

The penetration factor P_l is not the same as the Legendre polynomial and describes the penetration through the Coulomb barrier. The shift factor causes observed resonance energy to change from the formal resonance energy. We can then calculate the scattering amplitude $f(\Omega)$, the Coulomb scattering amplitude $f_C(\Omega)$ and subsequently the cross section for elastic scattering using the collision matrix by

$$f(\Omega) = \frac{1}{2ik}\sum_{l=0}^{\infty}(2l+1)e^{2i\sigma_l}(U_l - 1)P_l(cos\theta) \tag{1.33}$$

$$f_{\mathrm{C}}(\Omega) = -\frac{\eta}{2k\sin^2(\theta/2)} e^{2i(\sigma_0 - \eta \ln \sin(\theta/2))} \tag{1.34}$$

$$\frac{d\sigma}{d\Omega} = |f_{\mathrm{C}}(\Omega) + f(\Omega)|^2 \tag{1.35}$$

where σ_l is the Coulomb phase shift, k is the wavenumber defined as $k = \sqrt{2\mu E}/\hbar$ and η is the Sommerfeld parameter.

For each state, we can use the ratio of the observed reduced width, γ_R, to the so called Wigner limit (γ_W^2) to probe the nature of the state [22]. The Wigner limit is defined as

$$\gamma_W^2 = \frac{\hbar^2}{\mu a^2}, \tag{1.36}$$

and the ratio of the observed reduced width and the Wigner limit is the dimensionless reduced width:

$$\theta^2 = \frac{\gamma_R^2}{\gamma_W^2}. \tag{1.37}$$

A value of $\theta^2 \sim 1$ indicates that the state is of cluster nature and the two colliding nuclei conserve their identity within the resonance [22]. θ is not to be confused with the angle. In the case of proton elastic scattering on a nucleus, this means that a resonance with a unity dimensionless reduced width is a single-particle (single proton) state that can be described as a core nucleus in its ground state plus a proton occupying specific (sub)shell. General discussion of nuclear shell model is given in the next paragraph.

1.3 Nuclear Shell Model

The nuclear shell model was created to try to explain the structure of nuclei based on the success of the shell model for atomic physics. Similar to atomic physics, the nucleons in the nucleus are organized into shells. The shells are organized by their quantum numbers. The principal quantum number n determines the number of nodes in the radial wave function, l and j are the orbital and total angular momenta. The orbital angular momentum l is

denoted by s, p, d, f, g, h, ... for $l = 0, 1, 2, 3, 4, 5, \ldots$ and the total angular momentum is $j = l \pm s$ where $s = \frac{1}{2}$ is the intrinsic spin of the nucleons (both neutrons and protons). The degeneracy of each level is $2(2l + 1)$ arising from the m_l degeneracy of $(2l + 1)$ and the spin degeneracy m_s for the factor of 2. The notation for shells in the shell model is $n\ l_j$. So for a nucleon with quantum numbers $n = 2$, $l = 1$ and $j = 3/2$ is written as $2\mathrm{p}_{3/2}$. A common notation is to also specify whether it is a neutron or proton by adding a ν or π receptively at the beginning of the notation. So a proton in the previous example would be written as $\pi 2\mathrm{p}_{3/2}$.

In general, the nuclear shell model provides a reasonable overall description of nuclear structure and reproduces the magic numbers observed in nuclei. The magic numbers manifest themselves in various ways. For example, one can notice that the nucleon separation energy has significant irregularities at certain proton or neutron numbers. There is a gradual increase until a discontinuity is observed. These discontinuities correspond to the filling of the major shells. The magic numbers are 2, 8, 20, 28, 50, 82 and 126 [2]. A harmonic oscillator potential does fairly well to reproduce the lower shell closings (up to 20) but a more realistic potential is the Woods-Saxon potential of the form

$$V(r) = \frac{V_0}{1 + \exp(r - R)/a} \tag{1.38}$$

where V_0 is the depth of the potential well, a is the diffuseness of the nuclear surface and R is the nuclear radius normally defined as $R = r_0 A^{1/3}$ where r_0 is normally chosen around $r_0 = 1.2$ fm. With this potential and the addition of the spin-orbit term, the magic numbers are well reproduced. Figure 1.2 shows the magic numbers for the Woods-Saxon potential and the Woods-Saxon potential with the spin-orbit term.

The spin and parity of spherical nuclei in their ground state can be determined from the shell model based on the number of neutrons and protons it has following these simple rules:

- Even-even nuclei have zero intrinsic spin and positive parity. The ground state of these

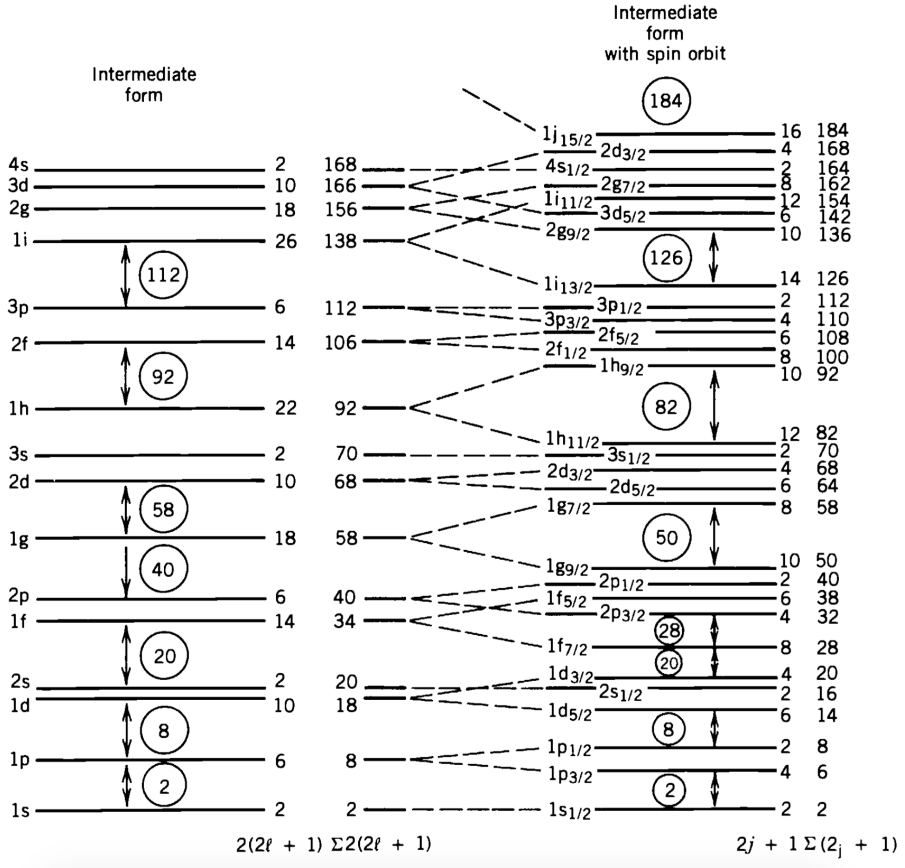

Figure 1.2: The shell model and magic numbers for the Woods-Saxon potential on the left and the Woods-Saxon potential with the spin-orbit term [2]. Reprinted with permission from [2].

nuclei will have a spin-parity of 0^+.

- Even-odd or odd-even nuclei have one unpaired nucleon and the spin-parity of the ground state is determined by the shell the unpaired nucleon is in. The spin is equal to the j-value of the shell it is in, and the parity is $(-1)^{\ell}$ where ℓ is the orbital angular momentum of the shell the unpaired nucleon is in.

- For odd-odd nuclei there is an unpaired neutron and an unpaired proton with total angular momentum j_n and j_p respectively. The total spin of the nucleus is then the vector sum and take values between $|j_n - j_p|$ and $|j_n + j_p|$. The parity is given by $(-1)^{l_n+l_p}$ where l_n and l_p are the orbital angular momenta of the unpaired neutron and proton respectively.

By following these rules, we can determine the ground state spins-parities of nuclei close to or in the valley of stability very well. Once we go to the more exotic nuclei, the shell sequence may change. A popular example is ^{11}Be nucleus. In ^{11}Be, the $\nu 2s_{1/2}$ shell is below $\nu 1p_{1/2}$ and the spin-parity of the ground state becomes $1/2^+$, instead of the shell model prescribed $1/2^-$.

There are several shortcomings to the shell model. The model space in the shell model consists of three parts: the core, valence space and the external space. The inert core consists of fully filled orbitals, the valence space is where the particle-hole excitations occur while the external space is always empty. Residual interactions are two-body interactions that are necessary when two or more nucleons are in the valence space. These residual interactions are not part of the central potential, are treated as free parameters and phenomenological [23]. This means that the choice of experimental measurements used to calculate these residual interactions could bias the predictions of unexplored properties of nuclei. The development of *ab initio* methods is a significant recent theoretical breakthrough.

1.4 *Ab Initio* Nuclear Models

In important step in resolving the shortcomings of nuclear shell model was the development of *ab initio* quantum many-body methods that start from realistic two-body (NN) and three-body (NNN) nucleon interactions and provided a way to make robust nuclear structure calculations. Several of these methods include the no-core shell model (NCSM) [24, 25], Green's Function Monte Carlo (GFMC) [26, 27], Lattice Effective Field Theory (EFT) [28, 29, 30] and Coupled Cluster methods [31, 32, 33].

In these methods, the nuclear Hamiltonian for A-nucleons has the form

$$H = T + V = \sum_{i}^{A} T_i + \sum_{i>j=1}^{A} V_{ij} + \sum_{i>j>k=1}^{A} V_{ijk} \tag{1.39}$$

where V_{ij} is the two-body potential and V_{ijk} is the three-body potential. Some examples of realistic two-body nuclear interactions are the Argonne-v18 [34] and CD-Bonn [35] potentials. These two-body potentials are fit to pp, np and nn scattering as well as the deuteron binding energy. Three-body potentials such as the Urbana [36] and Illinois [26] are fit using properties of ^{3}H and ^{4}He. ^{3}H and ^{4}He are also used to calculate the coefficients in the higher order terms (3N+ interactions) in EFT.

Below I discuss two of the *ab intio* approaches in more detail to highlight differences from the conventional shell model and to demonstrate the variety in the theoretical routes that can be used to solve the quantum many-body problem.

1.4.1 No-Core Shell Model

The NCSM solves the nuclear many-body equation where all nucleons are active unlike the standard shell model where there is an inert core with valence nucleons [3]. The inert core for the standard shell model is used to reduce the model space but for light nuclei, a model space where all nucleons contribute is possible due to more computational power available within the last few decades. The NCSM solves the non-relativistic Schrödinger equation for

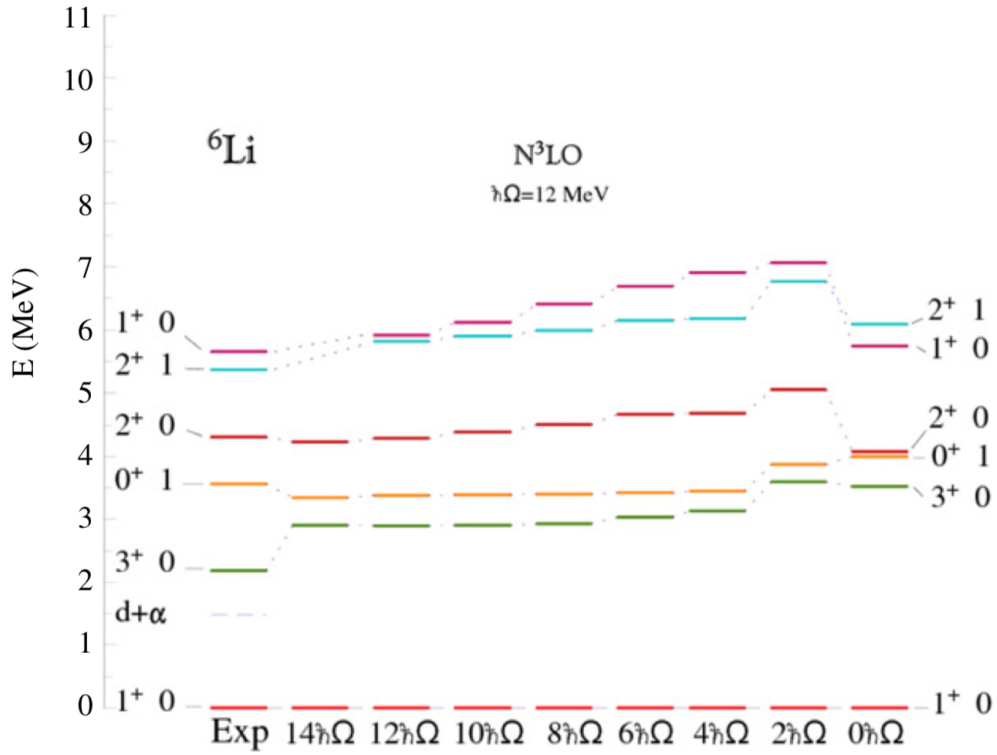

Figure 1.3: Excitation energies of ^{6}Li obtained up to $14\hbar\Omega$ basis space compared to experimental values [3]. Reprinted with permission from [3].

A interacting nucleons with a Hamiltonian including two and three-body potentials with the form of Eq. 1.39. To numerically solve the Schroödinger equation, the Hilbert space where the calculations are done needs to be truncated to a finite model space [3]. Thus, the model space contains all many-body states up to a maximum of $N_{\max}\hbar\Omega$ harmonic oscillator states. The calculations typically converge as this basis gets larger as shown in Figure 1.3. Figure 1.3 shows low lying states in ^{6}Li calculated for progressively larger model space. Although the energies for the excited states in ^{6}Li do not match the experimental values exactly, the level structure agrees with the measured level scheme reasonably well.

1.4.2 Quantum Monte Carlo Calculations

Quantum Monte Carlo (QMC) Methods such as the Variational Monte Carlo (VMC) and Green's Function Monte Carlo (GFMC) are a different type of approach when compared to

the NCSM. QMC has been proven to be valuable for calculating properties of light nuclei including level scheme, low-energy scattering and transitions [4]. Generally, a GFMC calculation starts with an initial VMC calculation. In VMC, one starts with a trial wave function Ψ_T with various parameters and minimizes the energy while changes these parameters [4]. The variational energy E_V is always greater or equal to the true ground state energy E_0 with this trial wave function:

$$E_V = \frac{\langle \Psi_T | H | \Psi_T \rangle}{\langle \Psi_T | \Psi_T \rangle} \tag{1.40}$$

When the trial wave function has been minimized with respect to the energy, it can be used in the more demanding GFMC calculations. The GFMC projects the wave function along an imaginary time τ by

$$|\Psi_0\rangle \propto \lim_{\tau \to \infty} \exp[-(H - E_0)\tau] \, |\Psi_0\rangle \tag{1.41}$$

An example of this propagation in imaginary time for four $J^\pi = 5/2^-$ states in ^{7}Li are shown in Figure 1.4.

The results of GFMC calculations of the ground state and excited states for light nuclei using the Argonne-v18 and Illinois-7 (IL7) potentials is shown in Figure 1.5. Included in Figure 1.5 are the calculations with (red and yellow) and without (blue) the three-body potential IL7. In this study, the experimental ground state energies are reproduced with a rms error of 0.36 MeV [4]. As expected, the excited states are not reproduced with such precision as the ground states for all nuclei but for most nuclei calculated in this study, the level structure is mostly reproduced. The GFMC technique has been successful in reproducing the level structure in light nuclei.

1.5 Experimental Techniques

RIBs have allowed the study of light nuclei outside the valley of stability without the use of techniques such as multi-nucleon transfer reactions that generally have low cross sections and complex reaction mechanisms [37]. As facilities all over the world have developed techniques to create these RIBs using Isotope Separation On-Line or in-flight methods, one clear

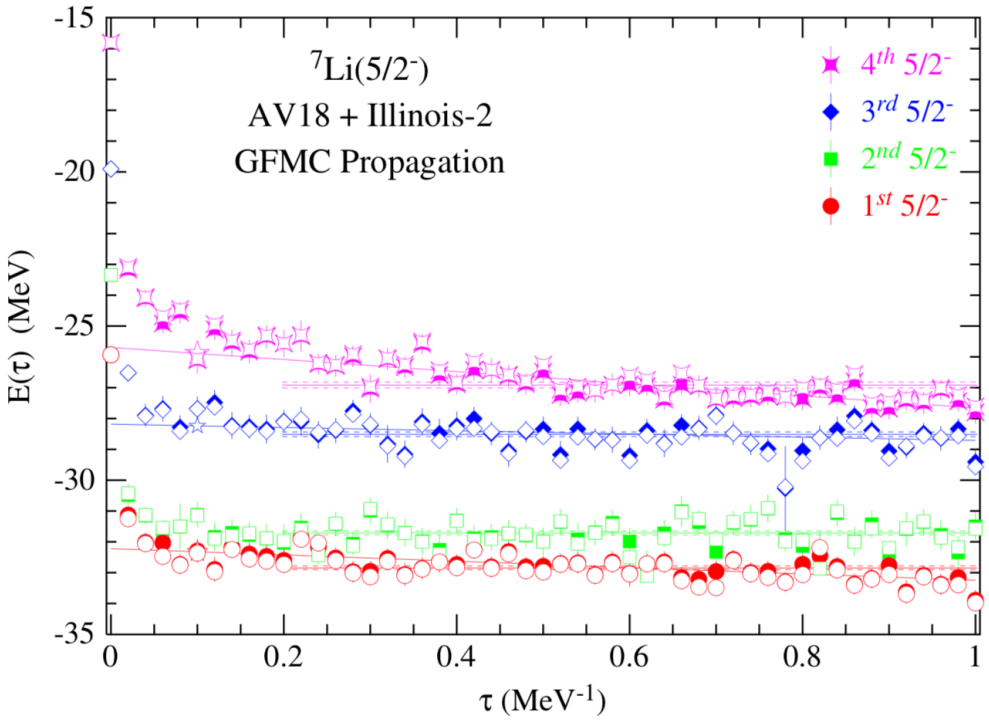

Figure 1.4: GFMC propagation in imaginary time for four $J^\pi = 5/2^-$ states in ^{7}Li [4]. Reprinted with permission from [4].

disadvantage to using these beams are the low intensities compared to stable beams. The intensities for RIBs are generally many orders of magnitude below stable beam intensities. With RIBs one can study light exotic nuclei using simple and well understood reactions, such as resonance elastic scattering, which have high cross sections. So even though RIBs have low intensities, studies on light exotic nuclei using powerful tools such as resonance elastic scattering can still achieve relatively good statistics needed for these measurements. Since the RIB intensities are so low, it is not ideal to use a thin solid target and change the beam energy to measure the excitation function. Instead we can use powerful techniques such as thick target inverse kinematics such that we can measure the full excitation function with one beam energy. This also saves time in the measurement that is lost due to re-tuning of the accelerator and magnets along the beam line.

Generally, thick target inverse kinematic techniques (TTIK) use a gas target instead of

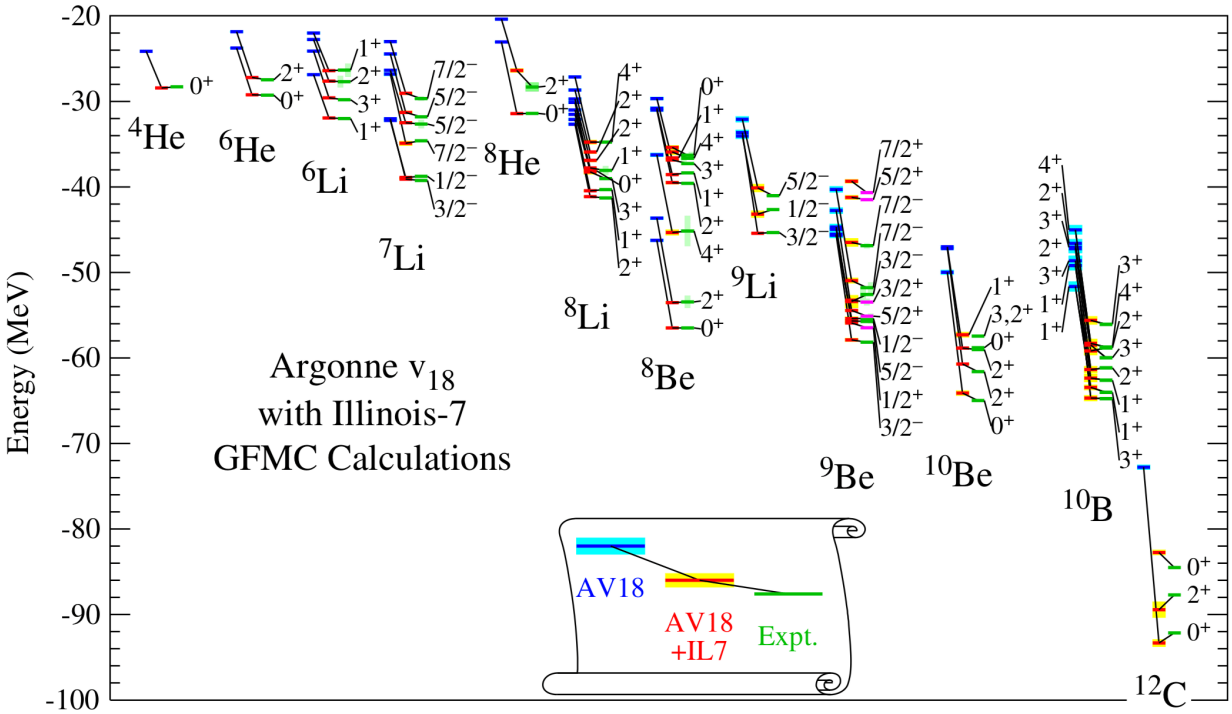

Figure 1.5: GFMC calculations for the ground state and excited states of light nuclei. The calculations are shown with and without the three-body force IL7 [4]. Reprinted with permission from [4].

a thick solid target and this technique was developed by Goldberg *et al.* [38, 39]. The TTIK method utilizes inverse kinematics where the heavy particle is the beam and the light particle is the target. This is also necessary since many radioactive nuclei decay too fast to be used as a target, hence the role of RIBs. As the heavy beam ion enters the chamber, the ion interacts within the target and losses energy. At any point in the target, the beam ion and target ion can interact and different types of scattering can occur. In the case of elastic scattering, the light recoil gains energy from the reaction. Generally, the chamber is filled with detectors to measure the light scattered recoil and the gas pressure is tuned such that the beam ion is stopped somewhere toward the end of the scattering chamber. The light ion can then be measured in the detectors due to the lower specific energy loss in the gas compared to the beam. Since the beam ion is losing energy as it moves further in the chamber, the energy of the interaction depends on the location of the interaction inside of the chamber.

In both of these studies we used active targets. Active targets utilize the TTIK technique but instead of the gas just being the target for the reaction, the gas is also a detector medium. As charged particles ionize the target gas creating electron-ion pairs and in most cases, the electrons are measured by a detector. The number of electron-ion pairs created depends on the specific energy loss of the charged particles within the volume cell and thus can be used in conjunction with other detectors to distinguish between particle species. Examples of recent measurements that used active targets include the structure of ^{9}He [40] and ^{10}Be [41].

Building on top of active targets are the use of time projection chambers (TPCs) which were developed in the 1970s by Nygren [42]. A TPC consists of an anode and a cathode producing an electric field. When the charged particle travels through the gas, it losses energy and ionizes the gas producing electron-ion pairs. With the electric field, these electrons drift toward the anode at a velocity determined by the gas properties and strength of the electric field. The anode is normally a position sensitive detector and produces a signal proportional

to the number of electrons that are collected. The electrons that are collected in the detector give information on the position in two-dimensions while the third dimension can be deduced from the time it takes to drift towards the detector. In TPCs, an uniform electric field is ideal for a constant drift velocity. This is so that the drift time can easily be transformed into the height above the detector using a linear function:

$$\text{height} = \text{drift velocity} * \text{time} + \text{offset} \tag{1.42}$$

With these three quantities, the 3-D track of the charged particles passing over the detector can be found.

The right choice of gas is needed for active targets. The gas chosen needs to have great properties for TPCs such as having good electron amplification, provide quenching and have a high stopping power as well as having the right nuclei for the reaction of interest. For proton elastic scattering, hydrogen is the obvious choice for the gas since it only contains protons but hydrogen gas does not have good properties for TPCs. Instead of using hydrogen gas, we can use methane (CH_4) or isobutane (C_4H_{10}) since they both have good properties for TPCs and contain protons (hydrogen). Carbon that is present in these gases can be a source of background, but since complete kinematics is measured in active targets, this background can often be eliminated in the offline analysis.

1.6 Summary

Many approaches to calculate the structure of nuclei have had success in reproducing observable but do not have the same success away from stability. The structure of two proton rich nuclei that are on either side of the proton drip line and far from stability, ^{10}N and ^{9}C, are the focus of this work. The outline for this dissertation for each of these nuclei are: The background and motivation for the experimental work, the experimental and theoretical techniques used in this study and the analysis procedure and results.

2. STRUCTURE OF ^{10}N

2.1 The Halo Nucleus ^{11}Li

One of the striking new phenomena that have been observed in exotic nuclei is nuclear "halo" - an extended spatial distribution of the wavefunction of a valence nucleon(s). Halos in atomic nuclei arise due to weak binding of the valence nucleon(s) (normally neutrons occupying s-orbitals) and decoupling of these nucleons from an inert core containing the rest of the nucleons of the system [43]. Several of the known halo nuclei are two-neutron halo systems called Borromean systems - bound systems of three particles where any two combinations of these particles are unbound. Shown in Figure 2.1 are the Borromean systems in the low mass region of the Segrè chart. These Borromean systems define the approximate location of the neutron drip line since there is generally nothing bound at higher mass in the isotope group.

^{11}Li is the heaviest particle-bound nucleus in the Li family and is at the edge of the neutron dripline because ^{10}Li is neutron unbound as is ^{12}Li. The radius of ^{11}Li was measured by measuring the interaction cross-section of ^{11}Li on Be, C and Al targets at 790 MeV/nucleon [44]. The root mean square (rms) radius can be extracted from the interaction cross section of the lithium isotopes and was found to have a large jump at ^{11}Li. The rms radius of ^{11}Li is measured at 3.14 ± 0.16 fm which is unusually larger than the other isotopes of Li which followed the $R_l \sim A^{1/3}$ relationship as illustrated in Figure 2.2 [44].

^{10}N plays an important role in our theoretical understanding of two-neutron halo in ^{11}Li since it is the mirror of ^{10}Li. A mirror nucleus is the nucleus that results from replacing all neutrons with protons and all protons with neutrons from its original. Nuclear properties of mirror nuclei are very similar and any difference is typically attributed to the Coulomb interaction. Since ^{11}Li is a Borromean system, the structure of ^{10}Li plays a crucial role in the two neutron halo system of ^{11}Li - as it defines the ^{9}Li+n interaction. By studying structure

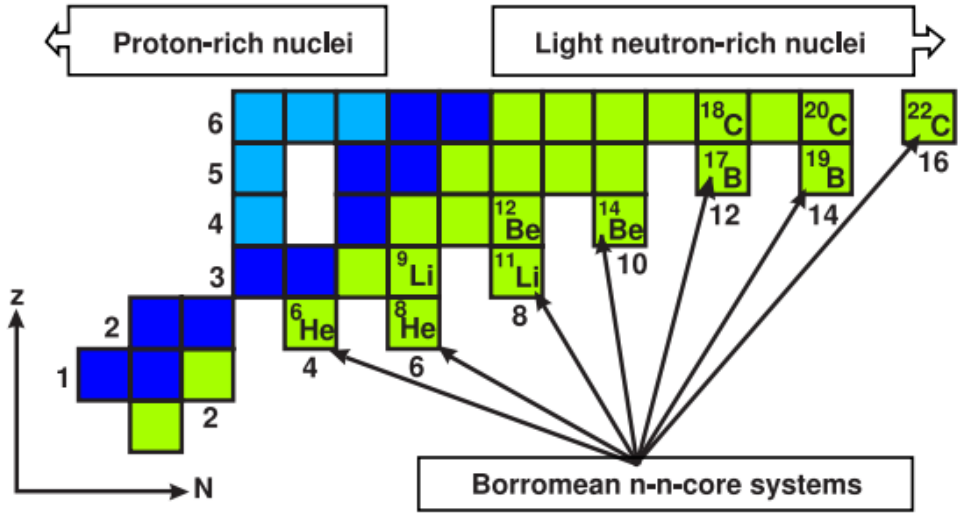

Figure 2.1: Low mass region of the Serge chart highlighting the two neutron halo systems [5]. Reprinted with permission from [5].

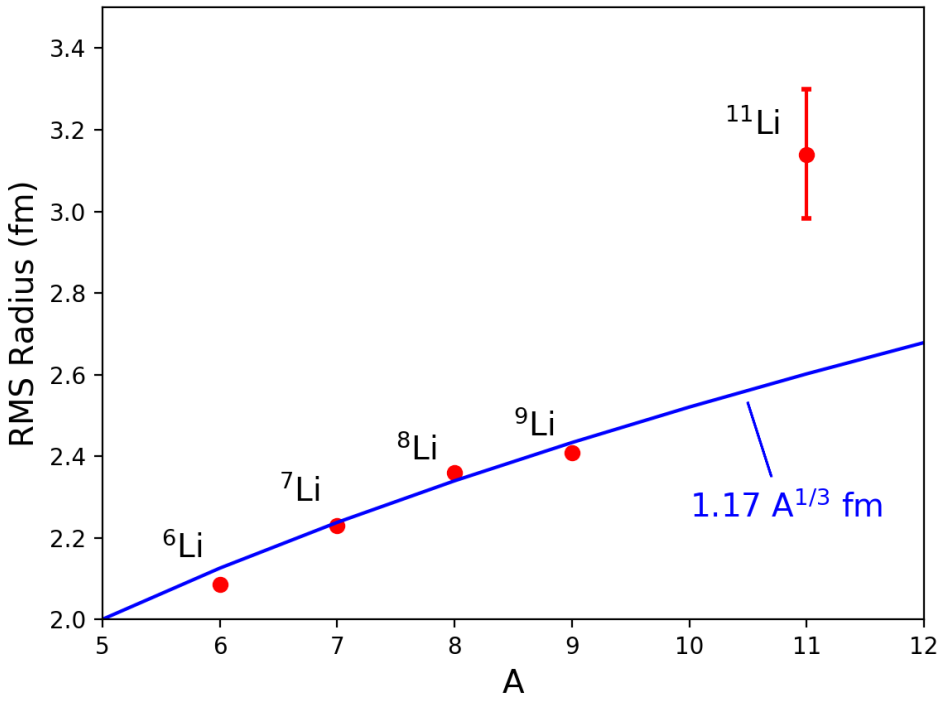

Figure 2.2: RMS radii of the Li isotopes plotted with the normal $R \sim A^{1/3}$ that is found in stable nuclei.

of ^{10}N, we can infer the structure of ^{10}Li and determine the strength of n+^{9}Li interaction.

2.2 Structure of ^{10}Li

^{10}Li is an odd-odd nucleus with three protons and seven neutrons. The ground state spin-parity depends on if the $1p_{3/2}$ proton couples with either a neutron in the $1p_{1/2}$ shell resulting in a ground state of either 1^+ or 2^+ or a neutron in the $2s_{1/2}$ shell making the ground state 1^- or 2^- [45]. The structure of ^{10}Li has been compared to the structure of ^{11}Be because they both contain the same number of neutrons. The ground state of neutron-rich ^{11}Be is $1/2^+$ indicating that the $2s_{1/2}$ shell goes below the $1p_{1/2}$ shell. If the normal shell configuration held for ^{11}Be, the ground state would be $1/2^-$. This same inversion is also seen in the unbound proton rich nucleus ^{11}N [46].

2.2.1 Theoretical Calculations

There have been several theoretical calculations of ^{10}Li using the shell model, a cluster model as well as *ab initio* calculations. Standard shell model calculations of ^{10}Li have been done by Poppelier *et al.* using a $1\hbar\omega$ model space [47]. Their calculations predict the ground state of ^{10}Li to have a spin-parity of $J^\pi = 2^-$.

Varga *et al.* used a microscopic cluster model for ^{11}Li and at the same time the properties of ^{10}Li were calculated [48]. This was done by splitting the core of ^{11}Li, ^{9}Li, into a α+t+n+n cluster for which this type of approach has been successfully used to study the properties of ^{7,8,9}Li [49, 50]. Starting with the ^{9}Li structure or basis, ^{10}Li can be described by coupling the ^{9}Li with a s-wave or p-wave neutron. The level sequence of ^{10}Li was calculated to have a 1^+ ground state at $E = 0.39$ MeV above the neutron threshold followed by a 2^+ state at $E = 0.55$ MeV [48]. Unlike the traditional shell model prediction by Poppelier *et al.*, the ground state of ^{10}Li is calculated to be a p-wave state.

Lastly, NCSM calculations of ^{10}Li were done by Caurier *et al.* using the CD-Bonn potential. Calculations using up to $9\hbar\Omega$ basis space shows that the positive parity states are below the negative parity states [6]. The problem with this specific calculation, shown in

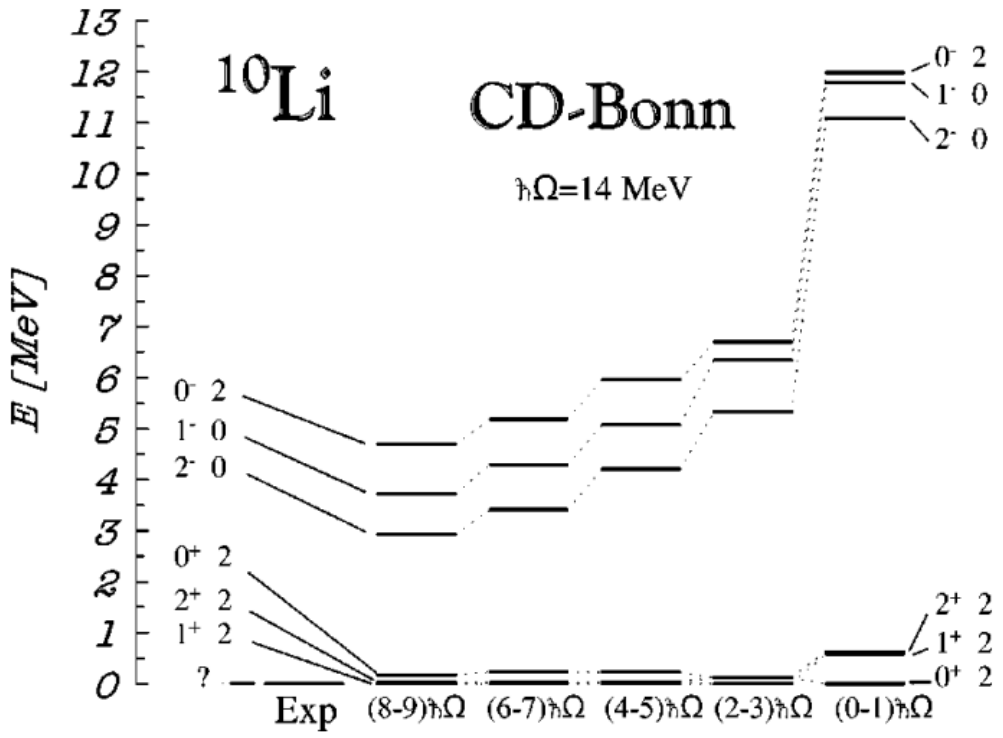

Figure 2.3: Calculations of the excitation energies of ^{10}Li using the NCSM with the CD-Bonn 2000 NN potential.[6]. Reprinted with permission from [6].

Figure 2.3, is that even though the basis space is rather high, it appears that the negative parity states are still not converged and trending down towards the positive parity states. Because of this issue it is difficult to make robust conclusions, but the authors suggest a positive party state as a ground state.

2.2.2 Previous Experimental Results

^{10}Li has been studied experimentally very extensively over the last few decades. This includes ^{11}Li fragmentation [51, 7], d(^{9}Li, p)^{10}Li [52, 8, 9], ^{11}Li(p, d)^{10}Li [10] and various multi-nucleon transfer reactions [53, 54, 55]. Only recent experiments within the last decade will be discussed.

The fragmentation of ^{11}Li was done on a carbon target at 264 MeV/nucleon by Simon *et al.* [7]. One neutron was measured in coincidence with the core of the fragment (^{9}Li in

this case). The distribution of the total relative energy between the charged particle and the neutron (E_{cn}) is found by measuring the relative momentum between the two particles ($\mathbf{p_{cn}}$) and then the energy above the core+n threshold can be calculated by

$$E_{cn} = \frac{m_c + m_n}{2m_c m_n} \mathbf{p_{cn}}^2 \tag{2.1}$$

where m_c and m_n are the mass of the charged particle or fragment and the neutron respectively. The neutron cross section is shown in the top figure of Figure 2.4. The spectrum was fit with a sum of contributions from several resonances using a Breit-Wigner shape. The lowest lying state was treated as a virtual s-wave state and included in the fit by using

$$\frac{d\sigma}{dE_{cn}} \propto p_{cn} \left[\frac{1}{k^2 + p_{cn}^2}\right]^2 \left[cos(\delta) + \frac{k}{p_{cn}} sin(\delta)\right]^2 \tag{2.2}$$

where δ is the s-wave phase shift with a scattering length a and $k \approx \sqrt{2\mu S_n}$ where $S_n = 0.25$ MeV for ^{11}Li [7]. Included in the fit was a virtual s-wave state with a scattering length of $a = -30^{+12}_{-31}$ fm, a p-wave state at resonance energy $E = 0.510 \pm 0.044$ MeV and a width of $\Gamma = 0.54 \pm 0.16$ MeV as well as a d-wave state at $E = 1.486 \pm 0.088$ MeV and a width of $\Gamma < 2.2$ MeV [7]. It appears that ^{10}Li's ground state is a low lying virtual s-wave state.

The bottom panel in Figure 2.4 is the correlation function which is defined as the invariant mass spectrum to a "randomized one". This removes the artificial structure in the invariant mass distributions and does not depend on the shapes of the neutron and charged particle spectra [7]. The quantity $R(E_{cn})$ indicates correlations and two-particle resonances will result in a peak in the correlation function. [7]. This correlation function shows a resonance at low energy and another resonance at 0.5 MeV.

Jeppesen *et al.* studied ^{10}Li via d(^{9}Li,p) reaction at 2.36 MeV/nucleon [8]. The ^{9}Li beam was impinged on a deuterated polyethylene (C_3D_6) target. The reaction products were measured in silicon telescopes covering an angular range from 18° to 80° in the laboratory frame. The extracted excitation function of ^{10}Li for $\theta_{\text{c.m.}} = 98 - 134°$ is shown in Figure

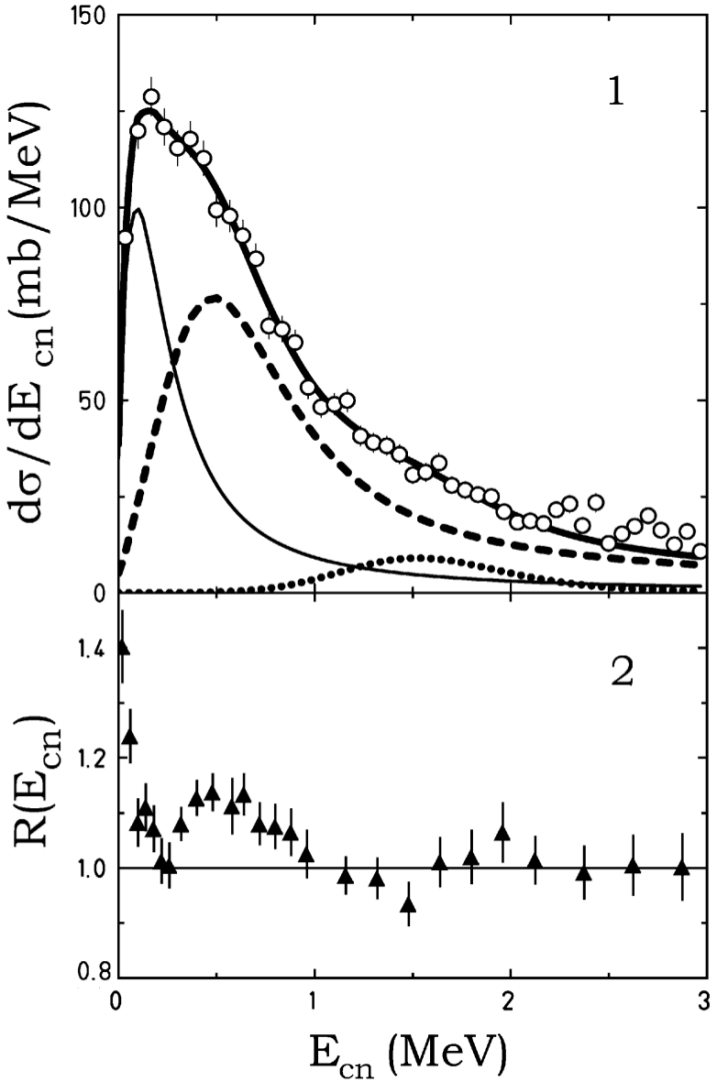

Figure 2.4: Differential cross section as a function of relative energy between the ^{9}Li and neutron. The thin solid curve represents the virtual s-wave state, the dashed curve is the p-wave state and the dotted curve is the d-wave state [7]. Reprinted with permission from [7].

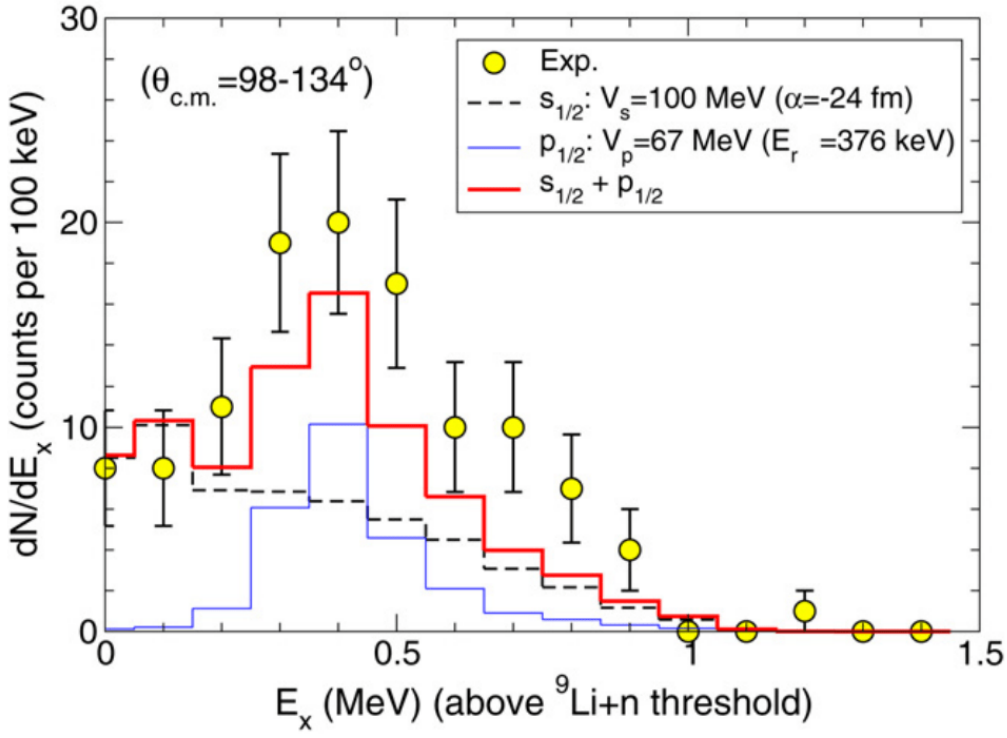

Figure 2.5: Spectrum of ^{10}Li using the d(^{9}Li,p) reaction. A virtual s-wave state was needed to reproduce the data with a p-wave state at $E = 0.38$ MeV [8]. Reprinted with permission from [8].

2.5. Coupled-channel Born Approximation formalism was used to fit the data. To reproduce the experimental data, a virtual s-wave state with a scattering length of $a \sim 13 - 24$ fm corresponding to a resonance energy of $|E| \sim 22$ keV and a p-wave state at $E = 0.38$ MeV above the neutron threshold and a width of $\Gamma = 0.20$ MeV [8]. Similar to the measurement by Simon *et al.*, it appears that the ground state of ^{10}Li is a virtual s-wave state with a p-wave state $\sim 400 - 500$ keV above the neutron threshold.

Cavallaro *et al.* also studied ^{10}Li via the d(^{9}Li,p) reaction at 100 MeV using a CD_2 target [9]. The protons were measured at c.m. angles $\theta_{\text{c.m.}} = 5.5$ to $16.5°$. Figure 2.6 shows the measured excitation function. The statistics in this d(^{9}Li, p) measurement are much higher than the Jeppesen *et al.* measurement. They found no indication of a low-lying s-wave state and the spectrum shows the presence of a p-wave state at $E = 0.45 \pm 0.03$ MeV with a width of $\Gamma = 0.68 \pm 0.03$ MeV [9]. This measurement suggests that ^{10}Li follows the traditional shell

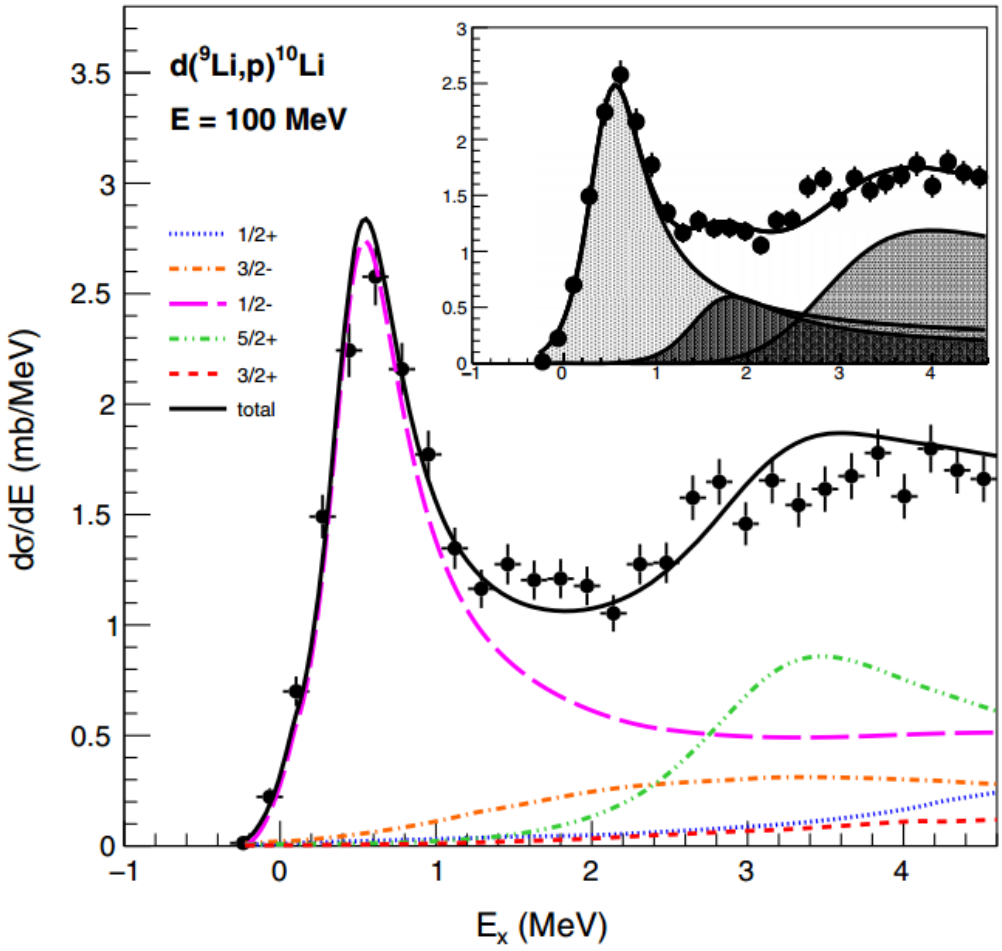

Figure 2.6: Spectrum of ^{10}Li via d(^{9}Li, p) at 100 MeV between c.m. angles $\theta_{\text{c.m.}} = [5.5°, 16.5°]$. The solid black line is the sum of the partial wave contributions from theoretical calculations matching the experimental data [9]. Reprinted with permission from [9].

model configuration and that the ground state is a p-wave state.

^{10}Li has also been measured using the p(^{11}Li, d) reaction. This was done using a 5.7 MeV/nucleon beam on a solid H_2 target [10]. Deuterons were measured between laboratory angles $1.8 - 5.7°$ and the spectrum of ^{10}Li is shown in Figure 2.7 and constructed using the missing mass technique with information from the deuteron energy and angle. Only one resonance was used to fit the measured spectrum at $E = 0.62 \pm 0.04$ MeV and a width of $\Gamma = 0.33 \pm 0.07$. The angular distribution indicates that the neutron is occupying the $p_{1/2}$ shell and similar to the measurement by Cavallaro *et al.*, there is no indication of a low-lying

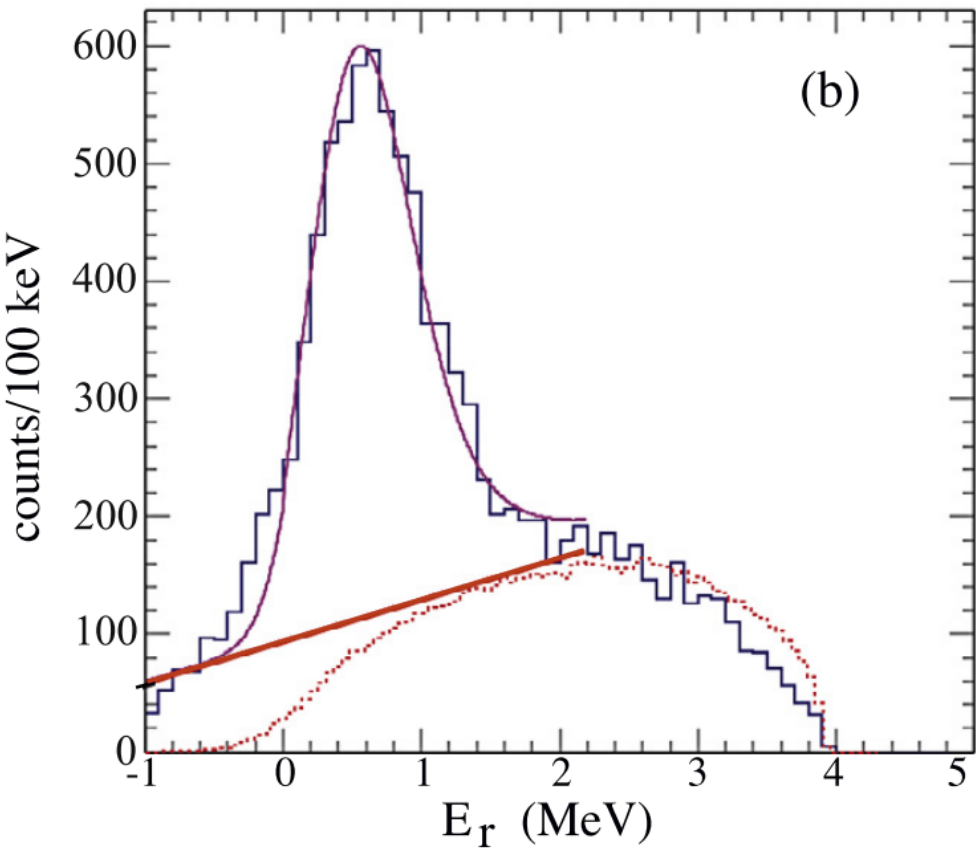

Figure 2.7: Spectrum of ^{10}Li using the p(^{11}Li, d) reaction. A p-wave state at $E = 0.62$ MeV was needed to reproduce the measured data [10]. Reprinted with permission from [10].

s-wave state.

In the last decade including several experiments, the structure of ^{10}Li is still relatively unknown. Some of these experiments have showed evidence of a virtual s-wave state while others do not see any low-lying states. One thing in common is a p-wave state between $E = 400 - 600$ keV above the neutron threshold. We can look toward ^{10}Li's mirror nucleus, ^{10}N, to try to resolve this problem.

2.3 ^{10}Li's Mirror Nucleus: ^{10}N

Aoyama *et al.* has calculated the structure of ^{10}N by using the complex scaling method. This method assumes that ^{10}N is made up of two components: a ^{9}C core and a proton [56]. The ground state of ^{10}N was calculated to have a spin-parity of $J^{\pi} = 2^{-}$ with an energy of

$E = 1.51$ MeV above the proton threshold and a very broad width of $\Gamma = 3.47$ MeV [56]. The excited states with spin-parity 1^+ and 2^+ calculated by Aoyama *et al.* at energies of 2.84 MeV and 3.36 MeV respectively match experimental measurements in ^{10}Li [45]. Although as discussed above, the comparison to experimental measurements is not a valid argument that the calculation works since the structure of ^{10}Li is still not clear.

Experimentally, ^{10}N has only had one study through the four-nucleon transfer reaction ^{10}B(^{14}N, ^{14}B)^{10}N [11]. This experiment was done at GANIL with a ^{14}N beam of 30 MeV/nucleon on a set of four solid ^{10}B enriched targets with a thickness of 0.1 mg/cm^2 each with impurities of ^{11}B, ^{16}O and ^{12}C. ^{14}B was measured using the high-precision magnetic spectrometer SPEG which included measurements for the particles specific energy loss and time of flight to be clearly identified [57]. Separate measurements were also performed with a ^{11}B target, Li_2O target as well as with a C target to measurement the background caused by the impurities in the ^{10}B target. The measured energy spectrum is shown in top part of Figure 2.8 with counts for the ^{10}B target, ^{11}B target and Li_2O target. These background counts are normalized to the impurity content of the ^{10}B target. The bottom of Figure 2.8 shows spectrum of the ^{10}B while subtracting out the normalized spectrum of the background targets.

A broad peak around 373 MeV ejectile energy was observed. This peak was fit with a Breit-Wigner shape on top of calculations for three- and four-body fragmentation reactions: ^{10}B+^{14}N $\rightarrow$ ^{14}B + ^{9}C + p and ^{10}B + ^{14}N $\rightarrow$ ^{14}B + ^{8}B + p + p. The fit is shown in Figure 2.9 including just the fragmentation reactions which matches the background and the Breit-Wigner fit on top of the fragmentation reaction calculations. A broad structure believed to be a $\ell = 0$ state was seen at energy $E = 2.6 \pm 0.4$ MeV with a width of $\Gamma = 2.3 \pm 1.6$ MeV [11]. This resonance suggests that the $2s_{1/2}$ shell is below the $1p_{1/2}$ shell in ^{10}N. This spin-parity assignment has been questioned by Tilley suggesting that these types of multi-nucleon transfer reactions populate $\ell = 1$ states rather than broad $\ell = 0$ states [58].

Unlike the previous measurement on ^{10}N using a multi-nucleon transfer reaction, we can

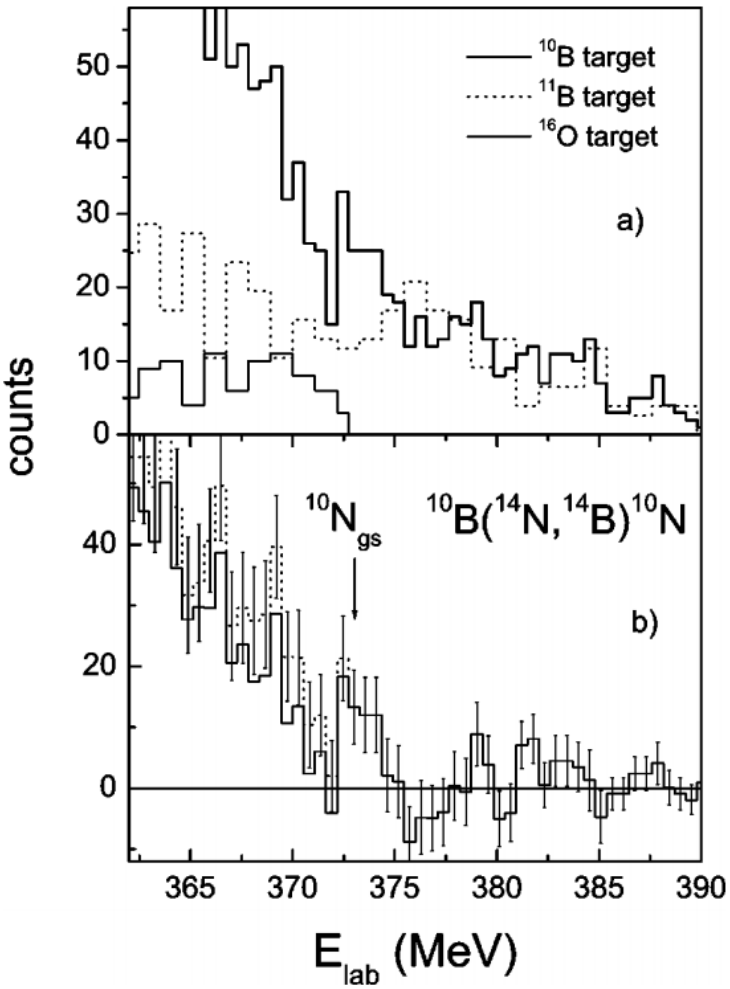

Figure 2.8: (Top) Spectrum from the (^{14}N, ^{14}B) reactions on the ^{10}B, ^{11}B and ^{16}O target. (Bottom) Spectrum after subtracting the counts from the target contaminants [11]. Reprinted with permission from [11].

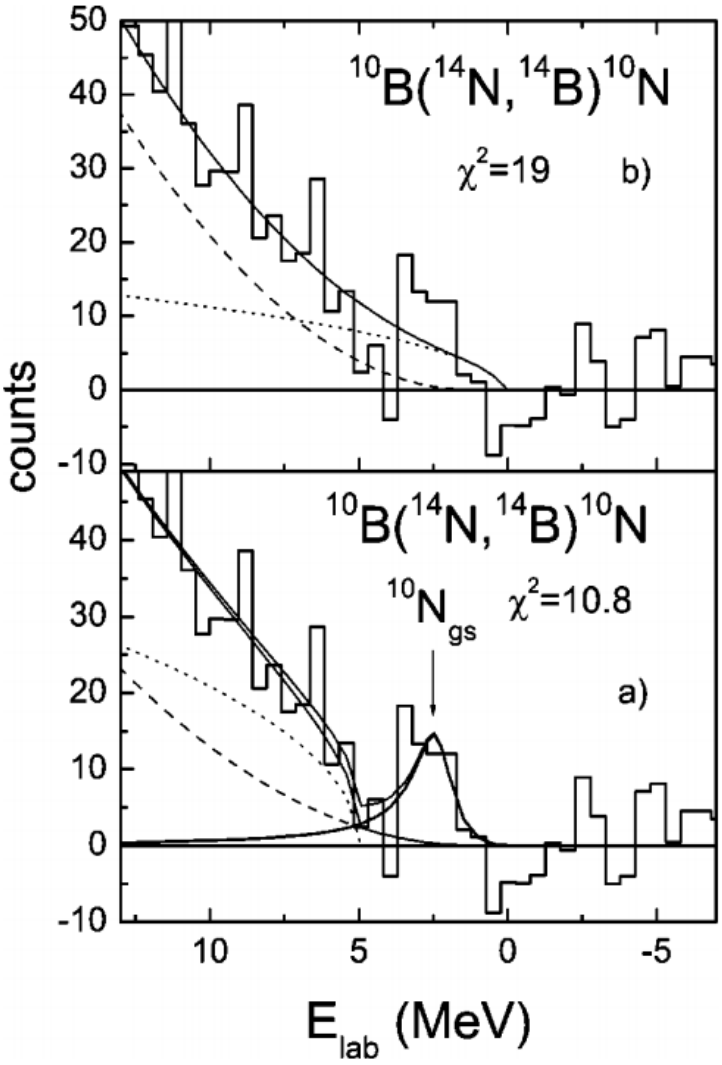

Figure 2.9: (Top) Subtracted background fitting with the sum of three (dotted) and four (dashed) body fragmentation background. (Bottom) Fit of the peak with a Breit-Wigner resonance [11]. Reprinted with permission from [11].

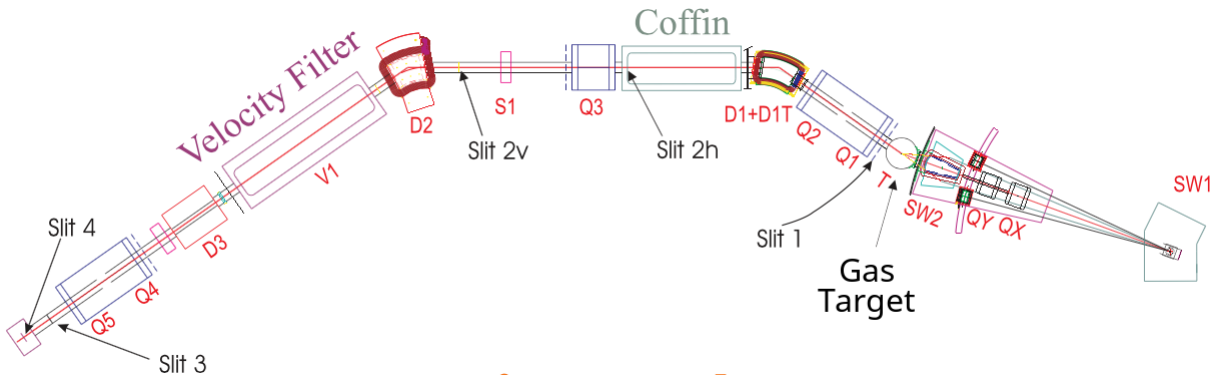

Figure 2.10: Overview of the MARS facility.

use a RIB of ^{9}C to perform resonance proton elastic scattering to study ^{10}N using an active target time projection chamber. Some of the clear advantages to study nuclei using this technique compared to the previous measurement is the much higher cross section and the known reaction mechanisms and tools for analysis.

2.4 Experimental Setup

To measure ^{9}C+p proton elastic scattering, a primary beam of ^{10}B from the K150 cyclotron at the Cyclotron Institute at Texas A&M University was used. The primary beam had an energy of 31 MeV/nucleon with an intensity of 200 pnA. The ^{10}B beam bombarded a hydrogen gas target cooled to liquid nitrogen temperatures to produce the ^{9}C RIB using the ^{10}B(p, 2n) reaction. To separate the ^{9}C beam, the Momentum Achromatic Recoil Separator (MARS) facility was used pictured in Figure 2.10.

2.4.1 The Momentum Achromat Recoil Spectrometer (MARS)

MARS has been utilized extensively to study nuclear reactions with radioactive beams in inverse kinematics [59].

As the primary beam from either the K150 or K500 cyclotron enters the MARS gas cell, the scattering angle can be controlled by two dipole magnets, SW1 and SW2, which are located in front of the gas cell. With these two dipole magnets, the scattering angle can be adjusted from 0° to 30° [59]. The MARS gas cell is cooled to liquid nitrogen temperatures

(77K) and is 9 cm long. The Havar entrance and exit windows have a thickness of 160 μm.

Between the gas cell and the velocity filter, MARS uses the combinations of Q1, Q2, D1, Q3 and D2 to provide parallel transport into the velocity filter. After the D1 dipole and when the scattering angle is close to 0°, the primary beam is separated from the secondary beam and stopped inside of the coffin. Located inside of the coffin is a Faraday cup to measure the primary beam for overall normalization and monitor the beam current. The Faraday cup was used to monitor the primary beam and not for overall normalization during these experiments.

After the D2 dipole magnet, the secondary beam enters the velocity filter or Wien filter. Inside of the Wien filter are perpendicular electric and magnetic fields that can select on the velocity of the charged particle that is desired. When the electric and magnetic forces have equal magnitude, the velocity can be selected by

$$v = \frac{E}{B} \tag{2.3}$$

After the velocity filter, the beam is bent up by the last dipole magnet (D3) and is lastly focused by the quadrupoles Q4 and Q5 before entering the scattering chamber providing the M/q focus where M is the mass of the particle and q is the charge.

Along the MARS beam line are several slits. The slits are used to cut out particles when their position is some distance away from the central ray throughout the beam line. MARS has a mass resolution of $\Delta M/M = 1/300$, an energy acceptance of $\Delta E/E = 9\%$ and a solid angle up to 9 millisteradians [59].

The secondary beam of ^{9}C was created through the (p, 2n) reaction and the reaction had a Q-value of -25.7 MeV. The gas cell was filled with 3 atm of hydrogen gas cooled to 77 K. The average ^{9}C beam intensity was 10^3 pps with the 200 nA of the primary beam ^{10}B. The main contaminant was $^{3}He^{2+}$ because the $^{3}He^{2+}$ ions have the same velocity as the $^{9}C^{6+}$ as well as the same rigidity. The beam purity was $\sim 40\%$ ^{9}C. A detector was placed before the

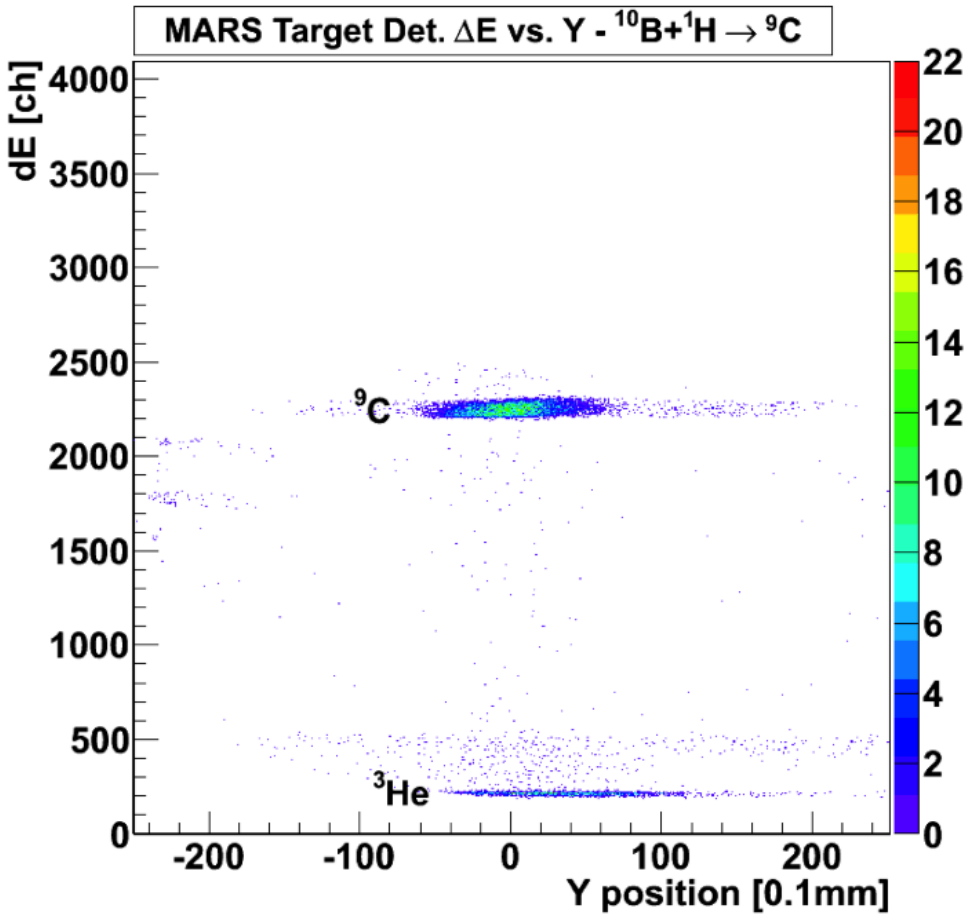

Figure 2.11: Result of the ^{9}C production on MARS showing the main contaminant of ^{3}He and some ^{4}He [12]. Reprinted with permission from [12].

entrance to the scattering chamber to tune the beam on and the ^{9}C and ^{3}He as measured by this detector are shown in Figure 2.11. There is also a small background of ^{4}He that have made their way to the scattering chamber.

2.4.2 Experimental Setup and Procedures

The scattering chamber used for this experiment is shown in Figure 2.12. Since we were interested in the ground and low lying excited states of ^{10}N the ideal beam energy would be below 10 MeV/nucleon and therefore the secondary beam ^{9}C energy of 23.4 ± 0.4 MeV/nucleon from MARS was too high. At energies above 10 MeV/nucleon the background unrelated to elastic scattering, such as breakup, is larger and because the target density must

be increased to stop the high energy beam, the energy resolution becomes worse. The higher target density will effect the lowest measured energy due to the higher specific energy loss. The BC-404 scintillator with a thickness of 700 μm was placed upstream of the scattering chamber at an angle of 45° for an effective thickness of 1 mm. This scintillator reduced the average beam energy from 23 MeV/nucleon to 9.3 MeV/nucleon. Two photomultiplier tubes (PMTs) were used to collect the light signals from the scintillator. This provides particle identification of the beam using the energy deposited in the scintillator and provides a way to filter out of the beam contaminants. The scintillators also provide a fast timing output for time-of-flight measurements to further cut out contaminants.

The chamber is an active target detector meaning that the gas inside is used as a detector medium as well as a target. The scattering chamber was filled with methane gas (CH_4) at 760 torr to stop the beam near the middle of the chamber and allow the light recoils (protons in this case) to make it to the detectors. Windowless ionization chamber was located at the entrance of the chamber. It consists of three plates - anode, cathode, and a Frisch-Grid, and works by measuring the charge of electron-ion pairs created when the charged particles propagate through the gas. The ionization chamber provides additional way to cut out beam contaminants by measuring the specific energy losses and to count the total number of incoming beam ions for overall normalization.

Inside the scattering chamber is a field cage with planar geometry. This created a uniform electric field for the electron drift. Along the beam axis on the bottom of the scattering chamber were an array of eight resistive proportional counters made from carbon fiber. These counters are used to measure the position inside the detector. As the electrons drift toward the wires from the electric field and if the electric field is strong enough, the free electrons drifting can have enough kinetic energy to create another electron-ion pair when colliding with another neutral gas molecule. The threshold field for this effect is on the order of 10^6 V/m [60]. More and more electrons can be created through this process which is known is the Townsend avalanche. For these proportional counter wires, the field is small

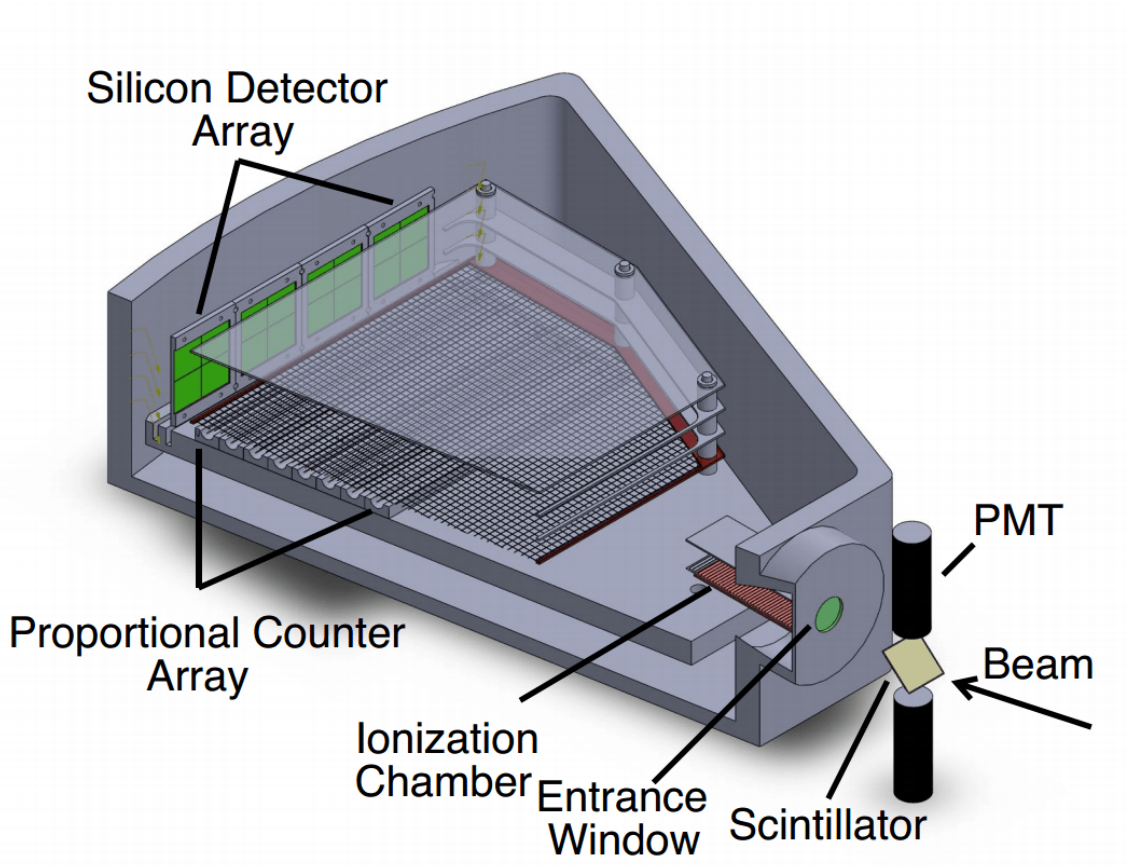

Figure 2.12: Sketch of the scattering chamber. The BC-404 scintillator is placed in front of the scattering chamber and is observed by two PMTs. A Havar window of 4 μm thickness separates the gas volume and the beam line. A windowless ionization chamber is installed at the entrance of the scattering chamber. An array of proportional wire cells and a set of silicon detectors are located downstream in the chamber.

and gets much stronger approaching the wire. The proportional counter cells are read from both sides. As the electrons are collected on the wire, the charge collected on each side of the wire is inversely proportional to the amount of resistance it encountered. We can determine the position ($x_{\mathrm{P.C}}$) at each proportional counter for the charged particle from the charge Q_L (left) and Q_R (right) at each end of the wire by using the formula

$$x_{\mathrm{P.C}} = \frac{Q_R - Q_L}{Q_R + Q_R} a + b \tag{2.4}$$

where a and b are the slope and offset to match to the actual positions inside of the chamber. The position calibration was performed with an alpha source in gas. Covering the Si detectors was a mask with slits in the vertical direction with defined spacing. By measuring the positions measured in the proportional counter cells and the known location of the source, slope and offset for each wire can be found. The measured positions along the proportional counter cells can be used to determine the vertex and the angle of the light recoil since the positions along the beam axis are known. By measuring the time from the proportional counters, we can reconstruct the height of the particles above the cells. Now that we have the horizontal, vertex and z-position of the hits in the proportional counters, full 3D track reconstruction can be performed. We can also measure the total charge measured by the proportional counter cells which is related to the specific energy loss of the charged particle over the cell by summing the energy of both sides

$$E_{\mathrm{P.C.}} = Q_R + Q_L \tag{2.5}$$

The specific energy loss deposited in the cells gives particle identification to select on the species of particle we are measuring (protons in this case).

At the end of the chamber were three MSQ25-1000 MicronSemiconductor silicon (Si) detectors. Si detectors work as a semiconductor diode with two energy bands: the valence band and the conduction band. The valence band corresponds to electrons in the outer-

shell. Electrons in the conduction band are allowed to freely move throughout the crystal. The two bands are separated by the band gap and for Si detectors, this corresponds to 1.1 eV [60]. Adding energy to the system allows the liberation of electrons from the valence band to the conduction band creating holes in the valence band. The energy is proportional to the number of electron-hole pairs. Part of the resolution of a semiconductor detector is limited by the number of electron-hole pairs, n, that are created and thus the standard deviation is $\sqrt{n}$. The electron-hole pairs are measured when a reverse bias voltage is applied. When the bias voltage is applied, there is an equilibrium across the silicon material ensuring that electron-hole pairs are not reabsorbed. This allows for more electron-hole pairs to be measured increasing the resolution. This bias also attracts the electrons and holes to the anode and cathode respectively where the charge can be measured. Each Si detector consisted of four 25 x 25 mm^2 square segments. An outline of each detector is shown in Figure 2.13 for reference. These detectors were used to measure the light recoils. Each of these detectors were 1 mm thick and placed at forward angles with respect to the beam direction.

2.5 Experimental Procedures

The readout scheme for this experiment is shown in Figure 2.14. The ionization chamber signal, proportional counter cell signals and the Si detectors were sent through a preamplifier and then to a MESYTEC MSCF-16 shaper that amplifies and shapes the signal as well as provide triggers if necessary. The energy and time outputs from the shapers were sent to MESYTEC Analog-to-Digital Converters (ADCs) and MESYTEC Time-to-Digital Converters (TDCs) that record an energy and time respectively. The two anodes from the PMTs located upstream from the chamber were fed through a constant fraction discriminator (CFD) and with a threshold high enough to cut out most of the ^{3}He background. The signals were also sent to a CAEN Charge-to-Digital Converter (QDC) to measure the total charge of the signals. The outputs from the CFD were sent to a logic unit to produce a signal when both PMTs fire above the threshold and a signal from the Si detectors was also

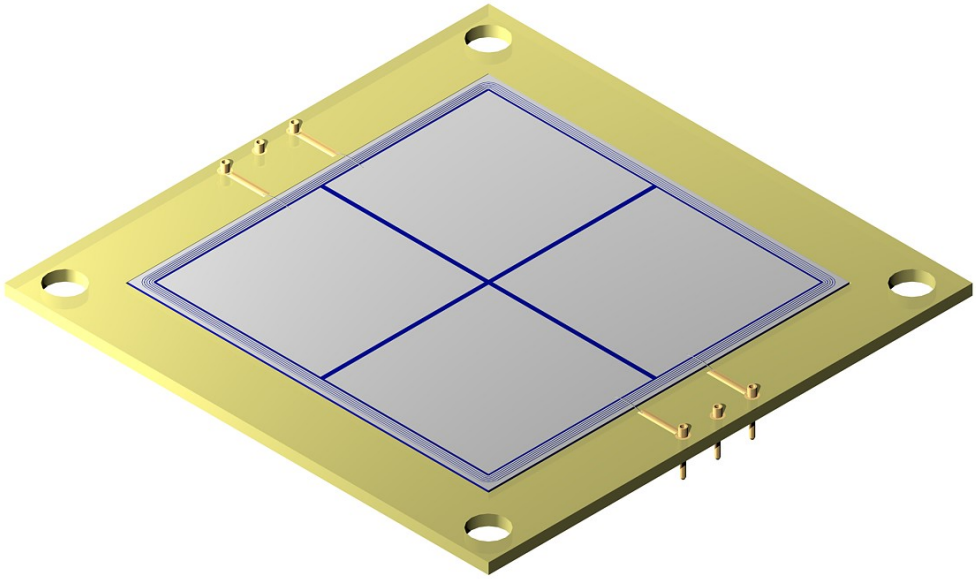

Figure 2.13: Diagram of the MSQ25-1000 silicon detectors.

present. The logic unit also contained a veto signal from the data acquisition system (ACQ computer) indicating that the ACQ was busy and not to trigger. The pulse signal triggered the logic unit was split to a gate and delay generator to generate gates for the ADCs, QDCs and TDCs as well as to the ACQ Computer to record the ADC, QDC and TDC data.

The data was analyzed using ROOT [61]. ROOT is an object-oriented program and library written in C++ that was designed for particle physics data analysis. Other software programs that were used in this analysis include SRIM [62], GEANT4 [63] and an minimization R-matrix software [64].

2.5.1 Calibration of the Detectors

All three silicon detectors were calibrated using a four-peak alpha source on an individual quadrant basis. The alpha source consisted of four different radioactive isotopes: ^{148}Gd, ^{239}Pu, ^{241}Am and ^{244}Cm. The peaks are well known with energies of 3.117, 5.142, 5.474 and

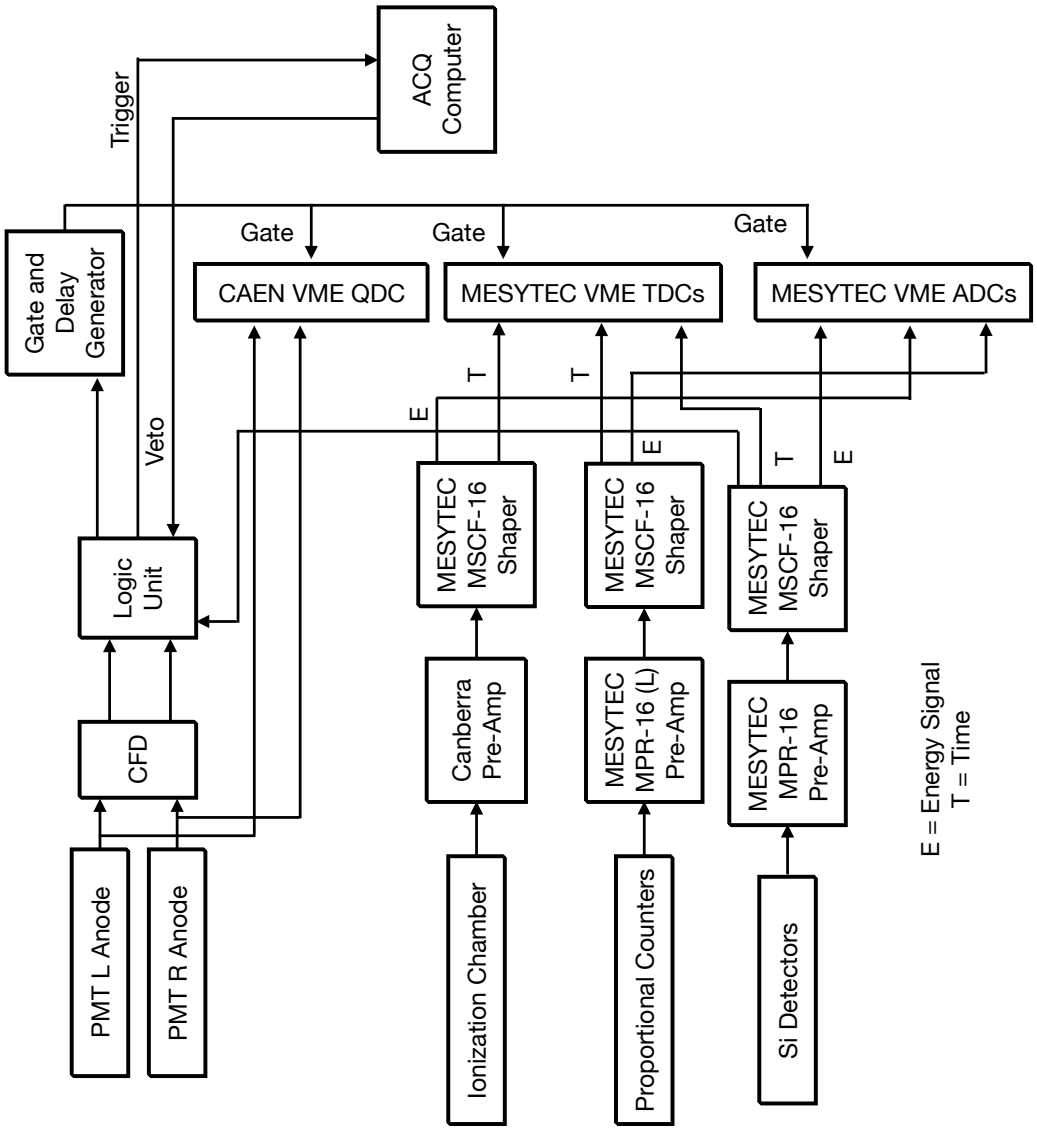

Figure 2.14: Readout scheme of the experimental setup.

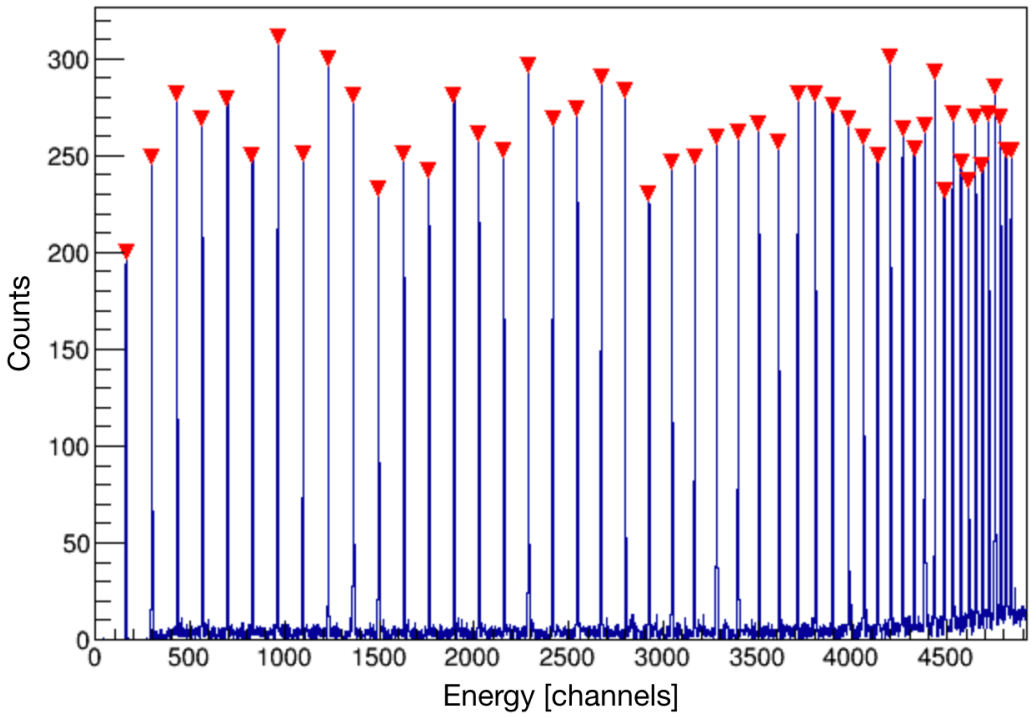

Figure 2.15: Signals measured in a proportional counter cell using equidistantly spaced pulsar signals. The equidistant pulsar signals bunch together at higher channels due to the logarithmic pre-amplifier.

5.787 MeV and the peaks in the Si spectrum were fit with Gaussian functions. The pre-amplifier used for the Si detectors was linear and the calibration from raw channel number to keV was fit using a first order polynomial.

Each of the two side for all eight proportional counter cells were electronically gain matched using a pulser. The pre-amplifier used for the proportional counter cells was logarithmic to provide for a large dynamic range. By measuring the signals in the spectrum using constantly spaced pulser signals, the logarithmic scale could be translated into a linear scale. The centroid for each peak was found and fitted with the known voltage of the pulse as shown in Figure 2.15. Now that the electronics for the proportional counter cell signals have been gain matched, the raw signals for the left and right sides of each proportional counter cell can be used to find the position and summed to measure the specific energy loss of particles passing over the cell.

An alpha source in methane gas was used to test the TPC as well as provide the data to make a calibration for the position of the proportional counter cells. As mentioned in section 2.4.2, the raw position of the proportional counter cell can be found by finding the difference between the beam left and beam right signal for the individual proportional counter and normalizing to the total sum of the both signals in Equation 2.4. This gives bounds for the raw position to be between -1 and 1. For this analysis, it was chosen that a raw position of 1 was the beam right side while a raw position of -1 was the beam left side. Since all of the proportional counter cell signals are now linear, the raw position and real position are linearly correlated by a slope and an offset. Knowing the exact position of the alpha source and the exact positions of where the Si detectors are located, we can use each proportional counter's raw position to made out the position for the three Si detectors. By finding the edge of the detectors in the raw position, we can calibrate the position for each proportional counter cell based on the actual locations of the detectors.

2.5.2 Particle Identification of the Beam

With the use of the BC-404 scintillator upstream from the entrance of the chamber and the windowless ionization chamber placed just inside the entrance, combination of both of these detectors can be used to cut on the beam particles. The two PMTs collecting the light from the scintillator were summed to measured the specific energy loss of the beam ions. The energy loss for charged particles traveling through matter can be described by the Bethe formula. For non-relativistic particles, the energy loss per unit length can be approximated as

$$-\frac{dE}{dx} \propto \frac{z^2}{E}\ln(E/I) \tag{2.6}$$

where E is the energy of the particle, z is the charge of the particle and I is the mean excitation potential [65]. The larger the energy loss, the more energy is deposited in the detectors. What is important in Equation 2.6 is that the higher the charge of the particle, there is more energy loss in a material and the more energy a particle has, the less energy it

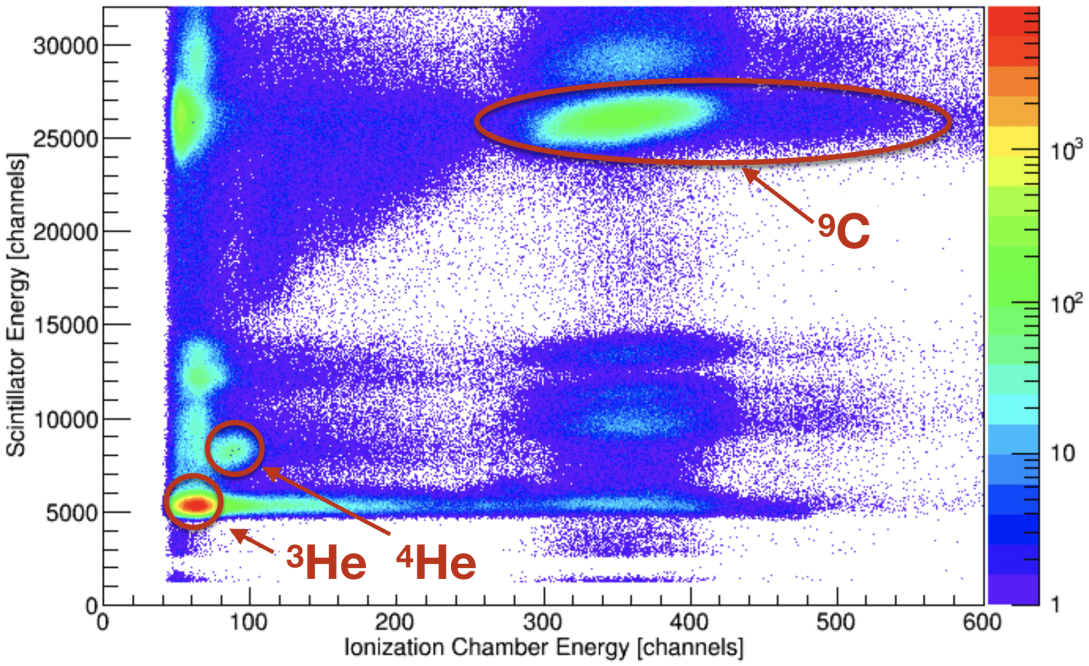

Figure 2.16: Ionization chamber energy vs the scintillator energy. We can clearly defined the ^{3}He, ^{4}He backgrounds and cut on the ^{9}C beam.

deposits in the material. By measuring the energy loss of the beam particles in the scintillator and ionization chamber, the identification of the beam particles can be easily obtained.

Shown in Figure 2.16 is the ionization chamber energy in channels plotted against the sum of the two PMTs energies in channels. There are clear bands in this spectrum associated with different particle species. By using coincidence between the energies of the two detectors, the different beam particles can be clearly identified and are circled in red in Figure 2.16. The lowest mass particle measured in both of these detectors is the $^3He^{2+}$ that comes with the $^9C^{6+}$ beam due to the same charge to mass ratio and these ^{3}He particles have the same velocity as the ^{9}C beam particles. Since the charge of the ^{3}He particles is three times smaller than that of the ^{9}C beam ions, it should lose less energy in the detectors when compared to the ^{9}C particles at the same velocity. Also clear in Figure 2.16 are alpha particles coming with the beam. These were also visible in the tuning of the ^{9}C beam shown in Figure 2.11. With ^{3}He and ^{4}He easily identified, we can cut on the ^{9}C. The cut on ^{9}C beam particles in

Figure 2.16 extends to higher energies in the ionization chamber due to the fact that elastic scattering off of protons can happen in this region of the detector. When this scattering occurs, the ^{9}C particle transfers energy to the proton and has a much higher energy loss over the detector. Since these events happen after the scintillator, the energy deposited in the scintillator should be the same whether or not there was a scattering events over the ionization chamber. So by using the combination of the ionization chamber and the scintillator signals in coincidence, the ^{9}C beam ions entering our chamber can be easily distinguished to look for proton elastic scattering events.

2.5.3 Selecting Proton Scattering Events

Even though there was a cut on the ^{9}C beam particles using the ionization chamber and the scintillator, there is still random coincidence coming mostly from alpha particles. By using the time-of-flight between the Si trigger and the delayed PMT signal, we can gate on events with the correct timing. This is shown in Figure 2.17. This was another way to cut out random coincidence of the measurement.

Since the pressure of methane gas of the system was adjusted so that the ^{9}C beam was stopped right before the beginning of the proportional counter cells, the specific energy loss of the proportional counter cells can be used to select proton events that have hit the silicon detectors. The specific energy loss can be found by summing both sides of the proportional counter cells as in Equation 2.5. By plotting the energy measured in the Si detectors against the energy measured in the proportional counter cells, we can create a specific energy loss (dE) vs energy plot. These kinds of plots are useful for determining particle species. Since the specific energy loss decreases when the particle has higher energy, the dE vs E plots have a very characteristic shape to them. Figure 2.18 depicts the specific energy loss of the proportional counter cells plotted against the measured Si energy. There is a clear band of protons in the spectrum. Also shown in Figure 2.18 is a turn around an energy of 12.5 MeV in the Si. This turn is caused by protons with energies higher than 12.5 MeV. Since the Si is only 1 mm thick, these high energy protons $>$ 12.5 MeV do not stop in the silicon and

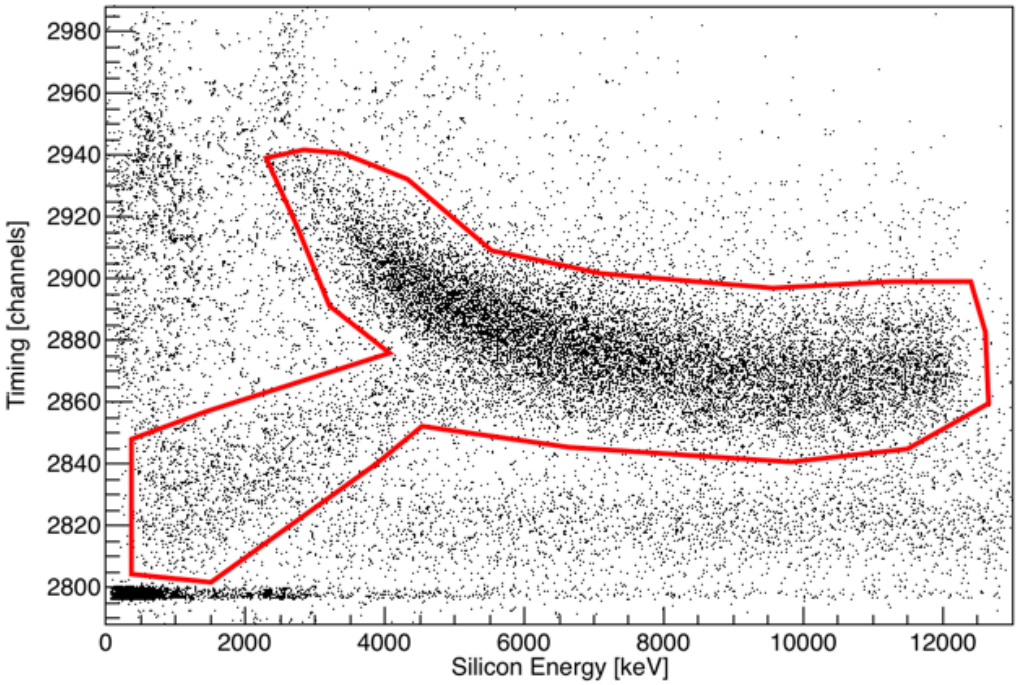

Figure 2.17: Cut made on the timing from the PMTs vs the energy in keV measured in the Si detectors. Punch-through proton events occur in the bottom left of the cut.

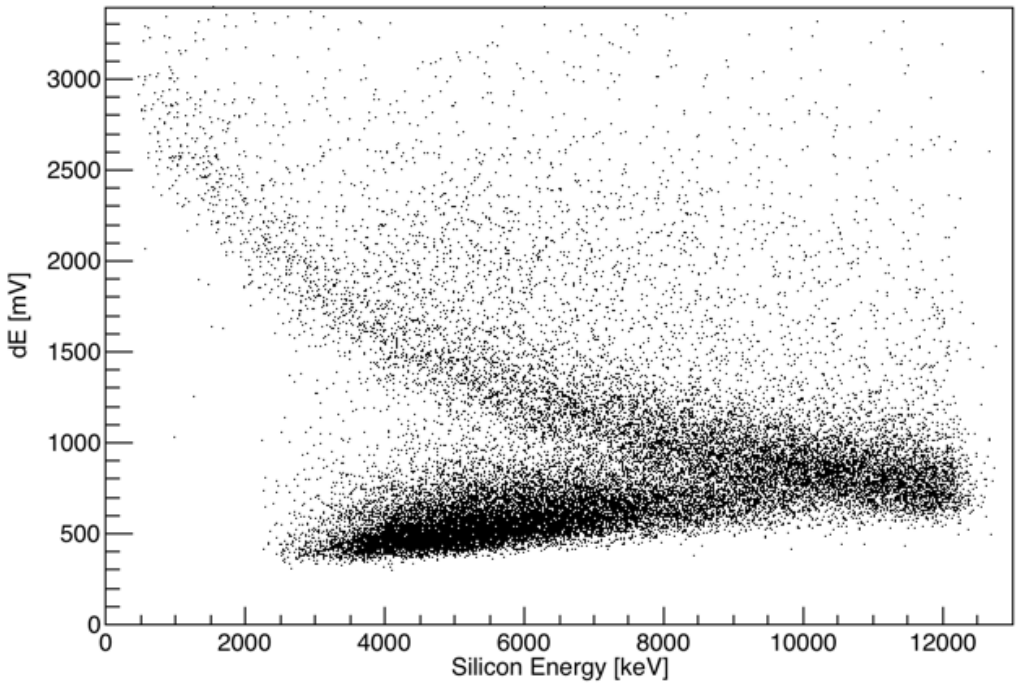

Figure 2.18: Specific energy loss deposited on the proportional counter cells (dE) plotted against the energy measured in the Si detectors.

punch-through the detector. The bottom band in Figure 2.18 corresponds to the punch-through events and events that deposit about 2 MeV in the Si detector actually have the highest total energy. This is because with increasing proton energy less energy is deposited in both the Si detector and the gas.

We can divide the dE vs E spectrum into three regions: a non-punch-through region, a punch-through region and a region where we are not certain whether or not the protons are punching through the detector which will be referred to as the 'mixed' region. The non-punch-through region includes protons with energies up to 8 MeV. For all of these events, the protons are fully stopped in the Si detector and these energies correspond to c.m. energies below 3.2 MeV. The punch-through region includes protons of the lower band from 2 MeV to 8 MeV and corresponds to c.m. energies above 4.5 MeV. The last region is this 'mixed' region with Si energies between 8 to 12.5 MeV in the Si. In this latest region we cannot clearly

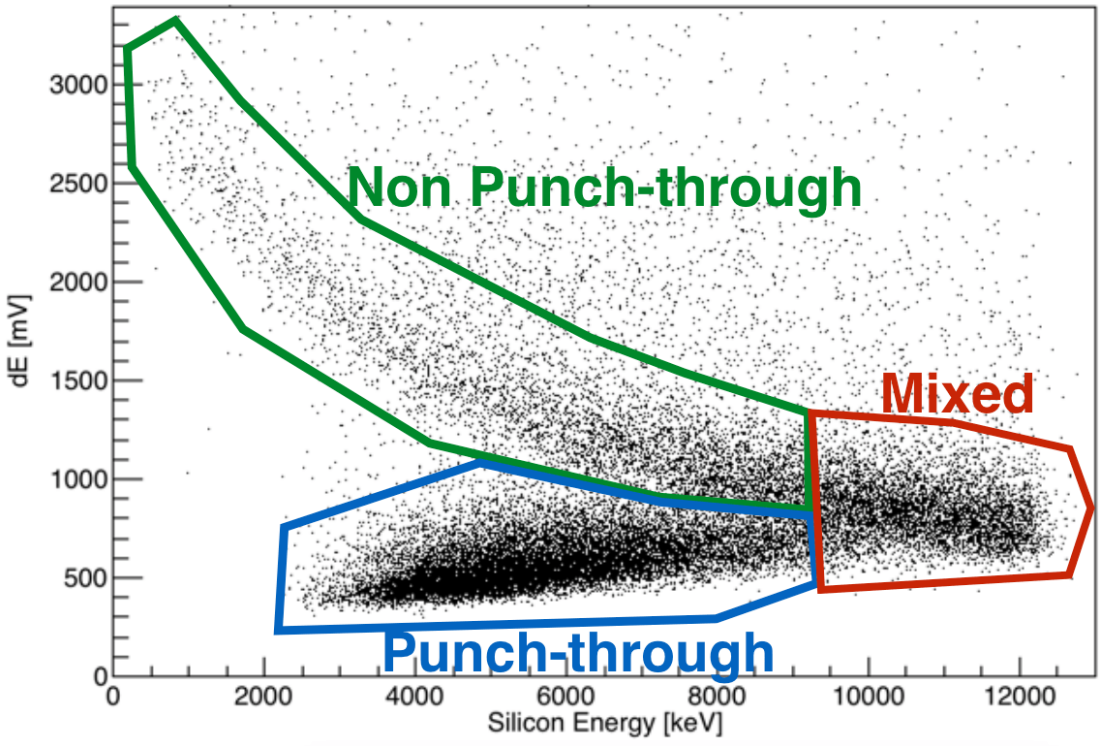

Figure 2.19: The three regions of the dE vs E is shown. The green region is the non-punch-through region where the protons are fully stopped in the Si detector. The blue region are the punch-through events and the red region is the 'mixed' region.

distinguish between punch-through and non-punch-through events. The cuts are presented in Figure 2.19. There are two steps to untangle the mixed and punch-through regions to recover the proton energies. Both of these steps involved the use of Monte Carlo simulations using GEANT4 discussed in the next section [63].

2.5.4 Reconstructing Punch-through Events

Two simulations were made in GEANT4 and are discussed in this section. The first simulation was for the reconstruction of punch-through events while the second simulation was used to realistically recreate the experiment and its conditions.

A very simple simulation was made to be able to reconstruct punch-through events. A beam of protons with various energies above 10 MeV and discrete angles from 0 to 0.7 radians were incident on a Si detector with a thickness of 1 mm. From the simulation,

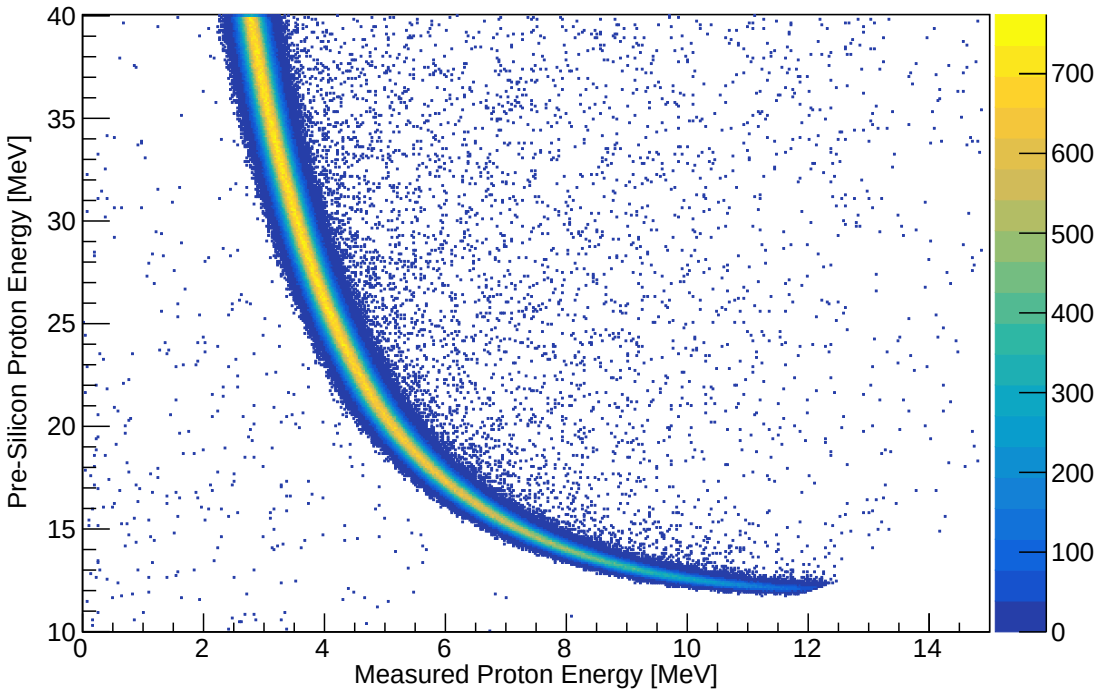

Figure 2.20: The incident proton energy (pre-silicon energy) plotted against the measured proton energy at an incident angle of 0.2 rad.

the incident energy of the protons, the angle of incidence on the detector and the energy deposited in the detector were recorded. For every angle, the incident proton energy (or pre-silicon energy) can be plotted against the measured energy in the Si detectors. One of these plots for an angle of $\theta = 0.2$ rad is shown in Figure 2.20. For every measured proton energy in the Si detector at a given angle, we know the distribution of the incident energy which is Gaussian. So then we can fit this pre-silicon incident energy with a Gaussian to extract a mean of the distribution and the width. This allows us to sample on a Gaussian distribution for punch-through events to obtain the pre-silicon energy of the protons and thus reconstruct the punch-through event's energy. The angle of the proton track that is obtained from the track reconstruction using the proportional counter cells is used as an input for the reconstruction.

After the reconstruction of punch-through events was sorted, another GEANT4 simula-

tion was made to emulate the experimental setup. This includes the realistic beam energy and spread, the scintillator and havar foil at the entrance of the chamber as well as the detectors and correct gas inside. The simulation reproduced the proton elastic scattering and was biased such that the measured cross-section would be flat. This also allowed us to test our reconstruction procedure and sort out the mixed region. In the simulation, we found the number of punch-through events in the mixed region accounts for approximately $20-30\%$ of the total number of events in this region. Using this result, for any event in the mixed region we can decided whether the event is punching through the detector or not by the condition that the boundaries between the non-punch-through and mixed regions as well as the mixed and punch-through regions must have a continuous distribution in the number of counts and not a discontinuity. Unfortunately this approach would wash out any narrow resonances in this region although all resonances in ^{10}N are expected to be fairly broad. Another result obtained from this simulation is that the spectrum above a c.m. energy of $E_{\text{c.m.}} = 5.5$ MeV is unreliable due to the large beam energy spread.

2.5.5 Measured Excitation Function and R-matrix Analysis

With the help of simulations discussed above, we are able to reconstruct the proton energies for all regions. To find the c.m. energy, we must use the combination of the measured Si energy and the track reconstructed using the proportional counter cells. The track of the protons can be traced back to the beam axis to give the angle and vertex of the reaction. We can also get the path length of the proton from the vertex to the Si. Since we know the proton energy at the Si detector and the vertex location in the gas inside the chamber, we can find the energy that the proton losses from the vertex to the Si to recover the proton energy at the vertex location. This is done using stopping power tables calculated using SRIM [62]. The stopping tables give the energy loss dE/dx for a given energy for a gas. We can relate the range a particle traveled in the gas and its specific energy loss using

$$\Delta x = \int_{E_{\text{f}}}^{E_0} \frac{-dx}{dE} dE, \tag{2.7}$$

where E_0 is an initial energy and E_f is a final energy. In our case, we know the range the proton travels and the final energy (the energy at the Si detector) so the initial energy can be found. Once we know the proton energy at the vertex location and know the scattering angle, we can calculate the energy the ^{9}C beam had at the vertex location just before the elastic scattering:

$$E_{\text{beam}} = \frac{(M_{\text{recoil}} + M_{\text{beam}})^2}{4M_{\text{recoil}}M_{\text{beam}}\cos^2\theta}E_{\text{recoil}} \tag{2.8}$$

For every proton elastic scattering event, we can find the energy the ^{9}C beam at the vertex location. Thus, the c.m. energy of the reaction is

$$E_{\text{c.m.}} = E_{\text{beam}}\frac{M_{\text{recoil}}}{M_{\text{recoil}} + M_{\text{beam}}}. \tag{2.9}$$

The cross-section can then be found using Equations 1.8 and 1.9. We divide the three Si detectors into three regions based on the angular range in relation to the beam axis. The first region is the 'Forward Angles' consisting of the zero degree detector. The next two quadrants on either side of the zero degree detector is the 'First Ring' while the most outside quadrants in the Si array are the 'Second Ring'. An illustration is shown in Figure 2.21. We separate all of the events based on which Si quadrant the proton was incident with. Thus we need to calculate the target thickness and solid angle for each region to calculate the excitation function. The target thickness in Eq. 1.8 is found by binning the c.m. energies and finding the total distance the beam can travel from one edge of the bin to the other using Equation 2.7. Thus, the number of target nuclei within this range (or target thickness T_t) is

$$T_t = c\rho\Delta x N_A/M_{\text{methane}} \tag{2.10}$$

where c is the number of target particles in the gas molecule (four in case of CH_4), ρ is the density of the gas, N_A is Avogadro's number and M_{methane} is the molar mass of methane. As we can track the protons and find the vertex location, for a given c.m. energy we can find

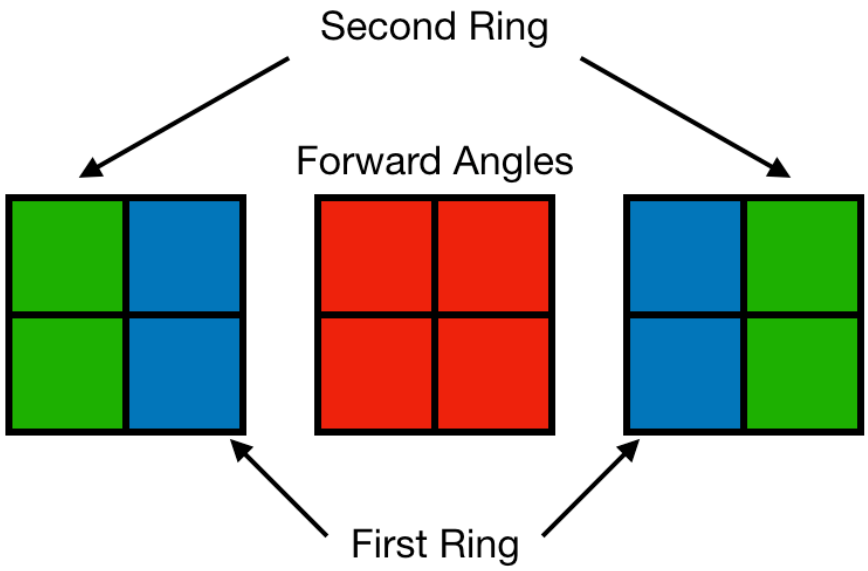

Figure 2.21: Schematic of the three different angular regions for obtaining the excitation function. The 'Forward Angle' region consist of events in the zero degree detector, the 'First Ring' region are the next four quadrants outside of the zero degree detector and the 'Second Ring' are the four most outside Si quadrants.

where in the chamber these reactions came from. Using this location in the chamber and the size of the regions, we can calculate the solid angle.

Due to extended gas target used in these measurements the scattering angle for any particular region in the Si detector is a function of c.m. energy. Events with smaller c.m. energy occur closer to the Si detectors and thus have a larger c.m. angle while higher c.m. energy happen closer to the entrance of the chamber and have a smaller c.m. angle. So with the number of counts for each c.m. energy and the target thickness and solid angle for each bin calculated, we can calculate the cross section and get the excitation function. Due to the shallow angle of tracks in the Forward Region, we limit the excitation function to just events in the non-punch-through region corresponding to a maximum c.m. energy of $E_{\text{c.m.}} = 3.3$ MeV. The First and Second Ring excitation functions are shown up to $E_{\text{c.m.}} = 5.5$ MeV. The c.m. angular range for the Forward Angles, First Ring and Second Ring are then $166° - 170°$, $139° - 162°$ and $129° - 154°$ respectively. The First Ring had the highest quality data and this region was used for R-matrix fitting. This is due to the fact that the angles of proton

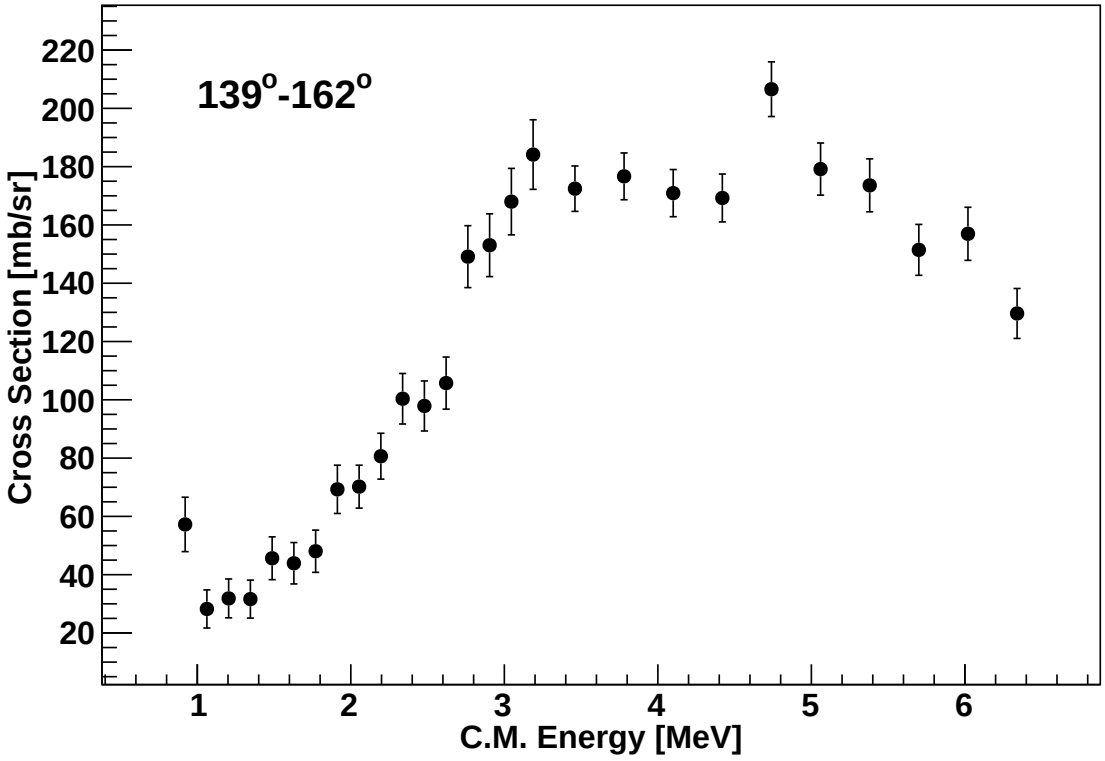

Figure 2.22: Spectrum of protons from the ^{9}C+p resonance scattering for the first ring [13]. Reprinted with permission from [13].

tracks are not as shallow as the Forward Angles and it has more statistics when compared to the Second Ring. The measured excitation function for the First Ring is shown in Figure 2.22 [13].

R-matrix calculations were performed using the code MinRMatrix [64] with a channel radius of $a = 5.0$ fm. Only states with an angular momentum of $\ell = 0$ or $\ell = 1$ were considered in these calculations. The spectrum of the Forward Angles and Second Ring regions had a background of 25 mb/sr each. This background most likely comes from the fusion-evaporation of the ^{9}C beam on the ^{12}C in the methane gas and the breakup of ^{9}C on the methane gas and entrance window. The First Ring did not need any background subtraction due to better tracking to cut out these background reactions. Figure 2.23(b) shows the First

Ring and several R-matrix calculations. The red dash-dotted line is Rutherford scattering which clearly does not reproduce the measured spectrum. As shown, there is a slow rise starting around $E_{\text{c.m.}} = 1.2$ MeV. The magenta dotted line in Figure 2.23(b) is the R-matrix calculation for no resonances in the system but the hard sphere phase shift as described in Equation 1.24. A single $\ell = 0$ resonance with a spin-parity of $J^\pi = 2^-$ was placed at $E_{\text{c.m.}} = 2.2$ MeV and is shown as the red curve in Figure 2.24. This agrees well with the spectrum at energies < 2.2 MeV but does not reproduce the higher cross section at high energies. To reproduce the cross section at higher energy, along with the $J^\pi = 2^-$ state at $E_{\text{c.m.}} = 2.2$ MeV and a width of $\Gamma = 3.1$ MeV, a second $\ell = 0$ state with spin-parity of $J^\pi = 1^-$ was placed at $E_{\text{c.m.}} = 2.8$ MeV and had a width of $\Gamma = 1.2$ MeV. This configuration is shown as the dashed blue line in all of Figure 2.23. The measured cross section can also be reproduced by switching the order of the two $\ell = 0$ states. The green solid line in Figure 2.23 has a $J^\pi = 1^-$ at $E_{\text{c.m.}} = 1.9$ MeV with a width of $\Gamma = 2.5$ MeV while the $J^\pi = 2^-$ state was located at $E_{\text{c.m.}} = 2.8$ MeV and had a width of $\Gamma = 2.0$ MeV. The best fit parameters for the states of these two statistically almost identical solutions are shown in Table 2.1. Also in Table 2.1 are the calculated dimensionless reduced width of the states. Regardless of the specific spin-parity assignment for the two $\ell = 0$ states, the dimensionless reduced with of the ground state is 0.8. Since this is close to unity, it shows that the ground state of ^{10}N has a single-particle nature and can be thought of as a ^{9}C core in its ground state and a proton in π2s1/2 shell. The first excited state has a dimensionless reduced width of 0.4 or 0.25 depending on the specific spin-parity assignment, 2^- or 1^- respectively. Therefore, the first excited state clearly has more complicated structure than the ground state and has significant contributions from configurations other than $\Psi(^9\text{C(g.s.)}) \times \Psi(\pi\text{2s1/2})$.

The ^{10}Li study using the d(^{9}Li,p) reaction by Cavallaro *et al.* observed a $\ell = 1$ state at 0.45 MeV with a width of 0.68 MeV [9]. Potential model calculations put this state at $E_{\text{c.m.}} = 3.3$ MeV in ^{10}N (see next section for more details on potential model calculations). By reproducing the reduced width of the state seen in ^{10}Li, we can add this state into our R-

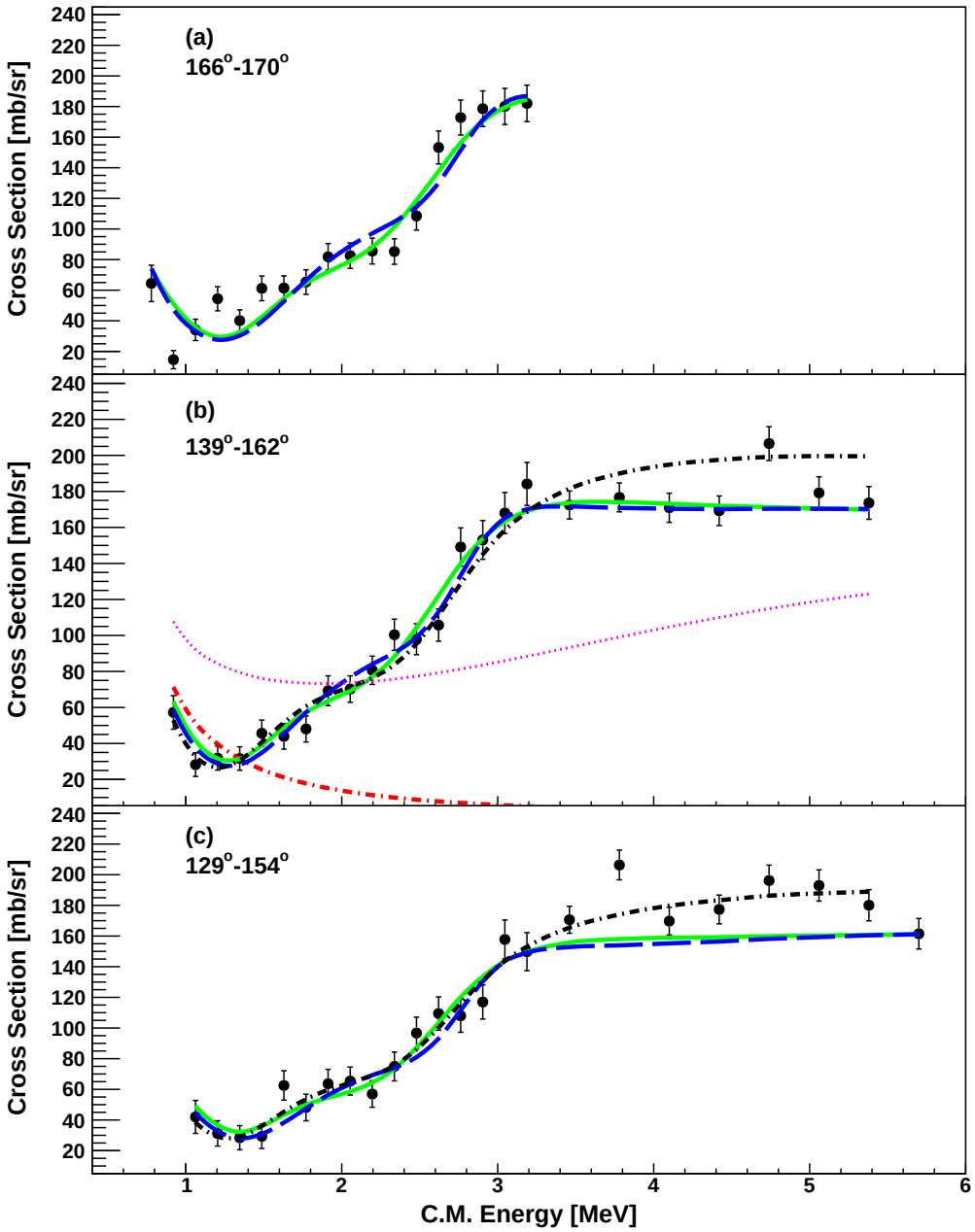

Figure 2.23: Spectrum of protons from the ^{9}C+p resonance scattering at three different angular regions. The red dash-dotted line in (b) is the Rutherford scattering cross section, the blue dashed line is the best fit with $J^\pi = 2^-$ as the ground state and a $J^\pi = 1^-$ state as the 1st excited state. The green solid line is the best fit with a $J^\pi = 1^-$ ground state and a $J^\pi = 2^-$ 1st excited state. The dotted magenta curve is the R-matrix calculation assuming that there are no resonances in the ^{9}C+p system, and that the cross section is defined by the repulsing hard sphere phase shift. The black dash-dotted curve is the fit with a $J^\pi = 2^-$ g.s., a $J^\pi = 1^-$ 1st excited and a $J^\pi = 1^+$ state at 3.3 MeV [13]. Reprinted with permission from [13].

state	J^π	E [MeV]	Γ [MeV]	Θ^2
G.S.	2^-	$2.2^{+0.2}_{-0.2}$	$3.1^{+0.9}_{-0.7}$	$0.8^{+0.2}_{-0.2}$
	1^-	$1.9^{+0.2}_{-0.2}$	$2.5^{+2.0}_{-1.5}$	$0.8^{+0.5}_{-0.3}$
1st excited	1^-	$2.8^{+0.2}_{-0.2}$	$1.2^{+0.6}_{-0.4}$	$0.25^{+0.1}_{-0.1}$
	2^-	$2.8^{+0.2}_{-0.2}$	$2.0^{+0.7}_{-0.5}$	$0.4^{+0.2}_{-0.1}$

Table 2.1: R-Matrix parameters for the best fit of the ground state and first excited state in ^{10}N. For both configurations, the spin-parity assignment, the c.m. energy, the total width of the state, and the dimensionless reduced width are shown.

matrix calculations. The black dash-dotted line in Figure 2.23(b) and (c) display a $J^\pi = 1^+$ state at 3.3 MeV in addition to a $J^\pi = 2^-$ ground state and a $J^\pi = 1^-$ state with the same properties as that reproduce the spectrum without the $J^\pi = 1^+$ state. In the First Ring, this added $J^\pi = 1^+$ state does not reproduce the measure spectrum above $E_{\text{c.m.}} = 3.3$ MeV but in the Second Ring, the measured spectrum in this energy is well reproduced. We cannot claim or rule out any observation of p-wave states in the measured spectrum due to the uncertainties in the reconstruction of punch-through events or any contributions of higher lying states and $\ell > 1$ partial waves.

We can now compare our results to the only previous study of ^{10}N [11] that was made using the ^{10}B(^{14}N, ^{14}B)^{10}N reaction and claiming an observation of the ground state at 2.6 MeV. Their measured state lies exactly between the ground state and first excited state observed in this measurement. It is possible that they observed both or either of these states although the statistics for their measurement were rather poor and spin-parity assignment could not be made.

2.5.6 Location of the 2s-shell in ^{10}Li

Since both $\ell = 0$ states in ^{10}N were observed and dimensionless reduced widths were determined, the location of the $2s_{1/2}$ shell in ^{10}N can now be established by weighted average

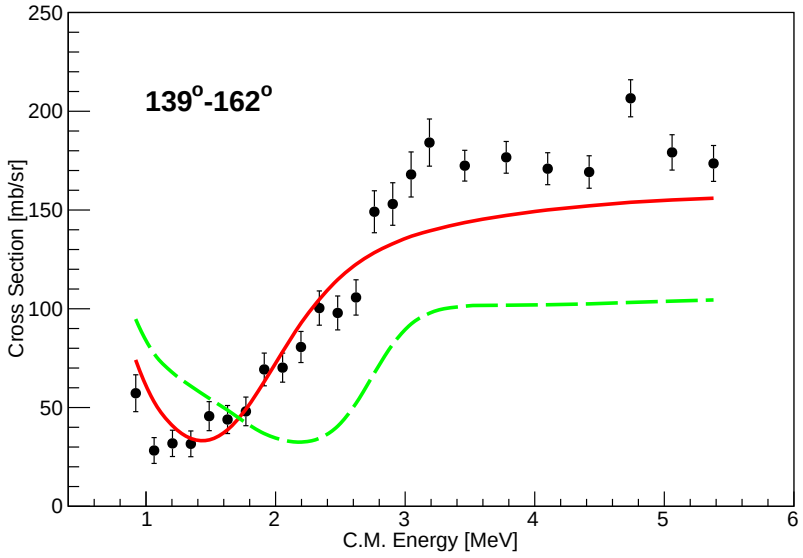

Figure 2.24: Excitation function of the First Ring. R-matrix calculations were performed for a single $J^\pi = 2^-$ state (solid red curve) and a $J^\pi = 1^+$ ground state with a $J^\pi = 1^-$ first excited state (green dashed line) [13]. Reprinted with permission from [13].

between the two s-states - it is unbound by 2.3 ± 0.2 MeV. We can now calculate the location of this shell in the mirror nucleus, ^{10}Li. We use a potential model with a Woods-Saxon potential of the form

$$V(r) = -\frac{V_0}{1 + e^{(r-R)/a}} \tag{2.11}$$

where V_0 is the depth of the potential, $R = r_0 A^{1/3}$ is the radius of the nucleus with A nucleons and a is the diffuseness of the potential. To determine the parameters of the potential, known states in ^{11}N and ^{11}Be were used and these two nuclei are also mirror nuclei. Starting with the three lowest known states in ^{11}Be including the ground state, the $J^\pi = 1/2^+$, $1/2^-$ and $5/2^+$ states, these states were calculated in ^{11}N. To reproduce the known locations of these states in ^{11}N, the parameters of the Woods-Saxon potential are $r_o = 1.25$ fm, $a = 0.7$ fm and the Coulomb radius of $r_c = 1.3$ fm.

With the measured location of the 2s-shell in ^{10}N and using the same potential parameters found between the ^{11}Be/^{11}N pair, the extrapolated location of the 2s-shell in ^{10}Li was

calculated to be −20 keV below the neutron threshold. This of course means that ^{10}Li is bound and we know that it is not. This calculation is of course not exact but we can place the 2s-shell within 100 keV above the neutron threshold. Although not all measurements of ^{10}Li observed a low-lying virtual s-wave state as discussed above, this measurement provides strong evidence towards a low-lying s-wave state in ^{10}Li.

2.6 Conclusion

States in ^{10}N were populated in ^{9}C+p elastic scattering at the Cyclotron Institute at Texas A&M University. A prototype time projection active target detector was used for this measurement. For the first time, the ground state and first excited state in ^{10}N have been observed. Both of these states are $\ell = 0$ states but the specific spin ordering for the ground and first excited state cannot be established. For a $J^\pi = 1^-$ ground state configuration, ^{10}N is unbound by 1.9 MeV while ^{10}N is unbound by 2.2 MeV for the $J^\pi = 2^-$ ground state configuration. The 2s-shell in ^{10}N is located at 2.3 ± 0.2 MeV. Regardless of the specific spin assignments, the ground state is of single particle nature while the first excited state has contributions other than from ^{9}C(g.s.)+p. P-wave states recently observed in ^{10}Li [10] should appear around $E_{\mathrm{c.m.}} = 3.3$ MeV in ^{10}N and while a p-wave state has not been observed in this measurement, it cannot be ruled out either.

3. STRUCTURE OF ^{9}C

3.1 Introduction

^{9}C is the most proton-rich nucleus known to be particle bound other than ^{3}He with a proton to neutron ratio of $Z/N = 2$. The ground state of ^{9}C decays via β decay to ^{9}B and has a half-life of 126.5 ± 0.9 ms. It belongs to the $T = 3/2$ $A = 9$ isobaric quartet along with ^{9}Li, ^{9}Be($T = 3/2$) and ^{9}B($T = 3/2$). There is significant uncertainty regarding spectroscopy of these nuclei. Only two excited states have conclusive spin-parity assignments, and two more excited states have been suggested. The location of the sd-shell is still unknown in these nuclei. The primary goal of the measurements discussed in this thesis was to establish the location of the sd-shell in ^{9}C and to benchmark it against the predictions of contemporary nuclear models. ^{9}C is only bound by 1.3 MeV and all of its excited states are in the continuum. Therefore, ^{8}B+p resonance scattering is a suitable reaction for ^{9}C spectroscopy. Another important goal of this experiment was commissioning of the new experimental apparatus - Texas Active Target (TexAT) - a brief description of which is provided in subsequent sections.

3.2 Previous Studies of ^{9}C

The early studies of ^{9}C were done using multi-nucleon transfer reactions. Multi-nucleon transfer reactions allowed experimentalists to study exotic nuclei before the development of RIB. The ground state of ^{9}C was discovered in 1964 through the three-nucleon pickup reaction ^{12}C(^{3}He, ^{6}He)^{9}C by Cerny *et al.* [14]. A ^{3}He beam of 65 MeV was used for this study. The spectrum at 12 degrees in the lab frame is shown in Figure 3.1. It was determined from this measurement that the mass excess of ^{9}C is 28.95 ± 0.15 MeV and thus ^{9}C is stable with respect to proton emission.

In 1974 Benenson and Kashy used the same multi-nucleon transfer reaction as Cerny *et al.* [15]. A beam of ^{3}He with an energy of 74.1 MeV was used and reaction products were sent into a magnetic spectrograph at an angle of 8° [66]. The ground state and the

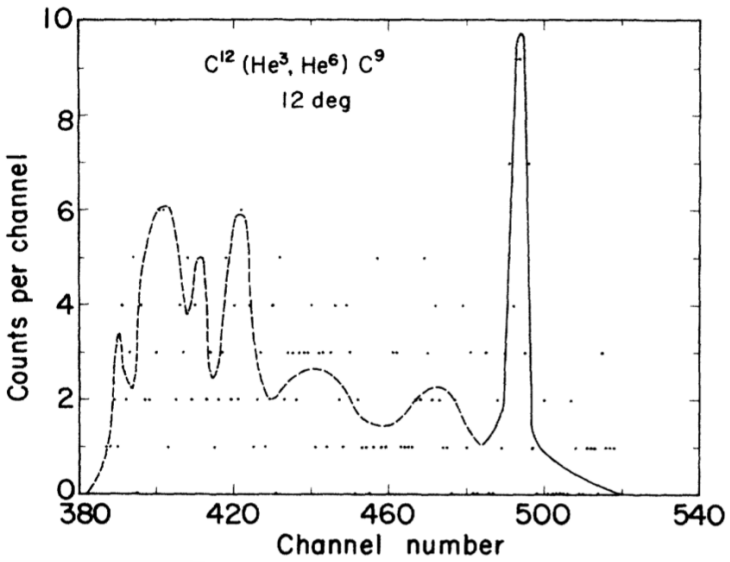

Figure 3.1: Energy spectrum from ^{12}C(^{3}He, ^{6}He)^{9}C. ^{9}C ground state is at channel number 490 [14]. Reprinted with permission from [14].

first excited state of ^{9}C were observed (see Fig. 3.2). The first excited state's energy was measured to be 2.2 ± 0.1 MeV above the ground state. No spin-parity assignment was made for the observed states. The mirror nucleus, ^{9}Li, has a ground state of $J^{\pi} = 3/2^{-}$ and the first excited state of $J^{\pi} = 1/2^{-}$.

Another ^{12}C(^{3}He, ^{6}He)^{9}C reaction study was performed by Golovkov *et al.*. The authors observed the first excited cite at 2.2 ± 0.1 MeV as well as excited states at 3.3 MeV and 4.3 MeV [67]. No experimental spin-parity assignment was made, but indirect arguments were used to infer $J^{\pi} = 5/2^{+}$ spin-parity assignment for the state at 3.3 MeV, implying rather low energy for the sd-shell in ^{9}C.

The excitation function for ^{8}B+p was measured for the first time by Rogachev *et al.* [16]. The secondary ^{8}B beam of 29 MeV was impinged on a 9.0 mg/cm^2 CH_2 target. The Thick Target Inverse Kinematics technique [38, 39] was used and protons were measured using a Si telescope (ΔE and E detectors) at an angle of 7.7° with respect to the beam axis. The excitation function is shown in Figure 3.3 with two features labeled A and B at excitation energies of 2.7 and 4 MeV. The structure at label A or 2.7 MeV does not have a

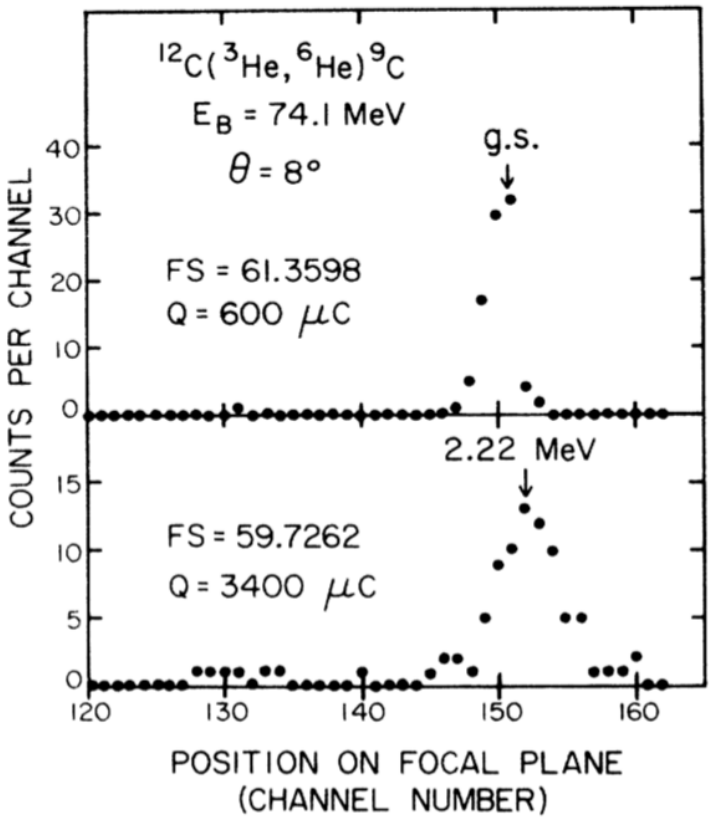

Figure 3.2: Spectra from the ^{12}C(^{3}He, ^{6}He)^{9}C reaction. Top and bottom panels are two different field settings. FS is the field setting of the splitpole spectrometer and Q is the total charge of the beam. Top panel is the ground state and the bottom panel shows the first excited state of ^{9}C at 2.2 ± 0.1 MeV [15]. Reprinted with permission from [15].

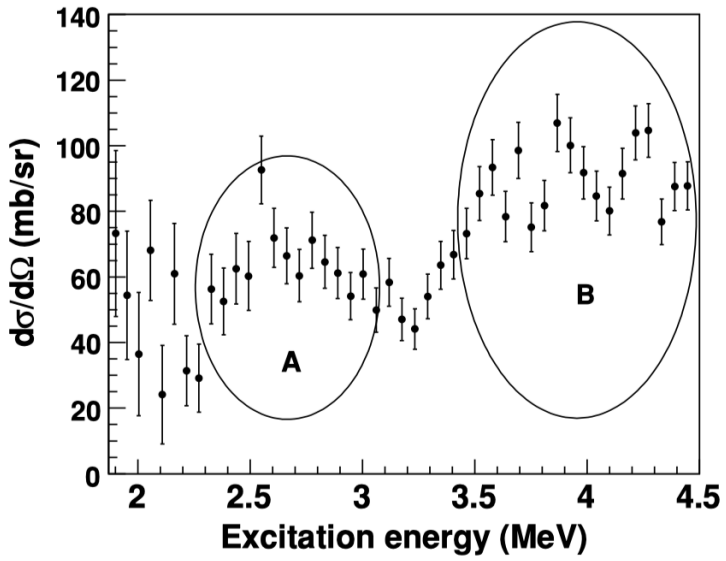

Figure 3.3: Measured raw excitation function of ^{9}C [16]. Peak A corresponds to events not from elastic scattering while B are events from elastic scattering. Reprinted with permission from [16].

counterpart in the mirror nucleus ^{9}Li and is likely not from elastic scattering with ^{8}B. Since this experiment was done with just a solid target and Si telescope, the authors were unable to distinguish between elastic and inelastic scattering. A measurement was also performed with a solid carbon target to remove the background in the CH_2 target spectrum.

A Monte Carlo simulation was performed to simulate the inelastic scattering spectrum via p(^{8}B, p')^{8}B* where the ^{8}B recoil is in the first excited state with a spin-parity of $J^{\pi} = 1^{+}$ and at an energy of 0.77 MeV. This state decays via proton emission. It was found that the inelastic scattering produces two peaks in the spectrum: one from the inelastically scattered proton and another from the proton emitted from the excited ^{8}B ion. An R-matrix analysis was performed on the spectrum after subtracting the carbon target background and the background calculated from the inelastic scattering shown in Figure 3.4. The dotted line in Figure 3.4 shows the R-matrix calculation for which only the known $J^{\pi} = 1/2^{-}$ state located at 2.2 MeV was included. Clearly, this does not agree with the rising cross section at higher excitation energies. The dashed and dotted-dashed curves show the R-matrix calculations

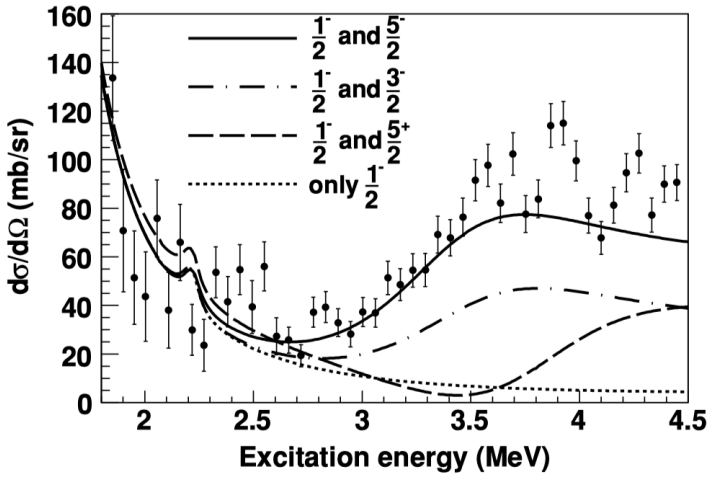

Figure 3.4: Excitation function of ^{9}C subtracting backgrounds. R-matrix calculations are shown and the best fit to the data is the known $J^\pi = 1/2^-$ state plus a $J^\pi = 5/2^-$ state at 3.6 MeV [16]. Reprinted with permission from [16].

for a $J^\pi = 1/2^-$ state at 2.2 MeV with a $J^\pi = 5/2^+$ and $J^\pi = 3/2^-$ state respectively and the cross section is not reproduced at higher energies. It was concluded that the cross section can be reproduced reasonably well if $J^\pi = 5/2^-$ state is introduced at excitation energy around 3.6 ± 0.2 MeV and width of 1.4 ± 0.5 MeV as shown in Figure 3.4 [16].

One problem with the calculated cross section from the $J^\pi = 1/2^-$ and $J^\pi = 5/2^-$ states is that the measured cross section is still higher at energies above 3.8 MeV. Calculations using the Continuum Shell Model (CSM) predict a $J^\pi = 3/2^-$ state close to 4 MeV [16]. The solid line in Figure 3.5 shows the R-matrix cross section for the level scheme of $J^\pi = 1/2^-$, $J^\pi = 5/2^-$ and $J^\pi = 3/2^-$. The $J^\pi = 3/2^-$ state is located at excitation energy $E_x = 4.1$ MeV and has a width of $\Gamma = 1.3$ MeV. The limited energy range and statistics and also significant background did not allow for any firm conclusions regarding excited states above the $5/2^-$

More recently, ^{9}C was studied using inelastic scattering of a ^{9}C beam on a ^{9}Be target by Brown *et al.* [17]. The spectrum of ^{9}C from the detection of protons and ^{8}B events is shown in Figure 3.6. They observe two peaks that correspond to the first and second excited states:

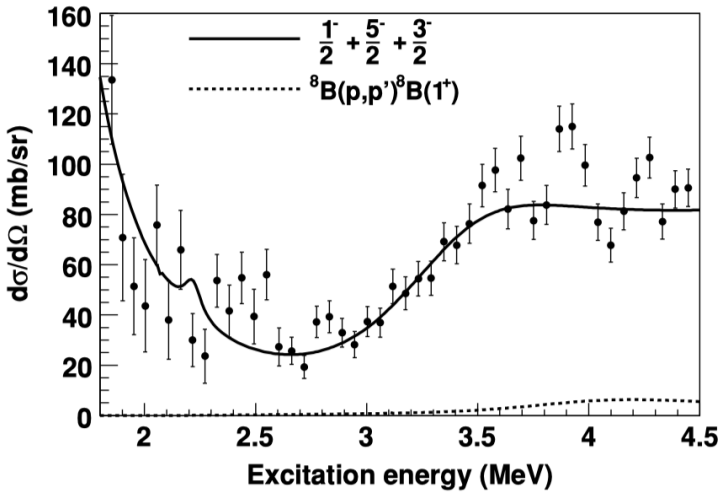

Figure 3.5: Excitation function of ^{9}C with R-matrix fits including $J^\pi = 1/2^-$, $J^\pi = 5/2^-$ and $J^\pi = 3/2^-$ resonances [16]. Reprinted with permission from [16].

$J^\pi = 1/2^-$ and $J^\pi = 5/2^-$ respectively. There is a discrepancy between their measured width of the first excited state and the multi-nucleon transfer reactions which agree with *ab initio* calculations. Brown *et al.* measured a width of $\Gamma = 52 \pm 11$ keV while the multi-nucleon transfer reaction done by Benenson and Kashy measured a width of $\Gamma = 100 \pm 20$ keV which agrees with *ab initio* calculations predicting the width to be $\Gamma = 102 \pm 5$ keV [17, 15, 68]. The spectrum for two proton emission from 2p + ^{7}Be was also obtained. They found two states at 4.40 ± 0.02 MeV and 5.69 ± 0.02 MeV that decay into the excited states. The state at 4.4 MeV agrees with an observed state in the multi-nucleon transfer reaction that is believed to be the start of the sd-shell in ^{9}C [67]. This 4.4 MeV state decays into the $J^\pi = 1^+$ state in ^{8}B and it is argued that the state is most likely a $J^\pi = 1/2^+$ while the 5.7 MeV state decays into the $J^\pi = 3^+$ state in ^{8}B and likely has a high spin of $J \geq 7/2$ [17]. A $J^\pi = 3/2^-$ state tentatively suggested in [16] was not observed by this measurement.

Our goal in this study is to build on the previous measurements and to shed further light on the structure of ^{9}C by measuring the excitation functions for ^{8}B+p resonance scattering to higher energies as well as measuring at several different angles. This also includes looking for the start of the sd-shell in ^{9}C. One advantage we will have when compared to the previous

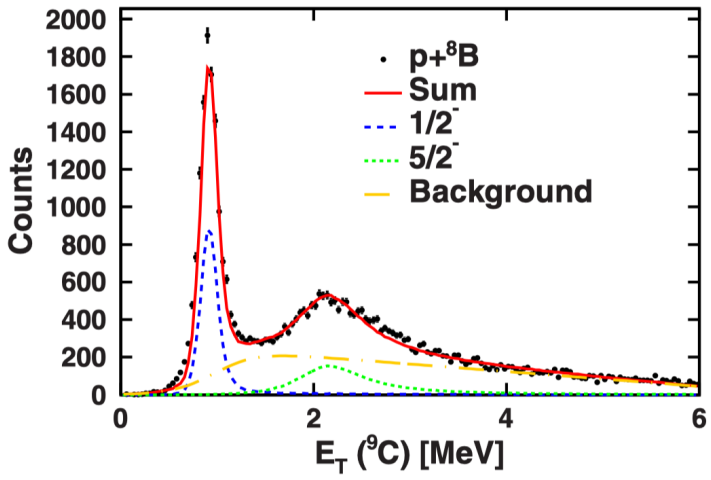

Figure 3.6: Invariant-mass spectrum of ^{9}C. Blue dashed and green dotted line are R-matrix calculations for a $J^{\pi} = 1/2^{-}$ and $J^{\pi} = 5/2^{-}$ respectively [17]. Reprinted with permission from [17].

measurement [16] is the use of active targets that will help remove the background from inelastic scattering seen in previous study.

3.3 Theoretical Calculations

Continuum shell model calculations for ^{9}C were done by Volya and Zelevinsky [18]. This was only done for the p-shell. Besides the states already observed and confirmed, a second $J^{\pi} = 3/2^{-}$ state was predicted to be slightly above the $J^{\pi} = 5/2^{-}$ at $E_{\mathrm{ex}} = 4.1$ MeV. A $J^{\pi} = 7/2^{-}$ was predicted at $E_{\mathrm{ex}} = 6.2$ MeV with a third $J^{\pi} = 3/2^{-}$ at $E_{\mathrm{ex}} = 6.6$ MeV. An overview of the calculation is shown in Figure 3.7.

3.4 Experimental Setup

To study the structure of ^{9}C, we used the MARS facility as described previously in the study of ^{10}N in Section 2.4.1 . A primary beam of ^{6}Li from the cyclotron was directed onto the MARS gas target consisting of ^{3}He and a secondary beam of ^{8}B was created through the two proton transfer reaction (^{3}He, n). The ^{8}B beam had an energy of 7.54 MeV/nucleon with an intensity of 10^{3} pps. What differentiates between the study of ^{9}C and ^{10}N is the experimental apparatus placed at the end of MARS.

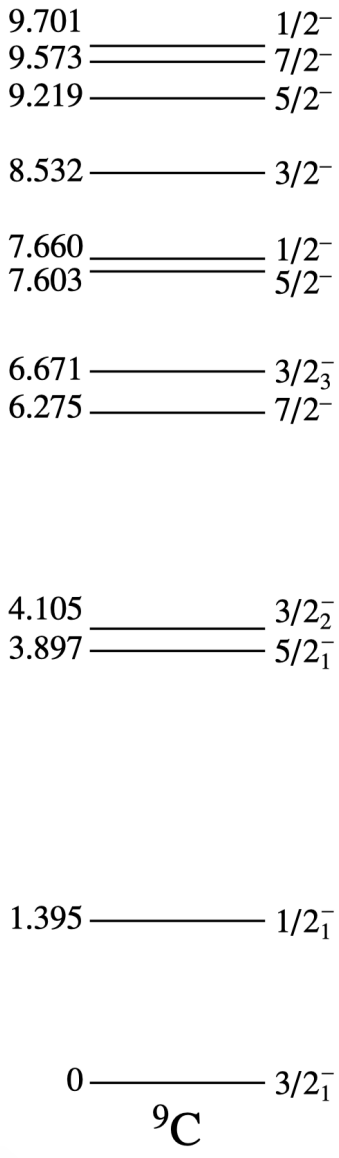

Figure 3.7: Shell model prediction for p-shell states in ^{9}C. Level energies are in MeV [18]. Reprinted with permission from [18].

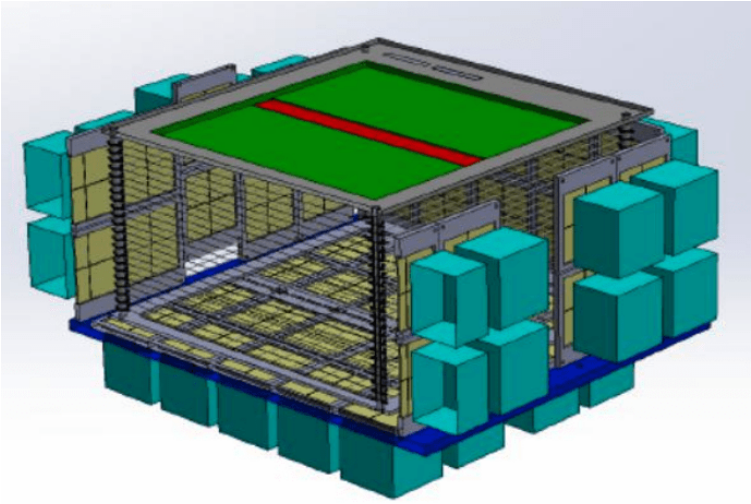

Figure 3.8: Designed TexAT Assembly with one side removed. The top part is the Micromegas where the red portion depicts the central pads and the green are the side regions. The Si detectors (yellow) are each backed by a CsI (turquoise) detector. The beam travels from right to left along the central pads [19]. Reprinted with permission from [19].

3.4.1 The Texas Active Target Detector

This project was a commissioning experiment for the Texas Active Target (TexAT) detector, a 3D view of which is shown in Figure 3.8. The general features of this detector are discussed in this section.

The TexAT detector contains a Micromegas detector or Micro-MEsh Gaseous Structure and it is a gas-electron amplification device [69]. The general design of a Micromegas detector is an anode readout plane below a micromesh. The distance between the readout plane and the micromesh in the TexAT detector is 80 μm and the micromesh is supported by pillars to ensure that the distance is constant. The electric field between the micromesh and the readout plane is much greater than the field above the micromesh. Generally, the field above the micromesh is on the order of 50 V/cm to 1 kV/cm while the field between the micromesh and readout plane can go up to 100 kV/cm. Similar to the proportional counter cells in the ^{10}N experiment, there is an electron amplification close to the readout detector and in this case, between the micromesh and readout plane. For the Micromegas detector, this electron

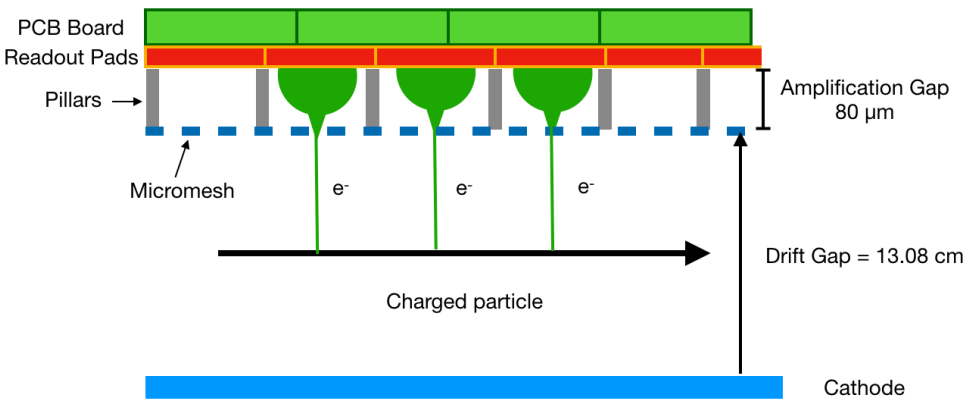

Figure 3.9: Schematic of the Micromegas detector and the sizes are not-to-scale.

gain can go up to 10^5 [69]. A not to scale schematic of the Micromegas detector is show in Figure 3.9.

In the TexAT detector, the Micromegas detector has an active area of 224 mm by 224 mm. There are a total of 1024 readout channels and the detector is divided into three regions: the central area and two sides as shown in Figure 3.10. The central region is 21 mm wide and contains 768 individual readout pads spanning 128 rows along the beam axis with each row containing six columns. Each pad in the central region has a pad size of 3.5 mm wide by 1.75 mm long along the beam axis. Both of the side regions are identical and are 224 mm by 101.5 mm. Instead of using individual pads like the central region, each side region contains 64 strips and 64 chains. The strips are 1.75 mm by 101.5 mm and run perpendicular to the beam axis. There is a gap of 1.75 mm between each strip. Between each strip are pads that are connecting with all other pads in the same column along the beam axis [19]. Although the strips and chains individually cannot provide an accurate location for tracking because each strip and chain run along either the beam axis or perpendicular to the beam axis, they can be matched together to make a 2D point. A picture of the Micromegas readout plane is shown in Figure 3.11.

The full configuration of the TexAT detector will contain 50 quad-segmented Si detectors

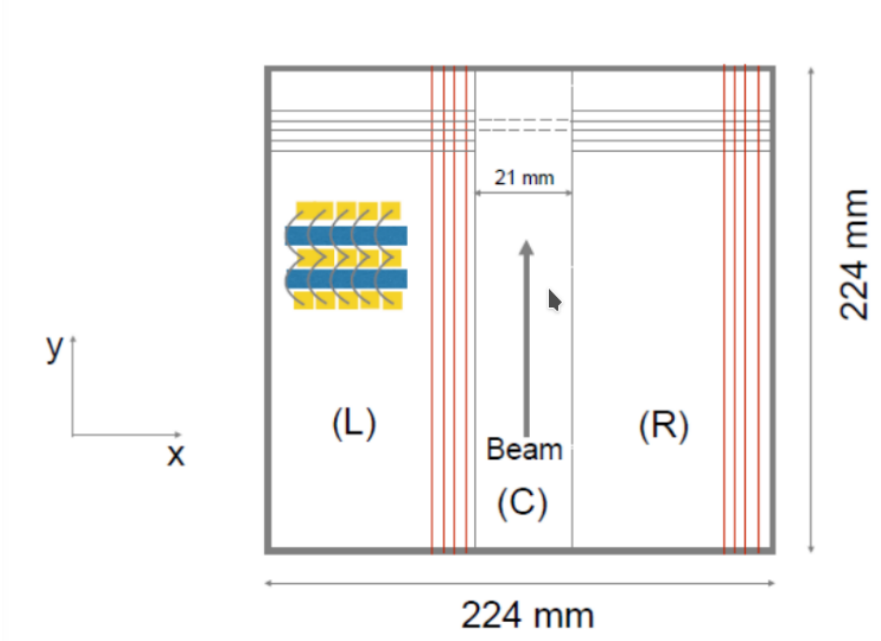

Figure 3.10: TexAT Micromegas Design. The Micromegas consists of three regions: the left, the central and the right [19]. Reprinted with permission from [19].

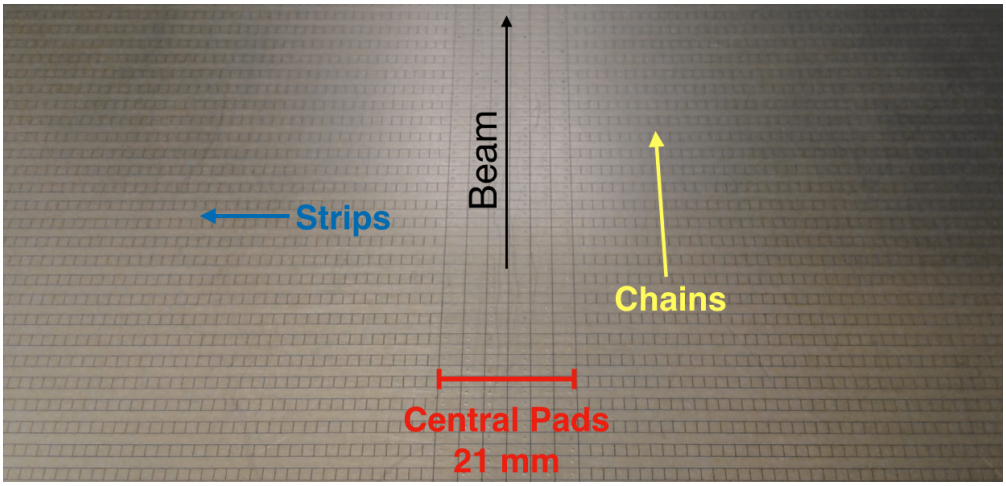

Figure 3.11: Picture of the Micromegas readout plane showing the detection pads. Shows the rows of the central pads consisting of six columns. The strips in the side planes are the solid readout pads that are perpendicular to the beam axis while the chains are the square readout pads in the side regions that go along the beam axis.

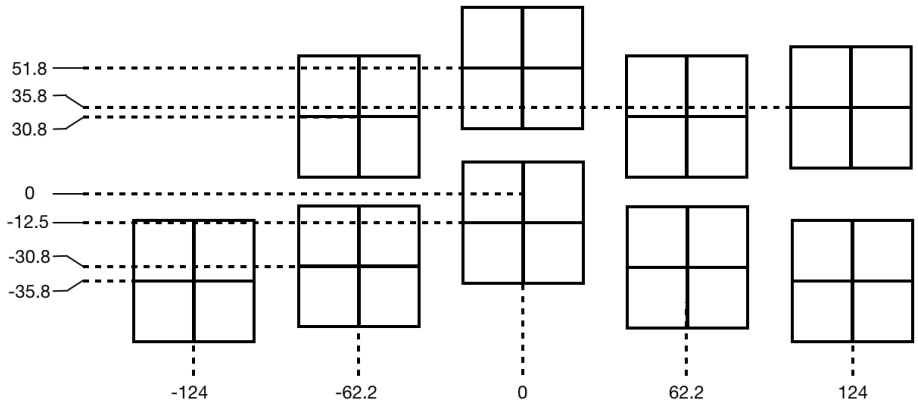

Figure 3.12: Schematic of the Forward Si Array. The center of the chamber along the beam axis is (0, 0) in this diagram. All measured distances are in mm.

each backed by a cesium-iodide (CsI) detector. The detectors will cover a solid angle of 3π. For the commissioning run, only 15 CsI backed Si detectors were used. Nine of these detectors were placed on the forward wall and their configuration is shown in Figure 3.12. This configuration was chosen to place one Si detector at zero degrees relative to the beam axis and to work around the the dimensions of the individual Si detectors. Six detectors were placed on the left wall in relation to the beam direction. Three different thicknesses of the Si detectors were used on the forward wall. The two central detectors had a thickness of 680 μm, the four detectors (two on either side of the central detectors) had a thickness of 750 μm while the three far outside detectors on the forward wall were the MSQ25-1000 MicronSemiconductor Si detectors.

Cesium-iodide (CsI) detectors were located at the back of all of the Si detectors in the TexAT chamber. CsI is a scintillation material that can measure both charged particles and gamma rays. The CsI detectors used in TexAT are doped with thallium, commonly written as CsI(Tl), that are used to shift the wavelength of the light emitted to be better matched with the Si pin-diode photon detectors.

The role of CsI(Tl) in the TexAT chamber are primarily to measure particles that punch-through the Si detectors. In the case of the ^{10}N experiment, protons with an energy $>$ 12

MeV did not deposit all of their energy in the 1 mm thick Si detectors. Because of this, the energy resolution for these events was affected by the reconstruction and the resolution in the excitation function in this energy region was compromised. By placing the CsI behind the Si detectors, we can measure all of the energy for those particles that punched through with good energy resolution. By using an alpha source, we have determined the energy resolution for these CsI detectors to be $< 5\%$. This is much better than the reconstruction method used in the ^{10}N experiment. What is also advantageous is that we know exactly which hits have punched through since the CsI detector has fired instead of relying on the specific energy loss of the dE detectors.

At the entrance of the TexAT chamber is a windowless ionization chamber similar to the one used in the prototype detector for the ^{10}N measurement. This allows for beam particle identification. Upstream from the entrance of the chamber was a thin ~ 100 μm scintillator that was used for overall normalization.

3.4.1.1 General Electronics for TPCs

The final configuration of TexAT will contain 50 quad-segmented Si detectors each backed by a CsI detector in addition to the 1024 channels in the Micromegas for a grand total of 1274 channels. If we used traditional electronics (Pre-Amplifiers, Shapers, ADCs, TDCs, etc.) for this setup, the cost and volume of the electronics would be monumental. Instead, we have used a system developed by an international collaboration for TPCs of up to 30k channels called GET or Generic Electronics System for TPCs [70].

The GET system can be divided into several different modules that all perform different tasks. The first of these modules is called the AGET or **A**SIC for **GET** where and ASIC is an Application Specific Integrated Circuit. The AGET chip amplifies and shapes the signals while preforming pole-zero corrections. For each channel, the signal is stored in 512 time buckets with a frequency that can vary between 1 to 100 MHz. The signals are compared to a threshold to provide a channel level trigger. The signals are then stored in a switch capacitor array in a circular buffer [71]. Each AGET chip has 64 independent channels and

include four extra channels to measure the noise. These "noise" channels are structurally identical to the 64 input channels and provide a way to subtract the electronic noise in the system.

The AsAd (ASIC Support and Analog to Digital conversion) boards each contain four AGET chips. The main role of the AsAd board is to digitize the signals from each AGET chip when a trigger is issued. The digitizer on board the AsAd board is a four channel 12-bit ADC [70]. Up to four AsAd boards can connect to the top level of the GET electronics, the CoBo (**Co**ncentration **Bo**ard). When a trigger is sent to the CoBo board, the CoBo collects the data, time stamps the data and sends the data to be stored. When there is more than one CoBo board, an additional board called the MuTAnt (**Mu**ltiplicity **T**rigger **An**d **T**ime) can synchronize all of the CoBo boards to make sure that the event is stored correctly. The MuTAnt board also collects all of the triggers from all of the CoBo boards and can generate a global trigger. There are three different types of triggers in the GET system: Level 0, Level 1 and Level 2. The Level 0 trigger is an external trigger into the system. A Level 1 trigger is done by summing the multiplicity triggers in the CoBos to generate a global trigger. The last trigger type, Level 2, can trigger on complex predefined pattern of channels that fired.

3.5 Data Analysis

The analysis of the data recorded using the GET DAQ with the TexAT detector involves a multi-step process. It involves subtraction of the baseline for all signals, the waveform fitting to determine waveform maximum amplitude values and peak times, matching chains and strips in the side region to create three-dimensional points for track reconstruction and fitting tracks using various methods for noise reduction.

3.5.1 Baseline Corrections and Obtaining the Energy and Timing

The AGET chips have 64 input channels but provide 68 output channels. Four of these channels are called fixed-pattern noise (FPN) channels that are not connected to any detector and record the intrinsic noise and electronic baseline [71]. These four channels are averaged

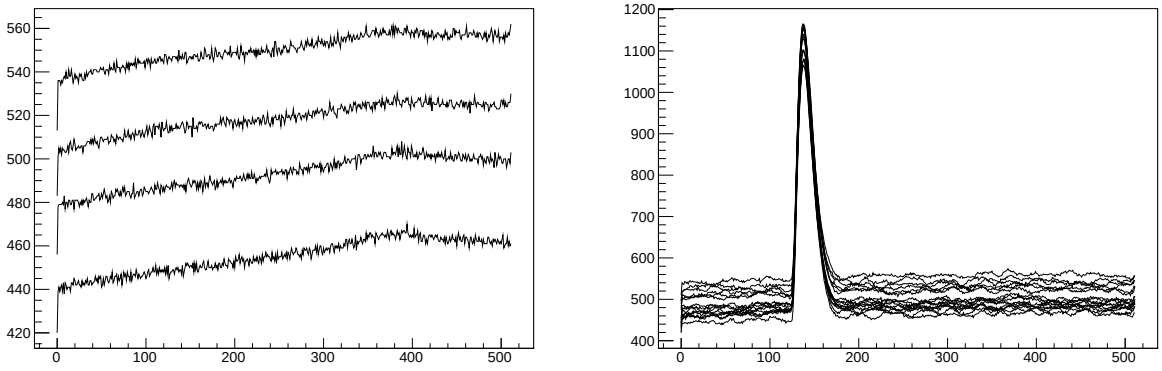

Figure 3.13: (Left) Example waveforms of the four FPN channels. (Right) Raw Waveforms without any FPN or background subtraction.

together and subtracted from each waveform of the remaining 64 channels to remove the intrinsic noise in the electronics. An example of the FPN channels and raw waveforms are shown in Figure 3.13.

To further correct the baseline, the first 10 and last 10 buckets in the waveform were used to find the average of the overall baseline and subtracted it from the signal. The energy and time for each of the waveforms are found by locating the maximum and location of the maximum converted to time (in ns) respectively. An example of the same waveforms corrected by FPN subtraction and background subtraction shown in Figure 3.13 (right) are shown in Figure 3.14.

3.5.2 Chain and Strip Matching

To perform track reconstruction in the side regions of the Micromegas detector, chains and strips must be matched with each other since chains run parallel to the beam axis along the entire Micromegas while the strips run perpendicular to the beam axis along the entire side region. Chains and strips were matched using the time recorded for each channel. When the proton travels over the side region, any chains and strips that correspond to the proton track position should have the same drift time. When the proton track is not parallel to the Micromegas plane, the matched chains and strips based on the same time should form a

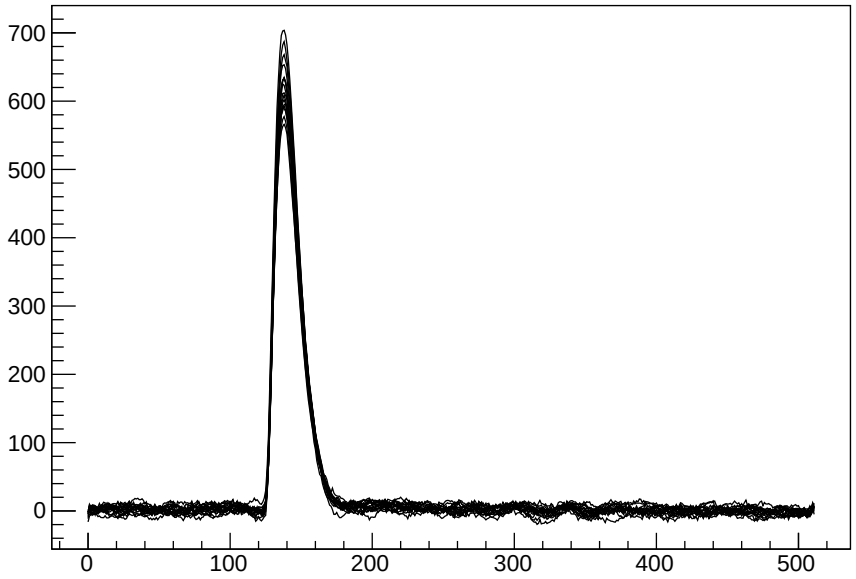

Figure 3.14: Waveforms corrected with FPN and background subtraction.

well defined track and an example is shown in Figure 3.15. When the track is parallel to the Micromegas detector, the timing for the chains and strips will be the same and instead of a defined track like that in Figure 3.15, it forms a rectangle of matched chains and strips. For cases like this, the first point in the matched rectangle closest to the origin and the point furthest away from the origin are chosen to form the track.

3.5.3 Track Reconstruction - Hough Transform

In the side region, the matched pads between the chains and strips will naturally contain some noise that can potentially throw off a fitting procedure. To reduce the effect the noise has on fitting, the two dimensional Hough transform was used.

The Hough transform is a feature extraction technique that has been very successful in image analysis and image processing [72]. The Hough transform was originally used to identify lines in an image and in this analysis, to find tracks (lines) through data points. This method works by transforming points into a parameter space and a voting procedure

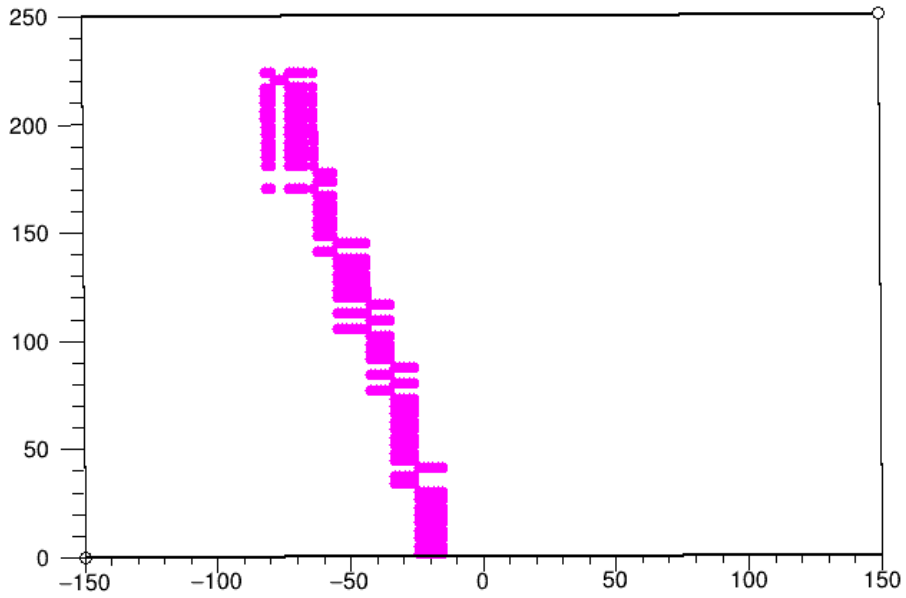

Figure 3.15: An example of matched chains and strips for a single event that can then be used to reconstruct a track.

is used to find peaks in this parameter space. For each point (x, y) in the track, the Hesse normal form is calculated

$$d = x \cos\theta + y \sin\theta \tag{3.1}$$

where d is the distance of closest approach to the origin and θ is the angle between the x-axis and the line connecting the origin to the closest point as shown in Figure 3.16. The (d, θ) parameter space is called the Hough space. For every point in the data, θ is varied from 0 to π and d is calculated.

The algorithm used to find the optimal (d, θ) was to search through all angles and find the lowest standard deviation in d. A simple example with noise is shown in Figure 3.17. In the top of Figure 3.17, there is a straight line formed by the blue colored points while the orange colored points are noise. The Hough space is shown at the bottom of Figure 3.17 illustrating the point where the standard deviation is minimal. By finding the optimal

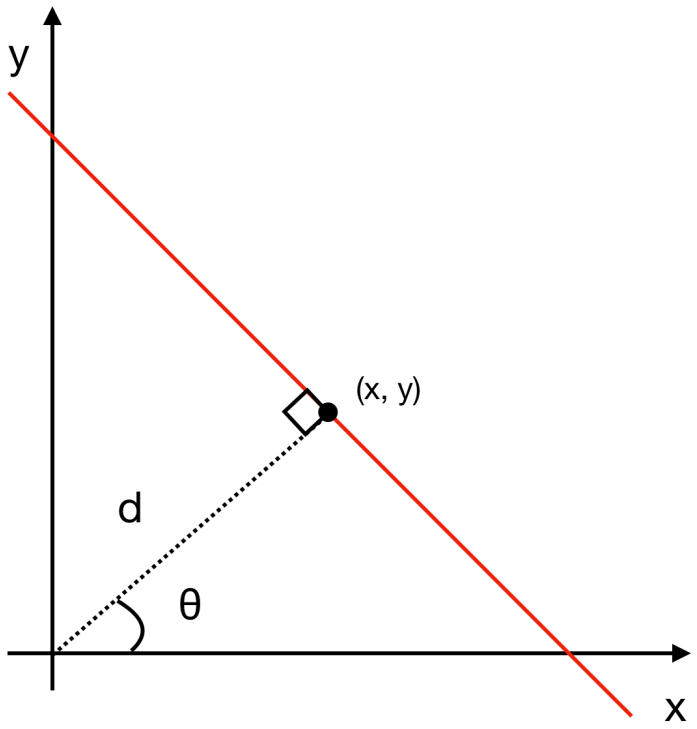

Figure 3.16: Diagram of the d, θ parameters in two dimensions.

parameters (d, θ), we find the best fit of the data that is not affected by noise.

3.5.4 Alpha Source Test in Gas

Now that we are able to match chains and strips and we have developed a technique to fit tracks with noise using the Hough transform, we can test track reconstruction using an alpha source in gas. The gas chosen for this measurement was methane at 50 torr so that the alpha particles do not stop in the middle of the chamber and make it to the Si detector while also depositing enough energy in the gas to make tracks. The alpha source was placed approximately 60 mm behind the Micromegas plate facing the Si detectors. An accumulation of the tracks in the XY-plane are shown in Figure 3.18. Zero on the y-axis in Figure 3.18 corresponds to the start of the Micromegas plate and shown are all the tracks that end up in the forward and side wall Si detectors. The tracks are converging at the (0 mm, -60 mm) point that has about the size of the source ($\sim$ 5 mm along the x-axis).

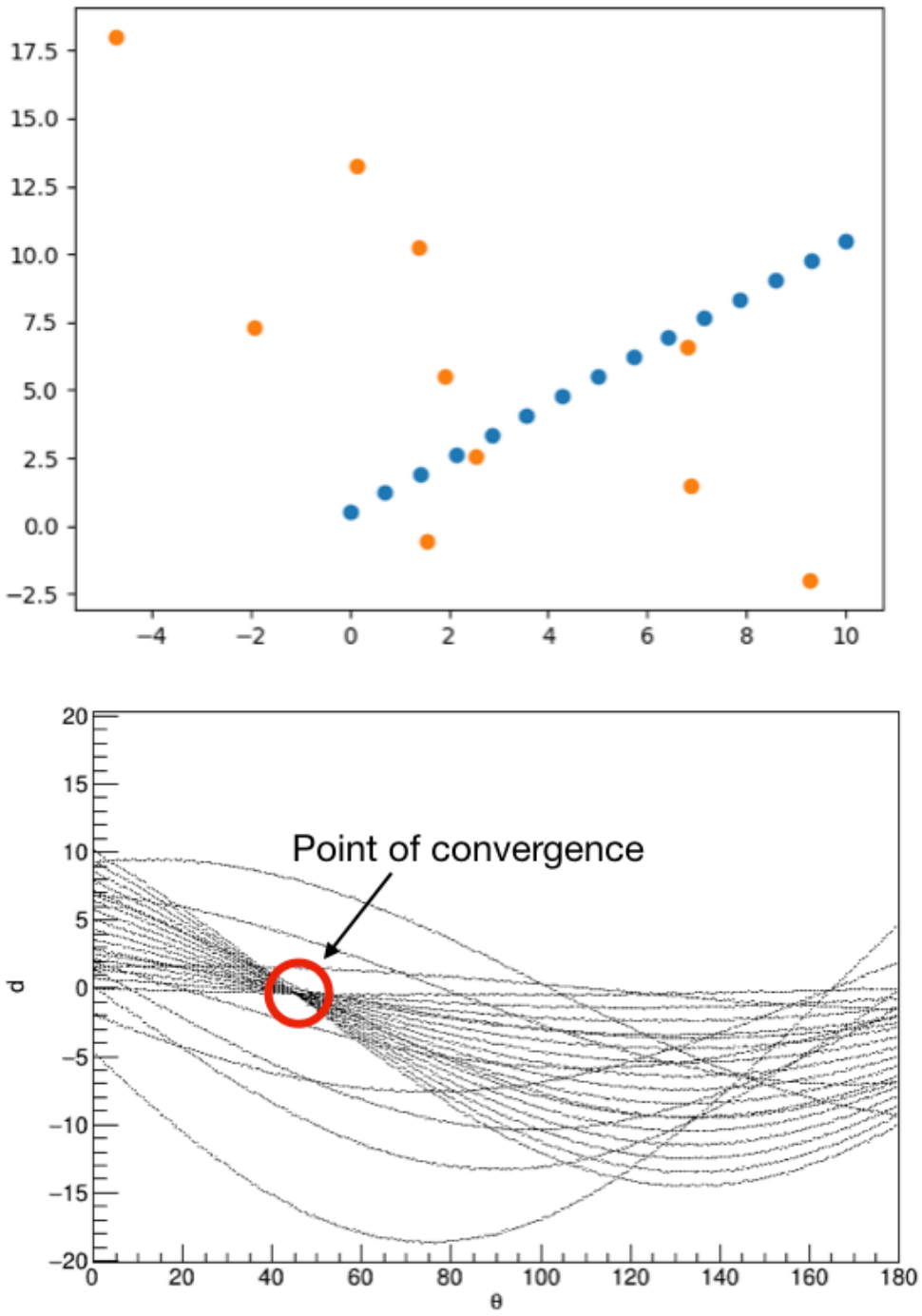

Figure 3.17: (Top) A straight line (blue points) with scattering noise (orange). (Bottom) The Hough space of the top points. Outlined in the red is the minimal standard deviation of d corresponding to the straight line of blue points.

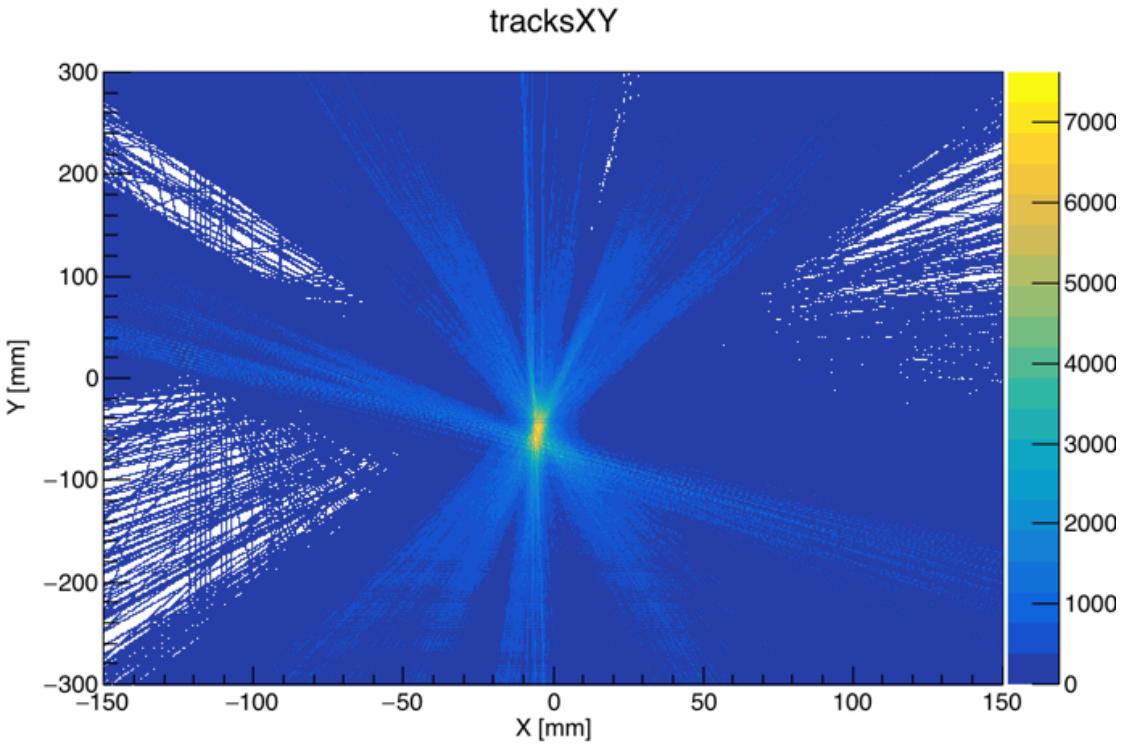

Figure 3.18: An accumulation of the alpha source tracks in the XY-plan in the forward and side walls. 0 mm on the y-axis corresponds to the beginning of the Micromegas plate. All of the tracks converge to ~ -60 mm where the source was located.

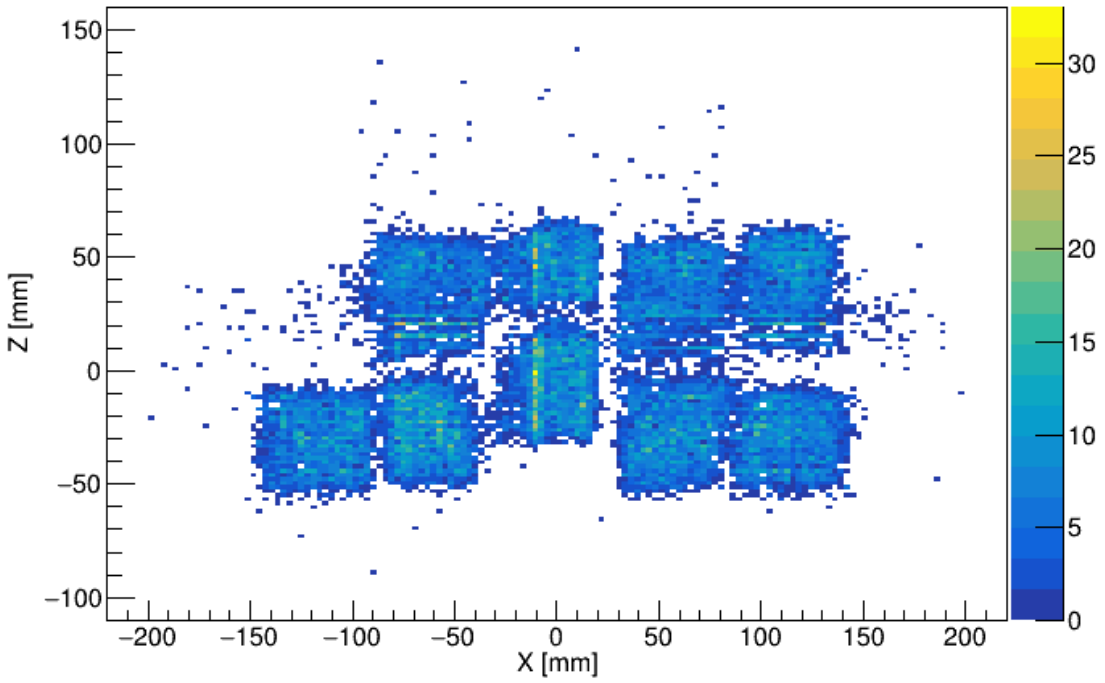

Figure 3.19: The XZ projection of the forward Si wall.

Beyond plotting the XY-plane of all the tracks, we also judge how well our track reconstruction is by plotting the position of the Si detectors. When fitting the tracks, none of the Si information is used to constrain the track reconstruction. The XZ reconstruction of where the Si detectors for the forward wall are located is shown in Figure 3.19. We clearly see the definitions of all nine Si detectors on the forward wall and see the gap corresponding to the missing Si detector in the top left corner. Although no Si information is used in the track reconstruction, it is recorded which Si quadrant fired. By using this information, we can get a better idea to how well the track reconstruction is by only plotting the XZ projection of the forward Si wall for certain quadrants that fired. Since the Si detectors used in this setup were all four quadrant detectors, the opposite corners of the Si detector were chosen to plot the XZ projection. These are shown in Figure 3.20. As shown, there is very good position reconstruction for each of the quadrants.

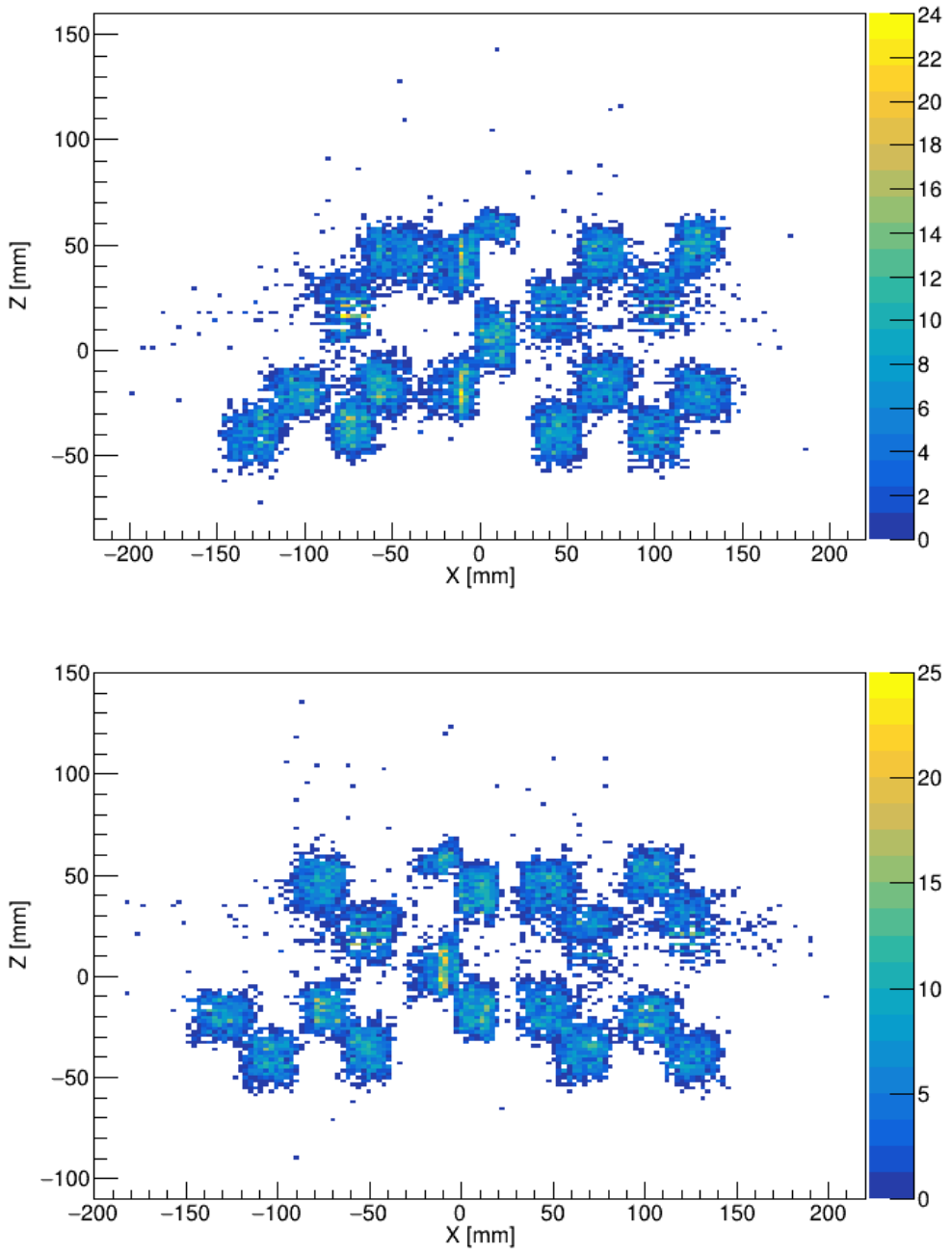

Figure 3.20: (Top) XZ projection of the Si wall choosing the lower left and upper right quadrants of each Si detector. (Bottom) XZ projection of the Si wall choosing the upper left and lower right quadrants of each Si detector.

3.6 Experimental Procedures

The readout scheme for the first commissioning run of the TexAT detector was as follows. The two PMTs upstream from the detector chamber were fed to a CFD with a threshold high enough to only trigger on the ^{8}B beam particles with all other beam contaminants below the threshold. The two outputs from the CFD were sent to a logic unit that triggers when both PMTs fire above the threshold. The trigger was then sent to a CAEN VME Scalar unit to count the number of beam ions for overall normalization. The CAEN Scalar was placed on its own data acquisition system separate from the GET electronics. The GET DAQ L1 trigger mode was used. It required coincidence between the ionization chamber and at least one Si detector channel. The digitizer was set to 25 MHz meaning that the waveforms were recorded every 40 ns and total window frame was 20 μs. The system was set in zero suppression mode so that all channels that fired above a threshold are recorded and written to disk but all other channels that have no hits or have hits below the threshold are ignored.

3.6.1 Beam Particle Identification

Separating the ^{8}B beam ions from the small contamination was done using the energy and timing from the ionization chamber. By measuring the energy deposited and the time relative to a signal in the Si detector, we can cut out the small amount of contamination. Note that the gas pressure was set so that ^{8}B ions were stopped long before they could hit the Si detector at zero degrees. Therefore, correlation between timing of the hit in a Si detector and that a ^{8}B ion in the ionization chamber is a signature of a nuclear reaction with ^{8}B that produced a light recoil. Figure 3.21 shows the energy and timing of the ionization chamber. For all good events, the ionization chamber time should all occur around the same time and in this spectrum this is between 5400 ns and 6500 ns. The energy peak of the ^{8}B beam in the ionization chamber is between channels 1300 and 1900. With these two quantities, we can clearly cut on the ^{8}B beam events.

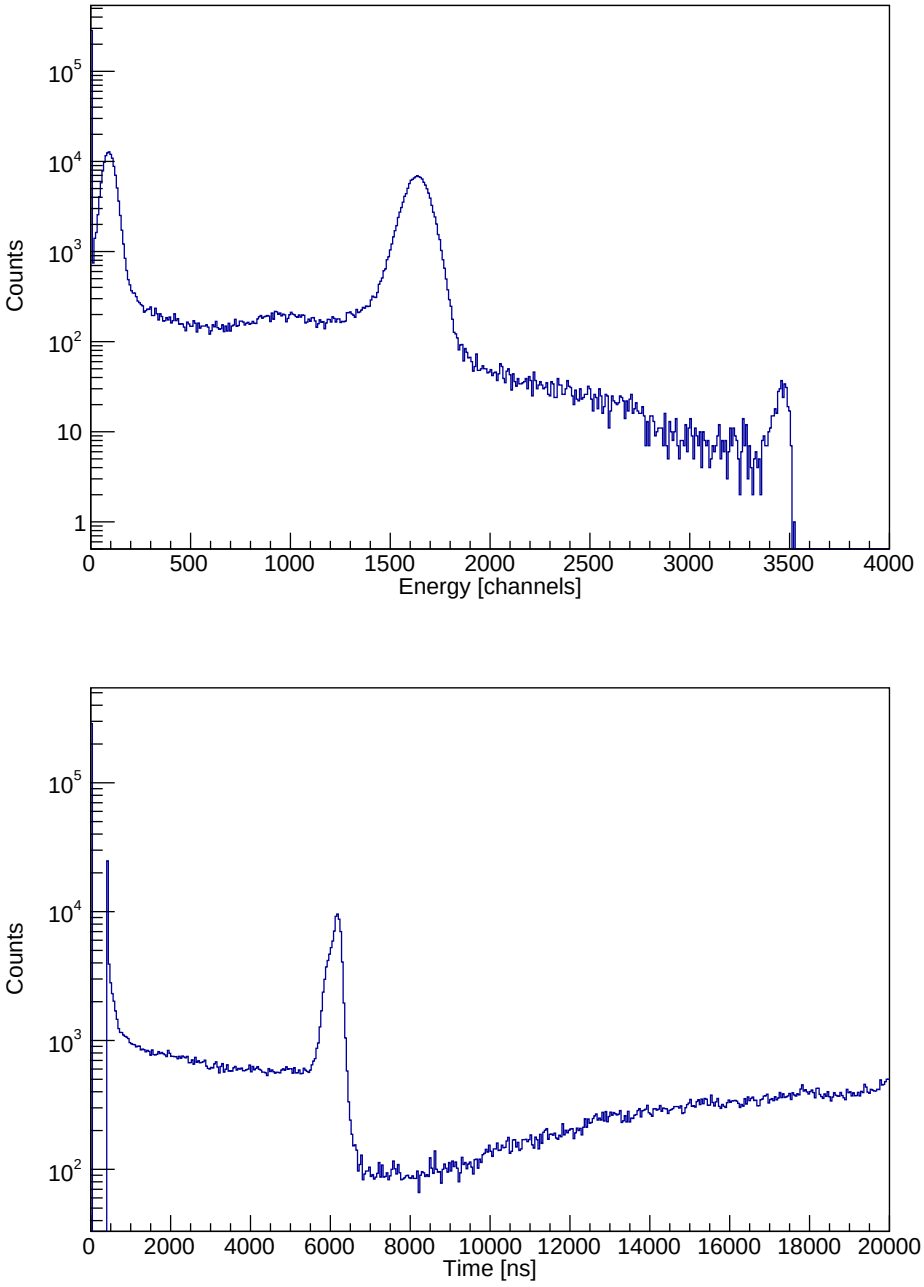

Figure 3.21: (Top) The energy of the ionization chamber. The ^{8}B peak is located between channels 1300-1900. (Bottom) The time of the maximum of the ionization chamber. The beam particles corresponding to the Si hit fall between 5400 ns to 6500 ns.

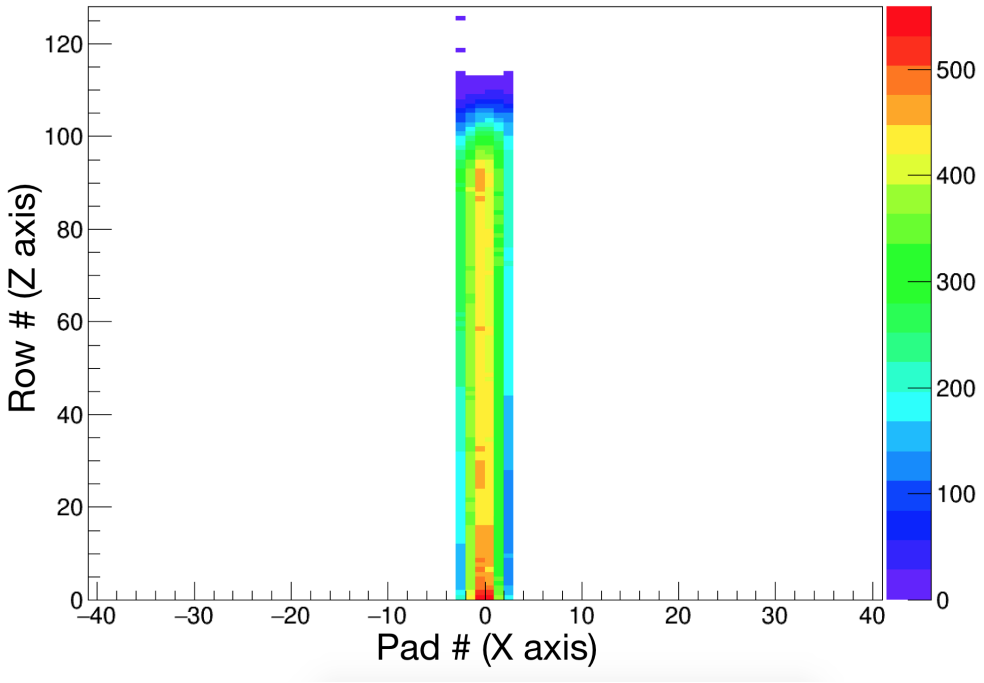

Figure 3.22: The cumulative counts in the central region of the Micromegas during the beam tuning. The pressure was adjusted to stop the beam about 1/8th from the end of the Micromegas.

3.6.2 Tuning of the beam

A huge benefit in this detector when compared to the detector used in the ^{10}N experiment is the ability to measure the incoming beam ions. This is especially useful when tuning the RIB into the chamber to make sure that it is coming in at the right angle and stopping in the correct location. Shown in Figure 3.22 is the cumulative counts in the central pads during the tuning process. As shown, the beam stops before the last 1/8th of the pads. Figure 3.23 is the average specific energy loss in the pads. The figure shows the Bragg curve which occurs as the beam travels further into the chamber and loses more and more energy, the specific energy loss over each pad becomes larger until it reaches the Bragg Peak around row number 90 (out of 128 total).

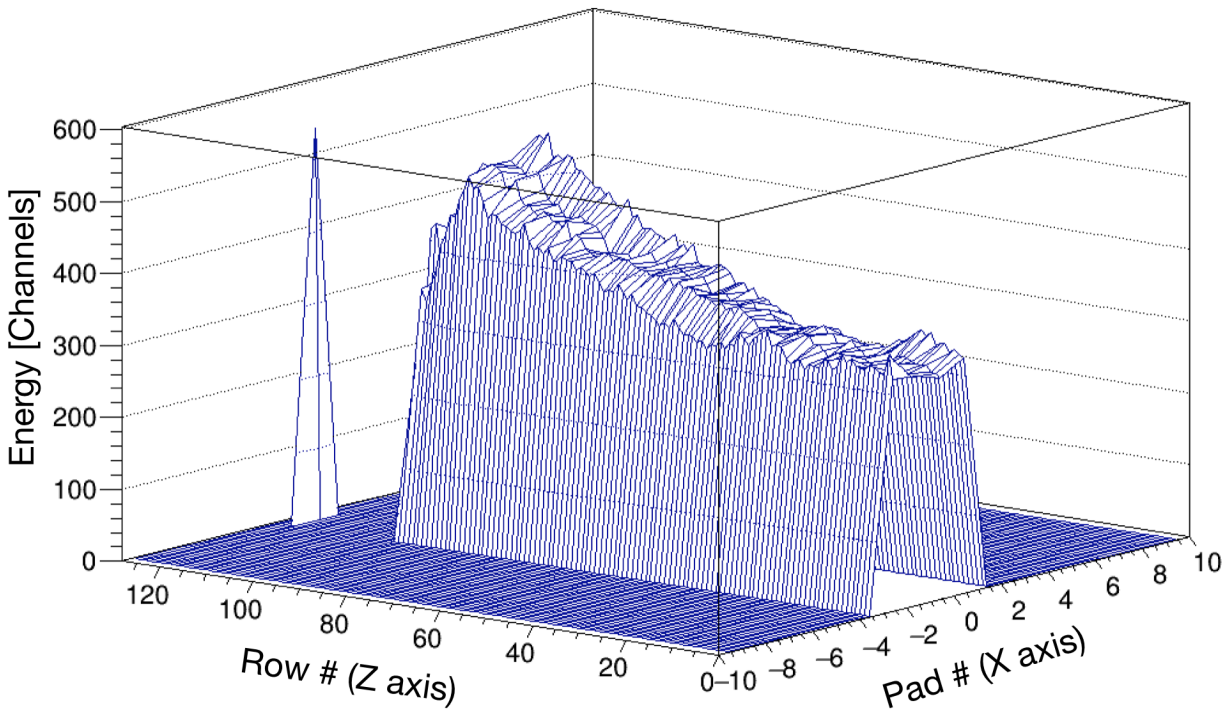

Figure 3.23: The energy deposited in each of the central region pads. The Bragg peak occurs around row number 90.

3.6.3 Low and High Gain Areas in the Micromegas Detector

The Micromegas detector was split into effectively two regions: one with low gain and another with high gain. The low gain region consists of the first 7/8th of the central pads in the beam direction. This low gain region is used to measure the incoming beam particle and the energy deposition along the pads. It had a Micromegas bias of 400 V. The last 1/8th of the central pad region closest to the Si detectors was biased at 600 V and is a high gain region which was used to measure the protons as the beam is stopped before this region. Both side regions were high gain regions biased at 570 V to also measure the scattered protons.

3.6.4 Selecting Proton Events

To clearly identify proton events, we used the specific energy loss in the high gain regions vs. the total energy in the Si and CsI detectors. Since not all events travel over the same

number of pads, we cannot use the total specific energy loss over the Micromegas but instead need to use the average specific energy loss per unit pad. This is especially necessary in the side regions since lower energy events happen closer to the Si detectors and when the proton goes over the side region, they do not travel over as many pads as events occurring closer to the entrance of the chamber. The specific energy loss per unit pad for the central detectors plotted against the total energy is shown in Figure 3.24. For the side regions, only the energy deposited in the strips are used to get the specific energy loss since the strips run perpendicular to the beam axis. This means that protons traveling in the forward direction will not skip over any strips nor will the geometry of the pad prevent the full measurement of the energy. The specific energy loss per unit pad plotted against total energy in the side region is shown in Figure 3.25. As shown in both of these figures, protons are easily identified and what is advantageous to this detector setup is the CsI behind the Si detectors allowing us to correctly identify punch-through events and reconstruct their energies unlike the ^{10}N measurement.

The gap in Figure 3.24 between ~ 9 and ~ 10 MeV corresponds to the threshold in the CsI detectors. The protons in this energy region do not deposit enough energy in the CsI to be recorded due to the threshold for the CsI(Tl) channels in GET electronics. Shown in Figure 3.26 is the Si energy plotted against the CsI energy in channels. As shown, we start recording a signal in the CsI detector when the punch-through protons are only depositing less than 7.5 MeV in the Si detector.

3.6.5 Removing Inelastic Scattering Events

In inelastic scattering one or both of the interacting nuclei undergo transition into an excited state as a result of interaction. In the case of ^{8}B+p inelastic scattering, ^{8}B can be excited to its first or higher lying excited states. There are no proton-bound excited states in ^{8}B because its proton decay threshold is located at 137 keV and the first excited state (1^{+}) is at 770 keV. As a result, any inelastic scattering event will produce two protons and a ^{7}Be recoil (which itself may be in its ground or excited state). By looking for the events

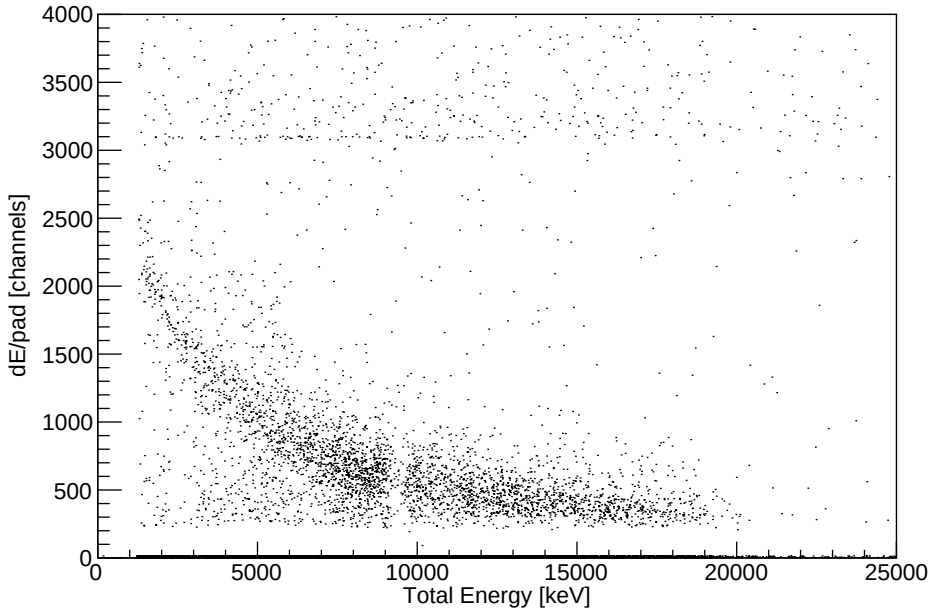

Figure 3.24: The specific energy loss per unit pad in the central region plotted against the total energy measured in the Si and CsI detector. The energy loss is measured in the last 1/8th in the central pads. Protons are clearly defined and a gap in spectrum between 9 and 10 MeV occur do to a threshold effect in the CsI.

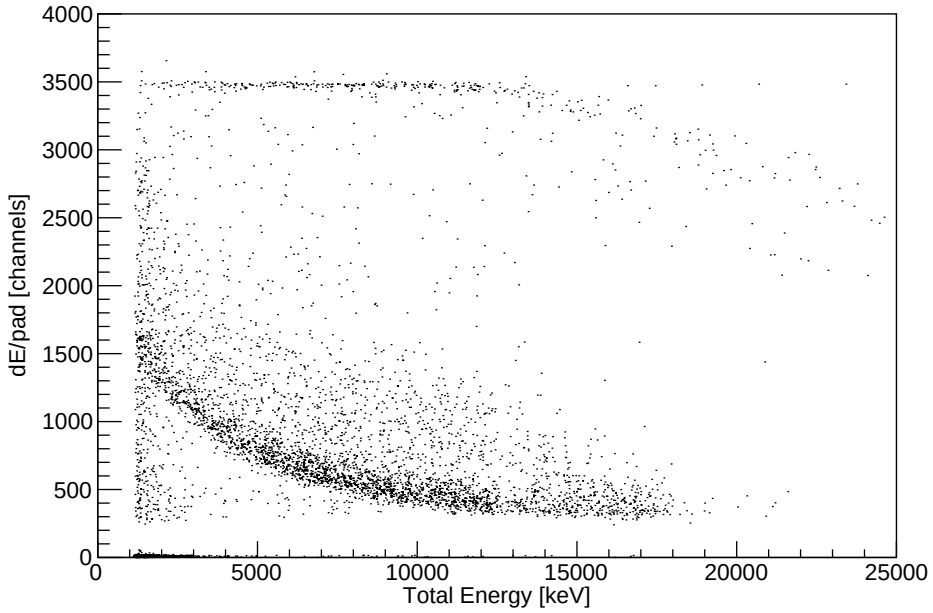

Figure 3.25: The specific energy loss per unit pad of the strips in the side region plotted against the total energy measured in the Si and CsI detector. Protons are the only particle than can be identified in the spectrum.

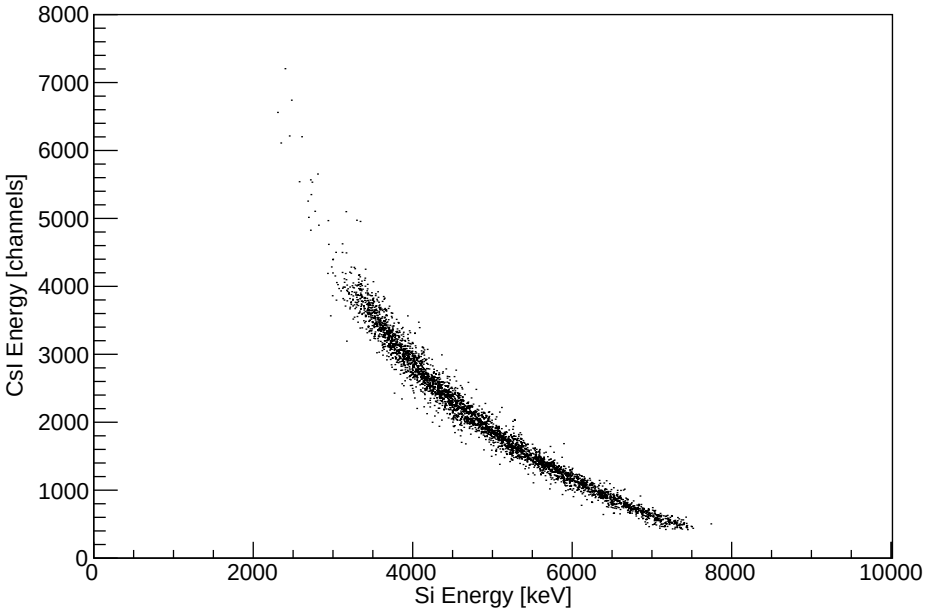

Figure 3.26: The energy recorded in the CsI detector in channel number plotted against the measured energy (in keV) in the Si detector. Only proton events punch-through the Si detector to deposit energy in the CsI.

with two proton tracks, we can identify these inelastic scattering events.

Using the total energy in the Si and CsI detectors and the Micromegas, we can clearly identify protons that hit one of the Si detectors and triggered the DAQ, but "second" protons produced by an inelastic scattering event do not always hit any Si detector. Therefore, we cannot rely on specific energy loss vs. the total measured energy and need to identify protons by only using their tracks in the gas. Specific energy loss of Z=1 nuclei is very different from that of heavier recoils (e.g. ^{7}Be) and there appears to be no or very few deuterons or tritons produced in the interaction of ^{8}B with the methane gas (see Fig. 3.24 and 3.25). So, by comparing specific energy loss per unit pad we can determine if the particle is a heavy recoil or a proton. Examples of protons measured in the side regions and the second proton is measured in the central region (Figure 3.27) and opposite side region (Figure 3.28) are shown. By identifying these events, we are able to exclude them from the excitation function for resonance elastic scattering. The excitation function for inelastic scattering can also be

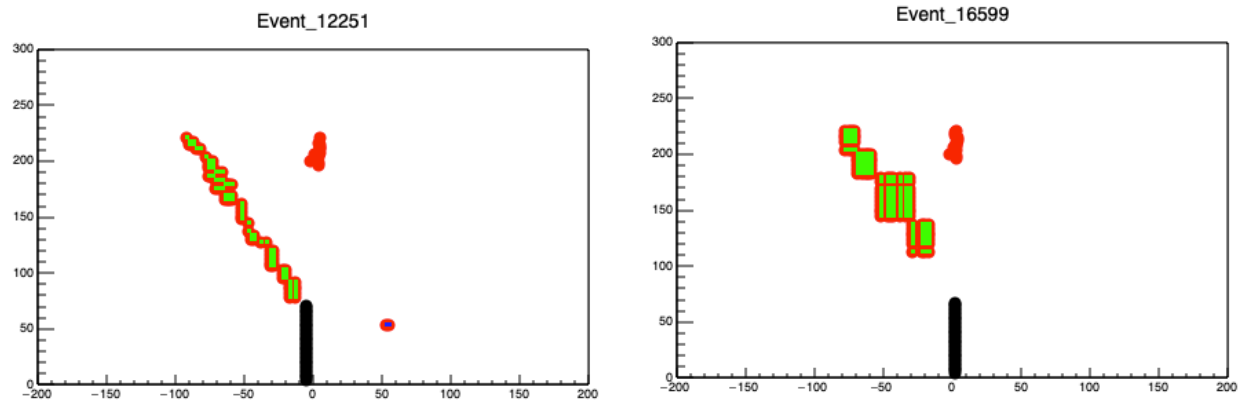

Figure 3.27: Inelastic events where a proton is measured in one side of the Micromegas plate and a proton in the central region.

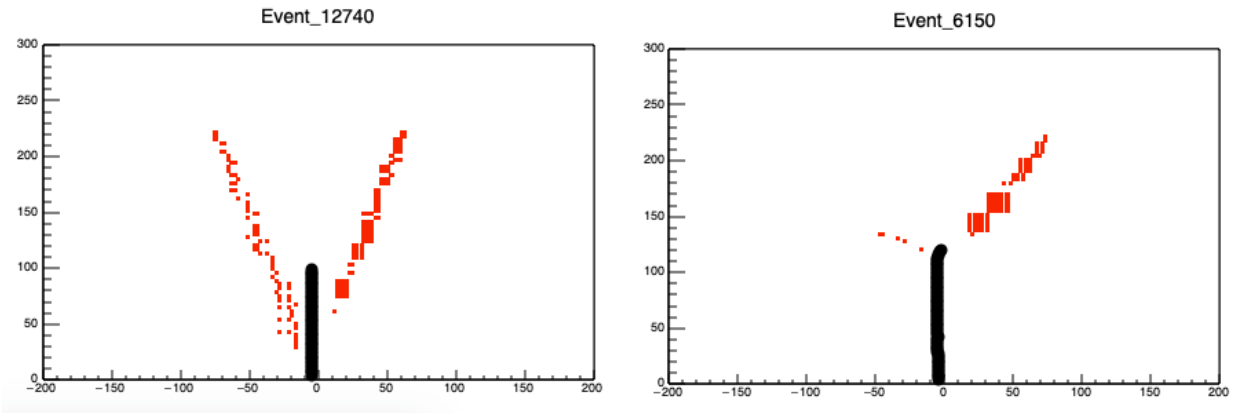

Figure 3.28: Inelastic events where protons are measured in both sides of the Micromegas plate.

constructed, but I am only focusing on the analysis of elastic scattering events in this thesis.

3.6.6 Vertex Reconstruction in the Central Region

As the ^{8}B beam travels over the Micromegas, it deposits energy by ionizing gas in the region of central pads. When a reaction occurs over the Micromegas, such as elastic proton scattering, the energy deposition changes. At this reaction point, there is a jump in specific energy loss because ^{8}B ion transfers a fraction of its energy to the target proton and therefore specific energy loss changes instantaneously at the interaction point. This energy jump

can be directly observed in the pads as long as the vertex is over the Micromegas. In this measurement, only events below $E_{\text{c.m.}} = 3.2$ MeV will have a vertex position over the Micromegas plate. An alternative way to determine the vertex location for central events and for events produced at c.m. energies above 3.2 MeV is to identify the location of the Bragg peak for a heavy recoil. Since the elastically scattered proton events measured in the central detectors travel at angles close to zero degrees, the heavy recoil also travels at angles close to zero (due to momentum conservation). This heavy recoil is then measured completely over the central pad region of the Micromegas. The energy of the heavy recoil produced in the ^{8}B+p elastic scattering depends on the location of the interaction or c.m. energy. These scattered recoils with higher energies travel further through the gas and the location of the Bragg peak can be measured. Two typical events of this kind are shown in Figure 3.29. By using kinematics and energy loss, we can formulate a way to relate the maximum energy deposition in the Micromegas with the vertex location. This is used to determine the vertex position for the events that produced a proton in the central region. The vertex position determined this way is plotted against the total energy measured in the Si and CsI in Figure 3.30. As expected, the vertex position is further away from the Si detectors (vertex position going further negative) as the total energy becomes higher. This figure demonstrates that vertex location can be reliably identified even if an interaction occurs outside of the active region of Micromegas (negative values along the y axis in Fig. 3.30).

3.6.7 Vertex Reconstruction in the Side Regions

Once we are able to identify proton events in the side region, we can match the strips and chains as discussed above. These proton tracks can then be analyzed using the Hough transform and traced back to the beam axis to find the vertex location. For events where the vertex is over the Micromegas and the incoming beam is measured, the proton track is traced to the measured incoming beam track. For higher energy events, the beam information is not measured in the Micromegas detector and the proton track is traced back to the ideal beam axis. The measured vertex position vs. total energy is shown in Figure 3.31. As in

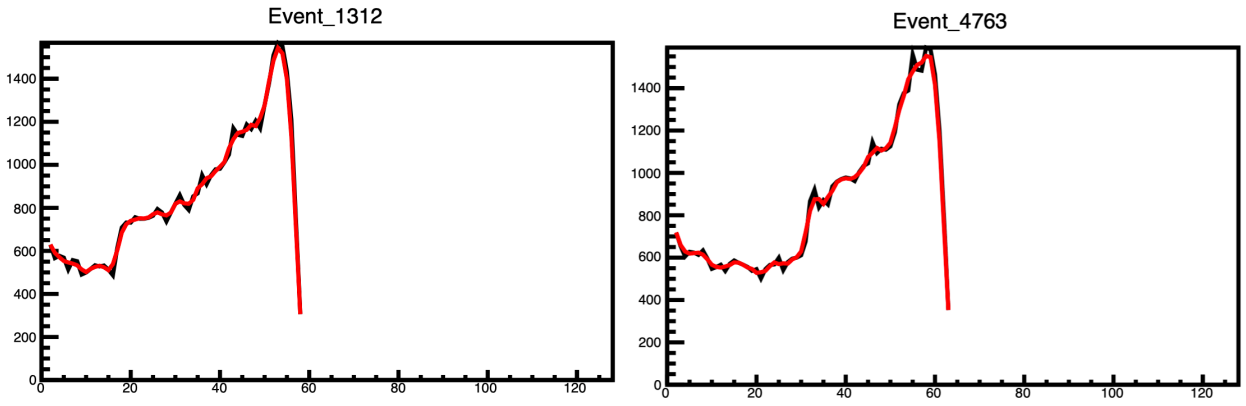

Figure 3.29: Specific energy loss of the beam and heavy scattered recoil vs. row number in Micromegas along the beam axis. Black lines are the raw energy values while the red curve is the running average. (Left) The vertex location is around row 20 while the maximum specific energy loss is around row 50. (Right) The vertex location is around row 30 while the maximum specific energy loss is around row 60.

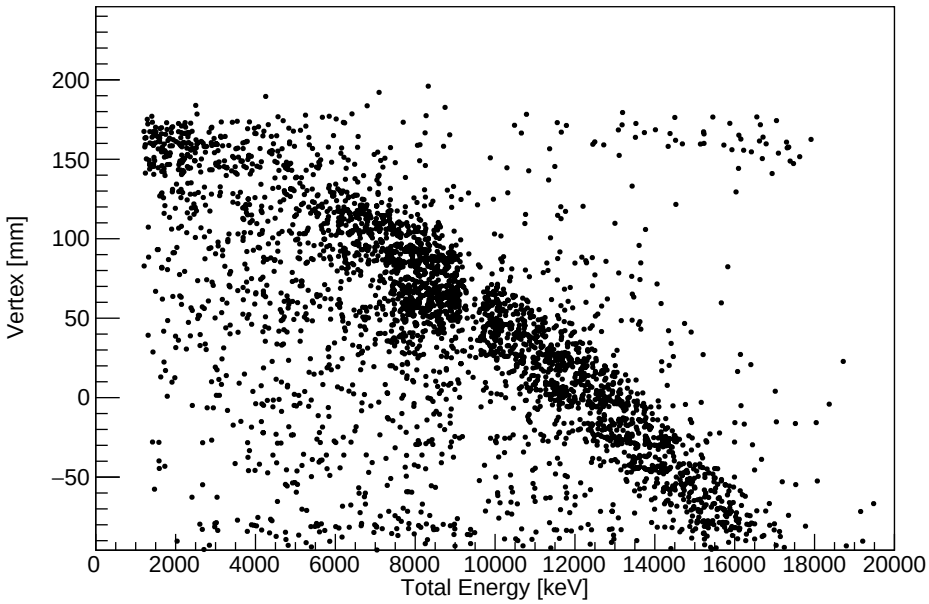

Figure 3.30: Vertex position vs. total energy measured in the Si and CsI detectors for the central forward detectors. The gap between energies 9 and 10 MeV occur due to a threshold effect for the CsI detectors.

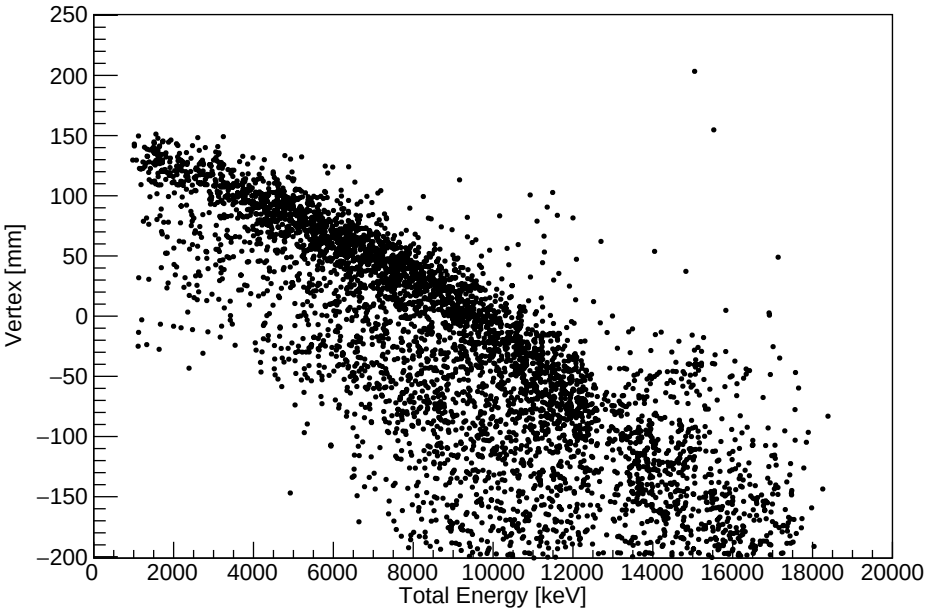

Figure 3.31: Vertex position vs total energy measured in the Si and CsI detectors for the outside forward detectors. The gap between energies 12 and 13 MeV occur due to a threshold effect for the CsI detectors.

the case of the central region, elastically scattered events occur further away for high energy events and thus higher c.m. energy events.

3.6.8 Measured Excitation Function and R-matrix Analysis

With identification of protons and reconstruction of tracks the elastic scattering events can be cleanly identified, the kinematics of each event reconstructed and the excitation function for elastic scattering can be established. Since all tracks are measured explicitly, the path length through the gas is known for each proton. A correction for (small) proton energy losses in the gas can be made using energy losses of protons in the methane gas as calculated by the well established code SRIM [62]. The c.m. energy for the interaction and the cross section can then be determined using Equations 2.8, 2.9, 1.8 and 1.9.

For the commissioning TexAT run, we were only able to obtain the excitation function for two regions, the central zero degree detectors in the forward wall of the Si array and the three

outside detectors in the forward wall. The other Si detector were unusable due to an uneven dead layer on the back side of the Si detectors. This was apparent while plotting the measured Si energy vs. the CsI energy. The band for an even dead layer detector is shown in Figure 3.26 while for an uneven dead layer detector, this band is much broader. This made energy reconstruction for any punch-through events and thus the excitation function unreliable. These low quality detectors were later replaced for the subsequent TexAT experiments.

The excitation spectrum for the two regions are shown in Figure 3.32. We were able to extend the excitation function to 6.3 MeV, almost 2 MeV higher than the previous measurement [16]. R-matrix calculations were performed using the code AZURE2 [73] with a channel radius of $a = 4.5$ fm. The analysis procedure followed the "minimalistic" approach - I start with the known states in ^{9}C and add only a minimal number of new states to reproduce the measured excitation function. The goal was not so much to produce a "perfect" fit but to conclusively demonstrate the necessity for new state(s) (if any) and to determine the spin-parities of the new state(s). Figure 3.33 shows R-matrix calculations for the two regions. The black solid line is the three states from [16]: the $J^{\pi} = 1/2^{-}$, $J^{\pi} = 5/2^{-}$ and $J^{\pi} = 3/2^{-}$ states located at $E_{ex} = 2.22$ MeV, 3.6 MeV and 4.1 MeV respectively. Although these states fit the previously measured spectrum near zero degrees and up to 4.5 MeV in excitation energy reasonably well, the excitation function at higher energies is not reproduced. More importantly, the outside forward region (smaller scattering angles that were not measured in [16]) has the completely wrong shape even at lower energies. The blue dash-dotted curve in Figure 3.33 are the same $J^{\pi} = 1/2^{-}$ and $J^{\pi} = 5/2^{-}$ states but instead of a $J^{\pi} = 3/2^{-}$ state, it is replaced by a $J^{\pi} = 7/2^{-}$ state at higher energy (6.5 MeV), which is the next negative parity state predicted by the shell model (see Fig. 3.7). Once again, it does not match higher energies in the central forward region nor the shape in the outside forward region. Since we now have an excitation function at low c.m. angles down to 105° that was not available previously [16], we can conclude that the experimental data cannot be reproduced with only $\ell = 1$ states. A broad $\ell = 0$ state with spin-parity $J^{\pi} = 5/2^{+}$ is necessary to reproduce

the shape of the excitation function at all measured scattering angles simultaneously. The R-matrix fit with the known $1/2^-$ and $5/2^-$ states and a new $5/2^+$ state at ∼4.0 MeV and width of 4.0 MeV is shown as the green dashed line in Figure 3.33. This configuration better matches the higher energy part of the central forward detectors and the shape of the outside forward region. The effect of a broad $\ell = 1$, $J^\pi = 7/2^-$ state at $E = 6.5$ MeV is shown as the red dotted curve in Figure 3.33. Its addition appears to be improving the fit.

The $3/2^+$ spin-parity assignment for the new $\ell = 0$ state was considered and is shown in Figure 3.34 as a green dashed curve. It does not match the shape of the spectrum in the outer forward detector, while still fitting the central forward spectrum reasonably well. The $1/2^+$ spin-parity assignment would require $\ell = 2$ for the elastic channel (spin-parity of ^{8}B(g.s.) is 2^+) - but the only way to reproduce the spectrum at smaller c.m. scattering angles is to introduce a strong $\ell = 0$ state.

We conclude that a broad $\ell = 0$ state at excitation energy around 4 MeV with a spin-parity of $J^\pi = 5/2^+$ is necessary to simultaneously reproduce the excitation function for ^{8}B+p resonance elastic scattering at all angles, indicating the start of the sd-shell in ^{9}C. These results are in agreement with recent measurements [17] that claimed observation of a broad $J^\pi = 1/2^+$ or $J^\pi = 5/2^+$ state at $E = 4.40 \pm 0.04$ MeV. More constrains on the level structure of ^{9}C may be obtained in the follow up analysis of the inelastic scattering excitation function but it is outside of the scope of this thesis.

3.7 Conclusion

We have populated states in ^{9}C using ^{8}B+p resonance elastic scattering at the Cyclotron Institute at Texas A&M university. We extended the excitation function 2 MeV beyond the previous ^{8}B+p measurement and were able to extract the excitation function down to c.m. angles of 105°. To reproduce the spectra in both angular regions, $J^\pi = 1/2^-$ and $J^\pi = 5/2^-$ states were used from [16] in addition to a $J^\pi = 5/2^+$ state at $E = 4$ MeV with a width of $\Gamma = 4$ MeV. To further improve the fit at higher energies, a $J^\pi = 7/2^-$ state at $E = 6.5$ MeV and width $\Gamma = 2.0$ MeV was introduced, although data at higher excitation energies are

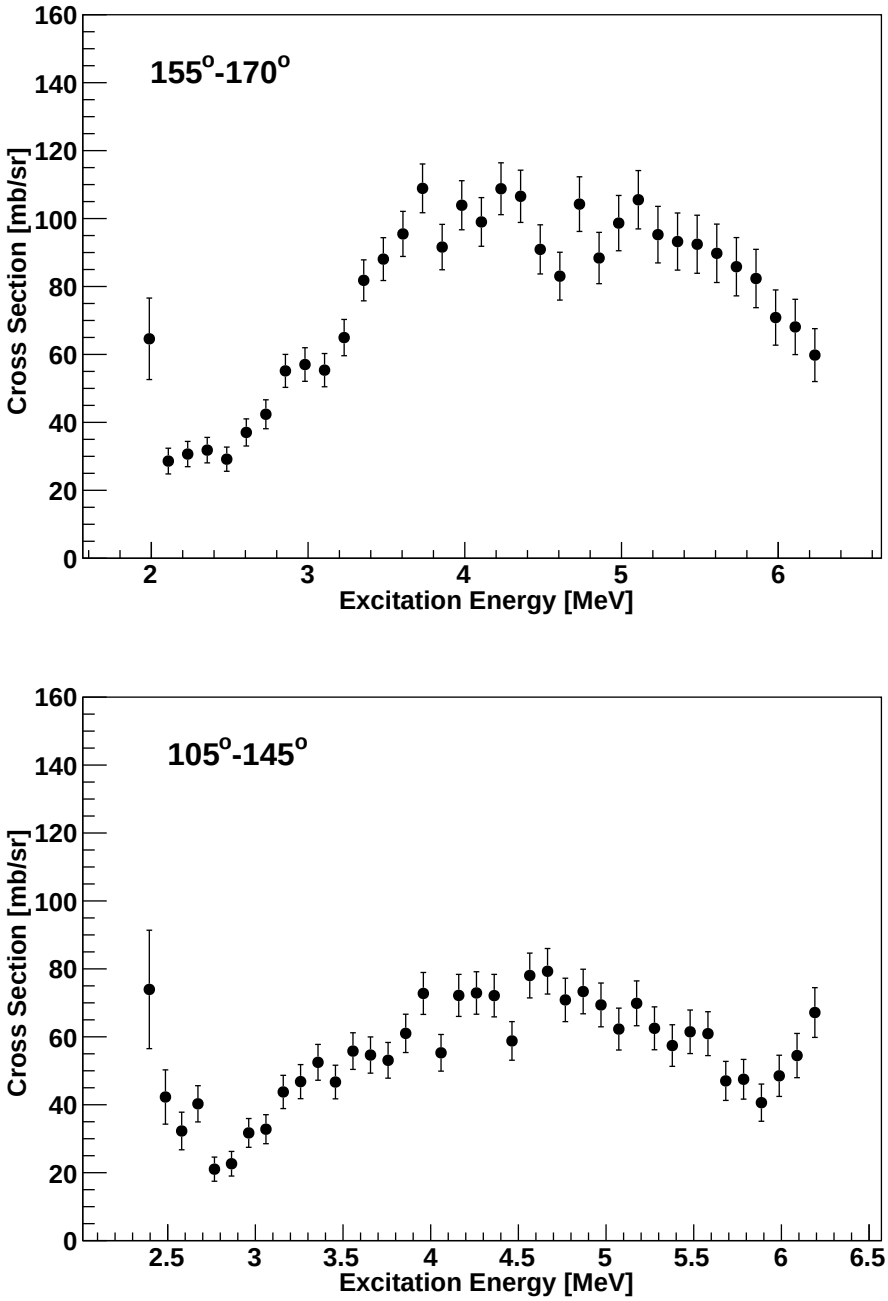

Figure 3.32: Cross section vs. excitation energy for the center forward detectors (top) and outside forward detectors (bottom) for ^{8}B + p resonance elastic scattering.

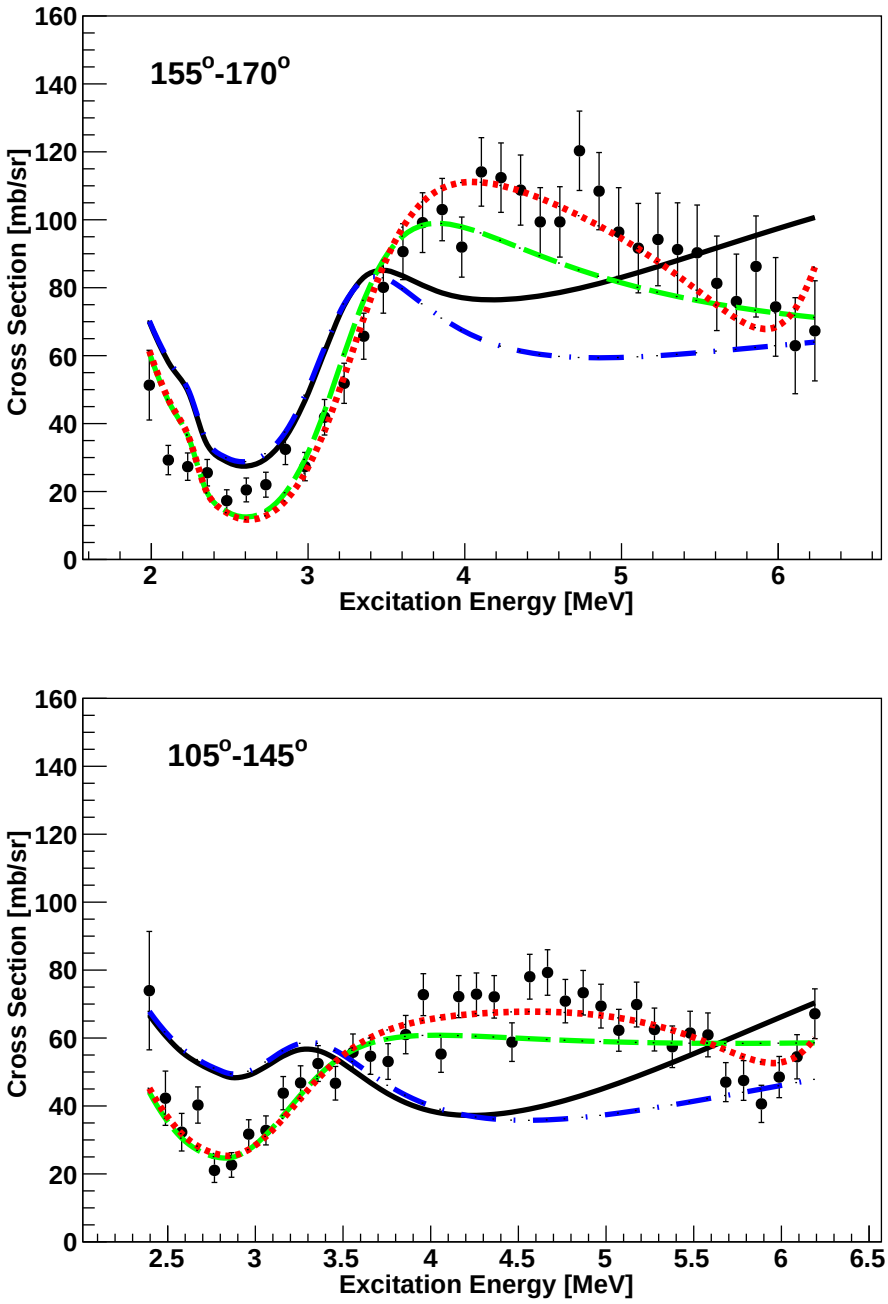

Figure 3.33: R-matrix calculations and experimental data for both regions. The black solid line are the three states from [16]: the $J^\pi = 1/2^-$, $J^\pi = 5/2^-$ and $J^\pi = 3/2^-$ states. The blue dash-dotted curve include the $J^\pi = 1/2^-$, $J^\pi = 5/2^-$ and $J^\pi = 7/2^-$. The green dashed curve includes the $J^\pi = 1/2^-$, $J^\pi = 5/2^-$ and $J^\pi = 5/2^+$ while the red dotted curve is the same configuration but with an added $J^\pi = 7/2^-$ state.

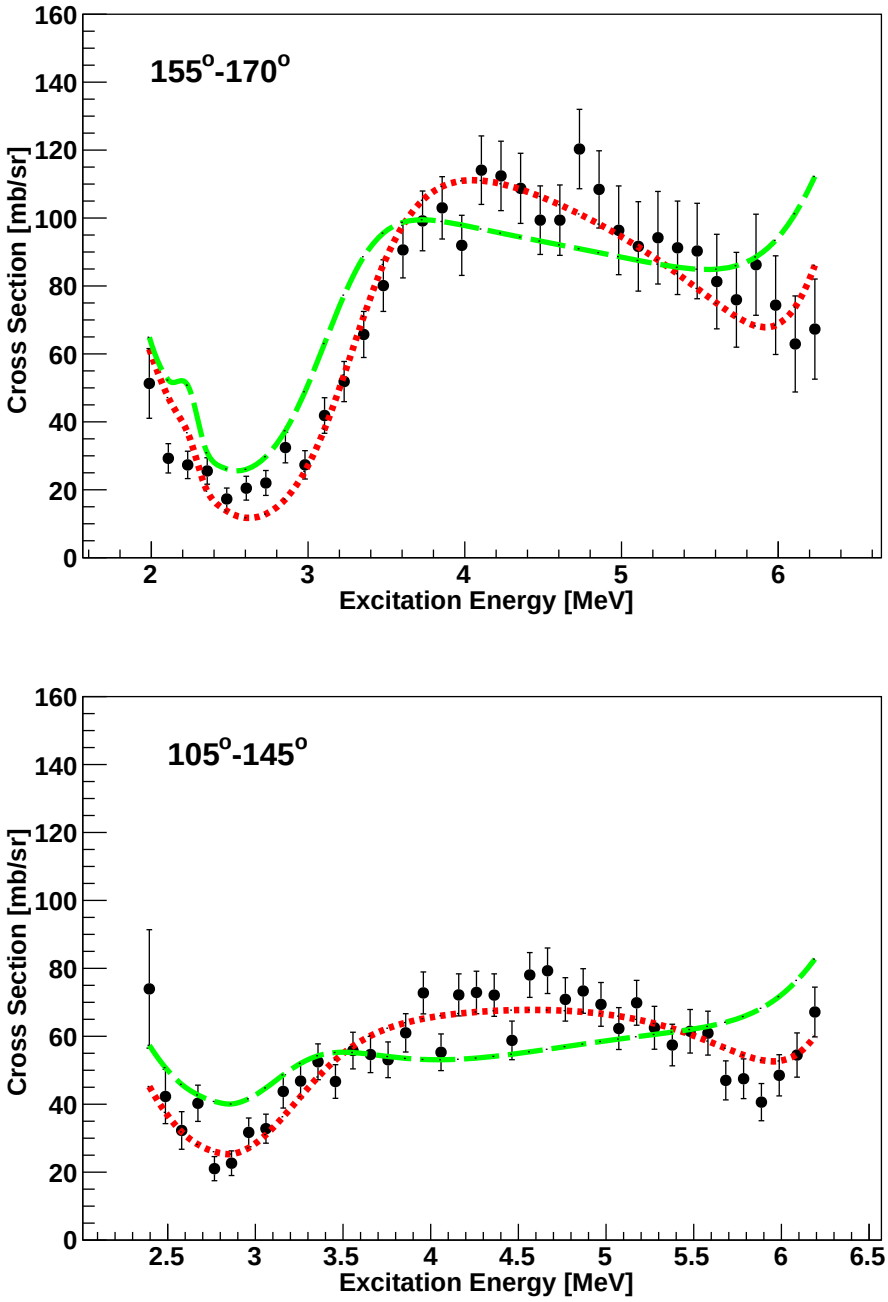

Figure 3.34: R-matrix calculations and experimental data for both regions. All three calculations include the $J^\pi = 1/2^-$, $J^\pi = 5/2^-$ and $J^\pi = 7/2^-$ states. The blue solid curve is the $J^\pi = 1/2^+$ state, the green dashed curve is the $J^\pi = 3/2^+$ state while the red dotted line the $J^\pi = 5/2^+$ state.

needed to confirm this state. It can only be considered as tentative. The broad $J^{\pi} = 5/2^{+}$ state at $E = 4$ MeV is the start of the sd-shell in ^{9}C and is the first sd-shell state observed in any of the T = 3/2 A = 9 nuclei.

Beyond looking and finding the start of the sd-shell in ^{9}C, this experiment was used as a commissioning run of the Texas Active Target detector. As with any commissioning run, there were a few obstacles to overcome but this experiment was successful. With the lessons learned and the analysis tools now developed, the TexAT detector is now ready to serve as a versatile tool for experiments with rare isotope beams it was designed for.

4. CONCLUSION

The study of proton-rich exotic nuclei provides a benchmark for developments in nuclear theories. It has been shown that resonance proton elastic scattering with the use of time projection active target detectors is an excellent way to study these nuclei.

There has now been more light shown on the ^{10}Li problem by studying its mirror nucleus, ^{10}N, using the ^{9}C+p resonance elastic scattering reaction. ^{10}Li plays a key role in the structure of the two neutron halo system ^{11}Li. Two broad $\ell = 0$ resonances were found and the first observation of the ground state and first excited state of ^{10}N were made. There was no evidence for p-wave resonances but they cannot be ruled out based on the present data. The $2s_{1/2}$ shell in ^{10}N has been located at 2.3 ± 0.2 MeV above the proton threshold. This finding, combined with the isospin symmetry considerations, allows us to conclude that in ^{10}Li the 2s-shell has to be located just above the neutron decay threshold (within 100 keV).

The first commissioning run of the TexAT detector was performed in which the structure of ^{9}C was studied using ^{8}B+p resonance elastic scattering. With this commissioning run, the tools to analyze the active target detector data have been developed. The ^{8}B+p excitation function has been measured in wide energy and angular region and R-matrix analysis was performed. The new $J^{\pi} = 5/2^{+}$ state at $E = 4$ MeV was observed. It indicates the start of the sd-shell in ^{9}C. This is the first positive parity state that was conclusively observed in any of the T = 3/2 A = 9 nuclei.

4.1 Future Outlook

The future outlook for experiments using the TexAT detector is very bright. As expected for a commissioning experiment, we had several unforeseen problems such as the loss of channels in the electronics, bad Si detectors used in part of the forward wall and completely covering the side wall rendering the spectrum from these regions useless. The commissioning run has also revealed shortcomings in some of the Micromegas design ele-

ments. We lost several channels in the Micromegas board due to sparking. Unfortunately, all of these channels where in the high gain region of the Micromegas which resulted in less than ideal proton track reconstruction. In spite of these shortcomings, we were still able to get high quality data and observed the begining of the sd-shell in ^{9}C.

In the future, the inclusion of a GEM detector placed over the mesh of the Micromegas would allow lower bias voltage on the Micromegas and thus less chances of sparking and losing channels. Of the 15 Si detectors used in the commissioning run, 10 we unusable due to a non-uniform dead layer on the back side of the detector. Since the dead layer was on the back side of the detector, it was not noticed during alpha source calibration and only noticed when looking at proton punch-through events. The uneven dead layer does not allow for proper energy reconstruction of these punch-through events with the CsI detectors.

This commissioning run was critical and paved the way for future TexAT experiments. We have identify problems and fixed several issues already. We also have plans for future improvements. The analysis tools built during the analysis of the commissioning run and the experience gained are both critical.

REFERENCES

[1] C. Iliadis, *Nuclear Physics of Stars*. Wiley-VCH, 2007.

[2] K. S. Krane, *Introductory Nuclear Physics*. Wiley, 1987.

[3] B. R. Barrett, P. Navratil, and J. P. Vary, "Ab initio no core shell model," *Prog. Part. Nucl. Phys.*, vol. 69, pp. 131–181, 2013.

[4] J. Carlson, S. Gandolfi, F. Pederiva, S. C. Pieper, R. Schiavilla, K. E. Schmidt, and R. B. Wiringa, "Quantum Monte Carlo methods for nuclear physics," *Rev. Mod. Phys.*, vol. 87, p. 1067, 2015.

[5] T. Frederico, A. Delfino, L. Tomio, and M. T. Yamashita, "Universal aspects of light halo nuclei," *Prog. Part. Nucl. Phys.*, vol. 67, pp. 939–994, 2012.

[6] E. Caurier, P. Navratil, W. E. Ormand, and J. P. Vary, "Ab initio shell model for A=10 nuclei," *Phys. Rev.*, vol. C66, p. 024314, 2002.

[7] H. Simon, M. Meister, T. Aumann, M. J. G. Borge, L. V. Chulkov, U. Datta Pramanik, T. W. Elze, H. Emling, C. Forssén, H. Geissel, M. Hellström, B. Jonson, J. V. Kratz, R. Kulessa, Y. Leifels, K. Markenroth, G. Münzenberg, F. Nickel, T. Nilsson, G. Nyman, A. Richter, K. Riisager, C. Scheidenberger, G. Schrieder, O. Tengblad, and M. V. Zhukov, "Systematic investigation of the drip-line nuclei ^{11}Li and ^{14}Be and their unbound subsystems ^{10}Li and ^{13}Be," *Nucl. Phys.*, vol. A791, pp. 267–302, 2007.

[8] H. B. Jeppesen, A. M. Moro, U. C. Bergmann, M. J. G. Borge, J. Cederkäll, L. M. Fraile, H. O. U. Fynbo, J. G'omez-Camacho, H. T. Johansson, B. Jonson, M. Meister, T. Nilsson, G. Nyman, M. Pantea, K. Riisager, A. Richter, G. Schrieder, T. Sieber, O. Tengblad, E. Tengborn, M. Turrión, and F. Wenander, "Study of ^{10}Li via the ^{9}Li(^{2}H, p) reaction at REX-ISOLDE," *Phys. Lett.*, vol. B642, pp. 449–454, 2006.

[9] M. Cavallaro, M. De Napoli, F. Cappuzzello, S. E. A. Orrigo, C. Agodi, M. Bondí, D. Carbone, A. Cunsolo, B. Davids, T. Davinson, A. Foti, N. Galinski, R. Kanungo, H. Lenske, C. Ruiz, and A. Sanetullaev, "Investigation of the ^{10}li shell inversion by neutron continuum transfer reaction," *Phys. Rev. Lett.*, vol. 118, p. 012701, 2017.

[10] A. Sanetullaev, R. Kanungo, J. Tanaka, M. Alcorta, C. Andreoiu, P. Bender, A. A. Chen, G. Christian, B. Davids, J. Fallis, J. P. Fortin, N. Galinski, A. T. Gallant, P. E. Garrett, G. Hackman, B. Hadinia, S. Ishimoto, M. Keefe, R. Krücken, J. Lighthall, E. McNeice, D. Miller, J. Purcell, J. S. Randhawa, T. Roger, A. Rojas, H. Savajols, A. Shotter, I. Tanihata, I. J. Thompson, C. Unsworth, P. Voss, and Z. Wang, "Investigation of the role of ^{10}Li resonances in the halo structure of ^{11}Li through the ^{11}Li(p,d)^{10}Li transfer reaction," *Phys. Lett.*, vol. B755, pp. 481–485, 2016.

[11] A. Lépine-Szily, J. M. Oliveira Jr, V. R. Vanin, A. N. Ostrowski, R. Lichtenthäler, A. Di Pietro, V. Guimarães, A. M. Laird, L. Maunoury, G. F. Lima, F. de Oliveira Santos, P. Roussel-Chomaz, H. Savajols, W. Trinder, A. C. C. Villari, and A. de Vismes, "Observation of the particle unstable nucleus ^{10}N," *Phys. Rev.*, vol. C65, p. 054318, 2002.

[12] B. T. Roeder, A. Saastamoinen, and S. A., "Mars status report for 2014-2015," *Progress in Research*, pp. IV–25, 2014 - 2015.

[13] J. Hooker, G. V. Rogachev, V. Z. Goldberg, E. Koshchiy, E. Koshchiy, B. T. Roeder, H. Jayatissa, C. Hunt, C. Magana, S. Upadhyayula, E. Uberseder, and A. Saastamoinen, "Structure of ^{10}N in ^{9}C+p resonance scattering," *Phys. Lett.*, vol. B769, pp. 62–66, 2017.

[14] J. Cerny, R. H. Pehl, F. S. Goulding, and D. A. Landis, "Completion of the Mass-9 Isobaric Quartet via the Three-Neutron Pickup Reaction ^{12}C(^{3}He, ^{6}He) ^{9}C," *Phys. Rev. Lett.*, vol. 13, pp. 726–728, 1964.

[15] W. Benenson and E. Kashy, "First excited A=9 isospin quartet," *Phys. Rev.*, vol. C10, pp. 2633–2635, 1974.

[16] G. V. Rogachev, J. J. Kolata, A. S. Volya, F. D. Becchetti, Y. Chen, P. A. DeYoung, and J. Lupton, "Spectroscopy of ^{9}C via resonance scattering of protons on ^{8}B," *Phys. Rev.*, vol. C75, p. 014603, 2007.

[17] K. W. Brown, R. J. Charity, J. M. Elson, R. W., L. G. Sobotka, W. W. Buhro, Z. Chajecki, W. G. Lynch, J. Manfredi, R. Shane, R. H. Showalter, M. B. Tsang, D. Weisshaar, and J. R. Winkelbauer, "Proton-decaying states in light nuclei and the first observation of ^{17}Na," *Phys. Rev.*, vol. C95, no. 4, p. 044326, 2017.

[18] A. Volya and V. Zelevinsky, "Continuum shell model and nuclear physics at the edge of stability," *Phys. Atom. Nucl.*, vol. 77, pp. 969–982, 2014.

[19] E. Koshchiy, G. V. Rogachev, E. Uberseder, and P. E., "Texas active target (texat) detector - part 1: Design and construction progress," *Progress in Research*, pp. IV–42, 2014 - 2015.

[20] E. P. Wigner and L. Eisenbud, "Higher Angular Momenta and Long Range Interaction in Resonance Reactions," *Phys. Rev.*, vol. 72, pp. 29–41, 1947.

[21] A. M. Lane and R. G. Thomas, "R-Matrix Theory of Nuclear Reactions," *Rev. Mod. Phys.*, vol. 30, pp. 257–353, 1958.

[22] P. Descouvemont and D. Baye, "The R-matrix theory," *Rept. Prog. Phys.*, vol. 73, p. 036301, 2010.

[23] C. A. Bertulani, *Nuclear Physics in a Nutshell*. Princeton University Press, 2007.

[24] P. Navratil and B. R. Barrett, "Large basis shell model calculations for p-shell nuclei," *Phys. Rev.*, vol. C57, pp. 3119–3128, 1998.

[25] P. Navratil, J. P. Vary, W. E. Ormand, and B. R. Barrett, "Six-Nucleon Spectroscopy from a Realistic Nonlocal Hamiltonian," *Phys. Rev. Lett.*, vol. 87, p. 172502, 2001.

[26] S. C. Pieper, V. R. Pandharipande, R. B. Wiringa, and J. Carlson, "Realistic models of pion exchange three nucleon interactions," *Phys. Rev.*, vol. C64, p. 014001, 2001.

[27] S. C. Pieper, "Quantum Monte Carlo calculations of light nuclei," *Nucl. Phys.*, vol. A751, pp. 516–532, 2005.

[28] E. Epelbaum, H. Krebs, D. Lee, and U.-G. Meissner, "Lattice calculations for A=3,4,6,12 nuclei using chiral effective field theory," *Eur. Phys. J.*, vol. A45, pp. 335–352, 2010.

[29] T. A. Lähde, E. Epelbaum, H. Krebs, D. Lee, U.-G. MeiSSner, and G. Rupak, "Lattice effective field theory for nuclei from A = 4 to A = 28," *31st International Symposium on Lattice Field Theory*, 2013. [PoSLATTICE2013,231(2014)].

[30] T. A. Lähde, E. Epelbaum, H. Krebs, D. Lee, U.-G. Meißner, and G. Rupak, "Lattice Effective Field Theory for Medium-Mass Nuclei," *Phys. Lett.*, vol. B732, pp. 110–115, 2014.

[31] F. Coester and H. Kümmel, "Short-range correlations in nuclear wave functions," *Nuclear Physics*, vol. 17, pp. 477–485, July 1960.

[32] B. Mihaila and J. Heisenberg, "Microscopic calculation of the inclusive electron scattering structure function in ^{16}O," *Phys. Rev. Lett.*, vol. 84, pp. 1403–1406, 2000.

[33] G. Hagen, T. Papenbrock, M. Hjorth-Jensen, and D. J. Dean, "Coupled-cluster computations of atomic nuclei," *Rept. Prog. Phys.*, vol. 77, no. 9, p. 096302, 2014.

[34] R. B. Wiringa, V. G. J. Stoks, and R. Schiavilla, "An Accurate nucleon-nucleon potential with charge independence breaking," *Phys. Rev.*, vol. C51, pp. 38–51, 1995.

[35] R. Machleidt, F. Sammarruca, and Y. Song, "Nonlocal nature of the nuclear force and its impact on nuclear structure," *Phys. Rev.*, vol. C53, no. 4, pp. R1483–R1487, 1996.

[36] J. Carlson, V. R. Pandharipande, and R. B. Wiringa, "Three-nucleon interaction in 3-body, 4-body, and infinite-body systems," *Nucl. Phys.*, vol. A401, pp. 59–85, 1983.

[37] V. I. Zagrebaev, B. Fornal, S. Leoni, and W. Greiner, "Formation of light exotic nuclei in low-energy multinucleon transfer reactions," *Phys. Rev.*, vol. C89, no. 5, p. 054608, 2014.

[38] K. Artemov, O. P. Belyanin, A. L. Vetoshkin, R. Wolski, M. S. Golovkov, V. Z. Goldberg, M. Madeja, V. V. Pankratov, I. N. Serikov, V. A. Timofeev, V. N. Shadrin, and J. Szmider, "Effective method of study of a-cluster states," *Sov. J. Nucl. Phys.*, vol. 52, p. 408, 1990.

[39] V. Z. Goldberg, B. T. Roeder, G. V. Rogachev, G. G. Chubarian, E. D. Johnson, C. Fu, A. A. Alharbi, M. L. Avila, A. Banu, M. McCleskey, J. P. Mitchell, E. Simmons, G. Tabacaru, L. Trache, and R. E. Tribble, "First observation of ^{14}F," *Phys. Lett.*, vol. B692, pp. 307–311, 2010.

[40] E. Uberseder *et al.*, "Nuclear structure beyond the neutron drip line: the lowest energy states in ^{9}He via their T=5/2 isobaric analogs in ^{9}Li," *Phys. Lett.*, vol. B754, pp. 323–327, 2016.

[41] S. Upadhyayula, G. V. Rogachev, V. Z. Goldberg, J. Hooker, C. Hunt, H. Jayatissa, Y. Koshchiy, E. Uberseder, and A. Volya, "Search for the high spin members in ^{10}Be," *AIP Conf. Proc.*, vol. 2038, no. 1, p. 020029, 2018.

[42] D. R. Nygren, "The Time Projection Chamber: A New 4π Detector for Charged Particles," *eConf*, vol. C740805, p. 58, 1974.

[43] A. S. Jensen, K. Riisager, D. V. Fedorov, and E. Garrido, "Structure and reactions of quantum halos," *Rev. Mod. Phys.*, vol. 76, pp. 215–261, 2004.

[44] I. Tanihata, H. Hamagaki, O. Hashimoto, Y. Shida, N. Yoshikawa, K. Sugimoto, O. Yamakawa, T. Kobayashi, and N. Takahashi, "Measurements of Interaction Cross-Sections and Nuclear Radii in the Light p Shell Region," *Phys. Rev. Lett.*, vol. 55, pp. 2676–2679, 1985.

[45] H. G. Bohlen, B. Gebauer, von Lucke-Petsch M., A. N. von Oertzen W. Ostrowski, M. Wilpert, T. Wilpert, H. Lenske, D. V. Alexandrov, A. S. Demyanova, E. Nikolskii, A. A. Korsheninnikov, O. A. A., R. Kalpakchieva, Y. E. Penionzhkevich, and S. Piskor, "Solution of the ^{10}Li-Puzzle - Mass and excited states," *Z. Phys. A*, vol. 344, p. 381, 1993.

[46] L. Axelsson, M. J. G. Borge, S. Fayans, V. Z. Goldberg, S. Grévy, D. Guillemaud-Mueller, B. Jonson, K. M. Källman, T. Lönnroth, M. Lewitowicz, P. Manngård, K. Markenroth, I. Martel, A. C. Mueller, I. Mukha, T. Nilsson, G. Nyman, N. A. Orr, K. Riisager, G. V. Rogachev, M. G. Saint-Laurent, I. N. Serikov, O. Sorlin, O. Tenglad, F. Wenander, J. S. Winfield, and R. Wolski, "Study of the unbound nucleus ^{11}N by elastic resonance scattering," *Phys. Rev.*, vol. C54, pp. R1511–R1514, 1996.

[47] N. A. F. M. Poppelier, L. D. Wood, and P. W. M. Glaudemans, "Properties of exotic p-shell nuclei," *Phys. Lett.*, vol. 157B, pp. 120–122, 1985.

[48] K. Varga, Y. Suzuki, and R. G. Lovas, "Microscopic multicluster model of ^{9,10,11}Li," *Phys. Rev.*, vol. C66, p. 041302, 2002.

[49] K. Varga, Y. Suzuki, and I. Tanihata, "Microscopic four cluster description of the ^{9}Li and ^{9}C mirror nuclei," *Phys. Rev.*, vol. C52, pp. 3013–3025, 1995.

[50] K. Varga, Y. Suzuki, and I. Tanihata, "Microscopic multicluster description of the ^{7}Li-^{7}Be-7, ^{8}Li-^{8}B and ^{9}Li-^{9}C mirror nuclei," *Nucl. Phys.*, vol. A588, no. 1, pp. c157–c160, 1995.

[51] M. Zinser, F. Humbert, T. Nilsson, W. Schwab, H. Simon, T. Aumann, M. J. G. Borge, L. V. Chulkov, J. Cub, T. W. Elze, H. Emling, H. Geissel, D. Guillemaud-Mueller, P. G. Hansen, R. Holzmann, H. Irnich, B. Jonson, J. V. Kratz, R. Kulessa, Y. Leifels, H. Lenske, A. Magel, A. C. Mueller, G. Munzenberg, F. Nickel, G. Nyman, A. Richter, K. Rissager, C. Scheidenberger, G. Schrieder, K. Stelzer, J. Stroth,

A. Surowiec, O. Tengblad, E. Wajda, and E. Zude, "Invariant mass spectroscopy of ^{10}Li and ^{11}Li," *Nucl. Phys.*, vol. A619, pp. 151–176, 1997.

[52] P. Santi *et al.*, "Structure of the ^{10}Li nucleus investigated via the ^{9}Li(d,p) ^{10}Li reaction," *Phys. Rev.*, vol. C67, p. 024606, 2003.

[53] H. G. Bohlen, A. Blazevič, B. Gebauer, W. Von Oertzen, S. Thummerer, R. Kalpakchieva, S. M. Grimes, and T. N. Massey, "Spectroscopy of exotic nuclei with multi-nucleon transfer reactions," *Progress in Particle and Nuclear Physics*, vol. 42, p. 17, 1999.

[54] J. A. Caggiano, D. Bazin, W. Benenson, B. Davids, B. M. Sherrill, M. Steiner, J. Yurkon, A. F. Zeller, and B. Blank, "Spectroscopy of the ^{10}Li nucleus," *Phys. Rev.*, vol. C60, p. 064322, 1999.

[55] B. M. Young, W. Benenson, J. H. Kelley, N. A. Orr, R. Pfaff, B. M. Sherrill, M. Steiner, M. Thoennessen, J. S. Winfield, J. A. Winger, S. J. Yennello, and A. Zeller, "Low-lying structure of ^{10}Li in the reaction ^{11}B (^{7}Li, ^{8}B) ^{10}Li," *Phys. Rev.*, vol. C49, pp. 279–283, 1994.

[56] S. Aoyama, K. Kato, and K. Ikeda, "Resonant structures in the mirror nuclei ^{10}N and ^{10}Li," *Phys. Lett.*, vol. B414, pp. 13–17, 1997.

[57] L. Bianchi, B. Fernandez, J. Gastebois, A. Gillibert, W. Mittig, and J. Barrette, "Speg: An Energy Loss Spectrometer for Ganil," *Nucl. Instrum. Meth.*, vol. A276, p. 509, 1989.

[58] D. R. Tilley, J. H. Kelley, J. L. Godwin, D. J. Millener, J. E. Purcell, C. G. Sheu, and H. R. Weller, "Energy levels of light nuclei A=8,9,10," *Nucl. Phys.*, vol. A745, pp. 155–362, 2004.

[59] R. E. Tribble, A. Azhari, C. A. Gagliardi, J. C. Hardy, A. Mukhamedzhanov, X. Tang, L. Trache, and S. J. Yennello, "Radioactive beams at Texas A&M University," *Nucl. Phys.*, vol. A701, pp. 278C–281C, 2002.

[60] G. Knoll, *Radiation Detection and Measurement (4th ed.).* Hoboken, NJ: John Wiley, 2010.

[61] R. Brun and F. Rademakers, "ROOT: An object oriented data analysis framework," *Nucl. Instrum. Meth.*, vol. A389, pp. 81–86, 1997.

[62] J. F. Ziegler, M. D. Ziegler, and J. P. Biersack, "SRIM - The stopping and range of ions in matter (2010)," *Nuclear Instruments and Methods in Physics Research B*, vol. 268, pp. 1818–1823, June 2010.

[63] S. Agostinelli, J. Allison, K. Amako, J. Apostolakis, H. Araujo, P. Arce, M. Asai, D. Axen, S. Banerjee, G. Barrand, F. Behner, L. Bellagamba, J. Boudreau, L. Broglia, A. Brunengo, H. Burkhardt, S. Chauvie, J. Chuma, R. Chytracek, G. Cooperman, G. Cosmo, P. Degtyarenko, A. Dell'Acqua, G. Depaola, D. Dietrich, R. Enami, A. Feliciello, C. Ferguson, H. Fesefeldt, G. Folger, F. Foppiano, A. Forti, S. Garelli, S. Giani, R. Giannitrapani, D. Gibin, J. J. Gomeze Cadenas, I. Gonzalez, G. Gracia Abril, L. G. Greeniaus, W. Greiner, V. Grichine, A. Grossheim, P. Gumplinger, R. Hamatsu, K. Hashimoto, H. Hasui, A. Heikkinen, A. Howard, V. Ivanchenko, A. Johnson, F. W. Jones, J. Kallenbach, N. Kanaya, M. Kawabata, Y. Kawabata, M. Kawaguti, S. Kelner, P. Kent, T. Kodama, R. Kokoulin, M. Kossov, H. Kurashige, E. Lamanna, T. Lampen, V. Lara, V. Lefebure, F. Lei, M. Liendl, W. Lockman, F. Longo, S. Magni, M. Maire, E. Medernach, K. Minamimoto, P. Mora de Freitas, Y. Morita, K. Murakami, M. Nagamatu, R. Nartallo, P. Nieminen, T. Nishimura, K. Ohtsubo, M. Okamura, S. O'Neale, Y. Oohata, K. Paech, J. Perl, A. Pfeiffer, M. G. Pia, F. Ranjard, A. Rybin, S. Sadilov, E. Di Salvo, G. Santin, T. Sasaki, N. Savvas, Y. Sawada, S. Scherer, S. Sei, V. Sirotenko, D. Smith, N. Starkov, H. Stoecker, J. Sulkimo, M. Takahata, S. Tanaka, E. Tcherniaev, F. Safai Tehrani, M. Tropeano, P. Truscott, H. Uno, L. Urban, P. Urban, M. Verderi, A. Walkden, W. Wander, H. Weber, J. P. Wellisch, T. Wenaus, D. C. Williams, D. Wright, T. Yamada, H. Yoshida, and D. Zschiesche, "GEANT4: A Simulation toolkit," *Nucl. Instrum. Meth.*, vol. A506, pp. 250–303, 2003.

[64] E. D. Johnson, *The Cluster Structure of Oxygen Isotopes*. PhD thesis, Florida State University, 2008. Available online at http://diginole.lib.fsu.edu.

[65] H. Bethe and J. Ashkin, *Experimental Nuclear Physics*. Wiley, 1953.

[66] E. Kashy, W. Benenson, and J. A. Nolen, "A=9 isospin quartet," *Phys. Rev.*, vol. C9, pp. 2102–2105, 1974.

[67] M. S. Golovkov, V. Z. Goldberg, L. S. Danelyan, V. I. Dukhanov, I. L. Kuleshov, A. E. Pakhomov, I. N. Serikov, V. A. Timofeev, and V. N. Unezhev, "Population of States of the Nuclei ^{9}C and ^{13}O in the (^{3}He, ^{6}He) Reaction," *Sov. J. Nucl. Phys.*, vol. 53, p. 550, 1991.

[68] K. M. Nollett, "Ab initio calculations of nuclear widths via an integral relation," *Phys. Rev.*, vol. C86, p. 044330, 2012.

[69] Y. Giomataris, P. Rebourgeard, J. P. Robert, and G. Charpak, "MICROMEGAS: A High granularity position sensitive gaseous detector for high particle flux environments," *Nucl. Instrum. Meth.*, vol. A376, pp. 29–35, 1996.

[70] E. C. Pollacco, S. Anvar, H. Baba, P. Baron, D. Bazin, C. Belkhiria, B. Blank, J. Chavas, P. Chomaz, E. Delagnes, F. Druillole, P. Hellmuth, C. Huss, E. Galyaev, W. G. Lynch, W. Mittig, T. Murakami, L. Nalpas, J. L. Pedroza, R. Raabe, J. Pibernat, B. Raine, A. Rebii, A. Taketani, F. Saillant, D. Suzuki, N. Usher, and G. Wittwer, "GET: A Generic Electronic System for TPCs for Nuclear Physics Experiments," *Phys. Procedia*, vol. 37, pp. 1799–1804, 2012.

[71] E. C. Pollacco, G. F. Grinyer, F. Abu-Nimeh, T. Ahn, S. Anvar, A. Arokiaraj, Y. Ayyad, H. Baba, M. Babo, P. Baron, D. Bazin, S. Beceiro-Novo, C. Belhkiria, M. Blaizot, B. Blank, J. Bradt, G. Cardella, L. Carpenter, S. Ceruti, E. De Filippo, E. Delagnes, S. De Luca, H. De Witte, F. Druillole, B. Duclos, F. Favela, A. Fritsch, J. Giovinazzo, C. Gueye, T. Isobe, P. Hellmuth, C. Huss, B. Lachacinski, A. T. Laffoley, G. Lebertre, L. Legeard, W. G. Lynch, T. Marchi, L. Martina, C. Maugeais, W. Mittig, L. Nal-

pas, E. V. Pagano, J. Pancin, O. Poleshchuk, J. L. Pedroza, J. Pibernat, S. Primault, R. Raabe, B. Raine, A. Rebii, M. Renaud, T. Roger, P. Roussel-Chomaz, P. Russotto, G. Saccà, F. Saillant, P. Sizun, D. Suzuki, J. A. Swartz, A. Tizon, N. Usher, G. Wittwer, and J. C. Yang, "GET: A generic electronics system for TPCs and nuclear physics instrumentation," *Nucl. Instrum. Meth.*, vol. A887, pp. 81–93, 2018.

[72] R. O. Duda and P. E. Hart, "Use of the hough transformation to detect lines and curves in pictures," *Commun. ACM*, vol. 15, pp. 11–15, Jan. 1972.

[73] R. E. Azuma, E. Uberseder, E. C. Simpson, H. Brune, C. R. Constantini, R. J. de Boer, J. Görres, M. Heil, P. J. LeBlanc, C. Ugalde, and M. Wiescher, "AZURE: An R-matrix code for nuclear astrophysics," *Phys. Rev.*, vol. C81, p. 045805, 2010.